

IMPROVING THE MECHANICAL PROPERTIES OF COLD SPRAY METALIZED POLYMERS

by

Jung-Ting Tsai

A Dissertation

Submitted to the Faculty of Purdue University

In Partial Fulfillment of the Requirements for the degree of

Doctor of Philosophy



School of Materials Engineering

West Lafayette, Indiana

December 2021

THE PURDUE UNIVERSITY GRADUATE SCHOOL
STATEMENT OF COMMITTEE APPROVAL

Dr. David Bahr, Co-Chair

School of Materials Engineering

Dr. Martin Byung-Guk Jun, Co-Chair

School of Mechanical Engineering

Dr. Lia Stanciu

School of Materials Engineering

Dr. Chelsea Davis

School of Materials Engineering

Approved by:

Dr. David Bahr

Dedication to Tsai family

ACKNOWLEDGMENTS

Dr. Bahr has always inspired me in my research work. His mentoring method is beyond reproach. Dr. Bahr's unwavering support throughout my Ph.D. journey was unquestionable, and I have learned from him to be more than a "researcher".

Dr. Jun's patient, persistence, passion have encouraged me every weekly group meeting. His advising method allows me to think outside the box, be innovative, and be hands-on in every experiment. In addition, he has allowed me to develop the necessary skills to advance my research career and support my pursuit.

My time at the EPICS was fruitful. Thank you to all the staff members and graduate TAs. I especially like to thank Jorge Martinez. He has been supportive in many ways. From the MSE Bronze to the lab managing. From sand casting to materials maintenance. My practical experiences, such as mentoring undergrad and administration work experience gain mainly because of him. I want to thank many, from Sivash Ghanbari, about simulation methods to Raheleh Mohammad Rahimi, David Brice, and Yailuth Alexandra Loaiza Lopera for electrospun forms, Temitope Aminu critics of research results. Furthermore, I want to thank research colleagues from Semih Akin for his collaboration in building the cold spray, Fengfeng Zhou relentless research support, Feraas Al-Najjar supporting lab supplies, and others from Seunghwan Jo, Xingyu Fu, Kyeongeun Song, Ted Gabor, Eunseob Kim, Siying Chen, Huitaek Yun, Hanjun Kim, Hangeun Joe, Sengul Teke, Farida Tangpoolcharoen. Thank you all for supporting me in the lab. Also, Professor Jeong and Professor Park's research discussions were helpful. Lastly, Reid Schmidt and David general assistance at Flex lab.

Others, I would like to thank Nesredin Kedir for his valuable ideas, Li-kai's in manuscript suggestions, Miguel Ramirez's perspective in damage mechanicals, and I learned a lot from Owen Davis Saturday bible study. Jinling Gau about the manuscript discussion. Sabrina Huang for her kind support. Thank you again to my committee members: Dr. Bahr, Dr. Jun, Dr. Stanciu, and Dr. Davis.

Finally, thank you for your continued support to pursue my career goal to my beloved father (Sei-Yu), mother (Tsui-Feng), brother, and sister.

TABLE OF CONTENTS

LIST OF TABLES	8
LIST OF FIGURES	9
ABSTRACT	13
1. INTRODUCTION	15
1.1 Motivation	15
1.2 Objectives	16
1.3 Thesis organization	17
2. STATE OF THE ART	19
2.1 Cold spray introduction.....	20
2.1.1 Cold spray mechanism.....	21
2.1.2 The success factor for evaluating cold spray coating on a polymeric substrate	22
2.1.3 Advantages limitations of cold spray on polymeric materials.....	24
2.2 Structure-properties relationship of cold spray metal deposition on polymer	25
2.2.1 Microstructure characteristics of metalized polymer	25
2.2.2 Adhesion and mechanical performance metalized polymer	26
2.2.3 Electrical properties of metalized polymer.....	29
2.3 Future cold spray applications	31
2.4 Conclusion	32
3. NUMERICAL INVESTIGATION INTO COLD SPRAY A SINGLE METAL PARTICLE ON POLYMER SUBSTRATE.....	34
3.1 Introduction.....	34
3.2 Numerical methods	36
3.2.1 Material models	36
3.2.2 Simulation properties.....	36
3.3 Numerical results and discussion.....	38
3.3.1 Numerical FEA factors	38
3.3.2 Numerical material factors	39
3.4 Experimental results.....	42
3.5 Conclusion	44

4. MEASUREMENT METHODS FOR RELATING POWDER FLOWABILITY IN COLD SPRAY SYSTEM.....	46
4.1 Introduction.....	46
4.2 Material and methods.....	48
4.2.1 Material selection and process.....	48
4.2.2 Powder flowability measurement	49
4.2.3 Powder velocity measurement.....	51
4.2.4 Mass flow rate measurement	53
4.3 Results.....	54
4.3.1 Powder size distribution and morphology	54
4.3.2 Powder flowability.....	56
4.3.3 Particle velocity during cold spray	59
4.3.4 Mass flow rate.....	60
4.4 Discussion.....	61
4.5 Conclusion	63
5. ESTABLISHING A COLD SPRAY PARTICLE DEPOSITION WINDOW ON POLYMER SUBSTRATE.....	65
5.1 Introduction.....	65
5.2 Experimental procedures	67
5.2.1 Material selection and process.....	67
5.2.2 Two-disk (plate) rotary system.....	68
5.3 Numerical method.....	71
5.3.1 Material model.....	71
5.3.2 Simulation properties.....	76
5.4 Results and discussion	78
5.5 Conclusion	83
6. THE MECHANICAL STRENGTH OF COLD SPRAYED SN ON A POLYMER SUBSTRATE.....	85
6.1 Introduction.....	85
6.2 Experimental procedures	88
6.3 Results and discussion	92

6.4 Conclusion	104
7. ELECTRICALLY CONDUCTIVE METALIZED POLYMERS BY COLD SPRAY AND CO-ELECTROLESS DEPOSITION.....	106
7.1 Introduction.....	106
7.2 Materials and methods	108
7.2.1 Materials	108
7.2.2 Cold spray particle deposition	109
7.2.3 Numerical modeling	109
7.2.4 Co-electroless deposition.....	110
7.3 Results and discussion	110
7.3.1 Cold spray particle impact	110
7.3.2 Microstructure investigation.....	113
7.3.3 Adhesion testing	115
7.3.4 Mechanical strength.....	117
7.3.5 Electrical conductivity	117
7.4 Conclusion	119
8. COLD SPRAY MULTILAYER METAL BUILD-UP ON A POLYMERIC SUBSTRATE ..	120
8.1 Introduction.....	120
8.2 Materials preparation and experimental process.....	121
8.3 Results and discussion	126
8.3.1 Microstructure characterization	126
8.3.2 Mechanical performance	129
8.3.3 Electrical performance.....	132
8.4 Conclusion	132
9. SUMMARY AND FUTURE WORK.....	133
REFERENCES	137

LIST OF TABLES

Table 1 The flow chart of this work.....	18
Table 2 The overall conductivity of cold spray on polymer substrate.....	31
Table 3 The studies of geometry size for particle impacting polymer substrate at 400m/s.....	36
Table 4 The effect of element for particle impacting polymer substrate at 400m/s	37
Table 5 The effect of mesh size for particle impacting polymer substrate at 400m/s	39
Table 6 Material damage criteria	40
Table 7 Feedstock powders information.....	49
Table 8 The four powders size distributions (unit μm).....	54
Table 9 Statistical analysis of the four different powders flow angle with rotating speeds	57
Table 10 Tap density measurement from the Granupack	58
Table 11 Feedstock powders properties.....	67
Table 12 Material constants used in the three-network model (Polyamide 6,6 substrate)	73
Table 13 Cu material constants used in the Johnson-Cook plasticity model.....	75
Table 14 Al_2O_3 material constants used in the Druker-Prager plasticity model	76
Table 15 The modified Weibull model constants	99
Table 16 The adhesion energy from the four different coating thickness	104
Table 17 Cold spray operating parameters	109
Table 18 Chemical ingredients of the co-ED process.....	110
Table 19 Adhesion test results of as-sprayed and electroless deposition specimens.....	117
Table 20 Cold spray operating process parameters	122
Table 21 The coating materials electrical resistivity	132

LIST OF FIGURES

Figure 2-1 The process-structure-property relationships of the cold spray coating	21
Figure 2-2 Schematic of cold spray process	22
Figure 2-3 Bonding mechanism schematic for cold spray particles on polymers	27
Figure 2-4 Test coupon for bond test.....	29
Figure 3-1 shows the geometry size for (a) condition 1 and (b) condition 3.....	37
Figure 3-2 shows the element size for (a) condition 4 and (b) condition 5	38
Figure 3-3 Polyamide 6 true stress-strain for strain failure at 0.6, 1, and 1.4.....	40
Figure 3-4 The impact velocity vs. friction coefficient (a) density at 4.96 g/cm ³ (b) density at 8.96 g/cm ³	41
Figure 3-5 (a) Spherical Cu powders before cold spray (b) cold sprayed Cu on the polyamide 6 substrate	42
Figure 3-6 Cold spray region of interests (a) cold spray process and coated region (b) surface covered with Cu (c) surface mostly covered with Cu (d) surface partially covered with Cu (e) surface few Cu particle attached but predominantly polymer deform morphology (f) surface reveal crater impact images but no particle attachment.....	43
Figure 3-7 Cross-section of (a) surface morphology area 1 (b) surface morphology area 2	44
Figure 4-1 The connection between powder flowability, particle velocity, and mass flow rate ..	48
Figure 4-2 Schematic of the Granudrum device (a) the drum is placed in a cabinet while rotating, a CCD camera taking images (b) posting processing steps	50
Figure 4-3 (a) Schematic of the Granupack device (b) The cross-section of the compact measurement device.....	51
Figure 4-4 The setup schematic for measuring particle impact velocity	52
Figure 4-5 Cyclone geometry and the cold spray setup for the measurement of mass flow rate .	54
Figure 4-6 Particle size distribution (a) four powders and morphology of (b) Al ₂ O ₃ (c) Cu (mixed) (d) Al (e) Sn	55
Figure 4-7 Images of (a) Al ₂ O ₃ (b) Cu (c) Al (d) Sn from Granudrum at 10 RPM.....	57
Figure 4-8 The four different powders at an increasing RPM with the function of (a) flow angle (b) cohesive index.....	57
Figure 4-9 The tap density of four different powders.....	58
Figure 4-10 The measurement of particle velocity (a) Sn (b) Cu (c) Al (d) Al ₂ O ₃ with the function of input pressure (MPa) and temperature.....	59

Figure 4-11 The measurements of the mass flow rate with the function of hopper feed rate and the inlet pressure (a) Sn (b) Al (c) Al ₂ O ₃ (d) Cu	61
Figure 4-12 Measurement of Sn, Al ₂ O ₃ , Cu, and Al flow angle with the function of (a) hopper feed rate (b) volume flow rate (hopper) (c) mass flow rate (d) volume flow rate (cold spray).....	63
Figure 5-1 SEM images of (a) Al ₂ O ₃ (b) Cu.....	68
Figure 5-2 The setup of the two disk rotary system.....	69
Figure 5-3 The experiment result shows the coating marked on the second plate	70
Figure 5-4 The measured output of particle velocity as a function of input air pressure for this cold spray system.....	71
Figure 5-5 (a) Schematic of the constitutive models for polyamide (b) Stress vs. strain (c) Stress vs. time (d) Stress vs. strain at a strain rate range from -10 ⁰ to -10 ⁷	74
Figure 5-6 (a) Initial conditions used for the impact of the metal particle on the substrate (b) Mesh geometry and the schematic view of the FE model	77
Figure 5-7 (a) Plastic strain distribution of the particle (Cu) and the substrate (Polyamide) (b) Evolution of energy distribution (c) Strain and particle velocity in 30 μm particle and the substrate during the entire process at an impact velocity of 400 m/s.....	79
Figure 5-8 (a) Plastic distribution for the particle (Al ₂ O ₃) and the substrate (Polyamide) (b) Evolution of energy distribution	79
Figure 5-9 Effect of particle size vs. particle velocity (a) Al ₂ O ₃ (b) Cu.....	81
Figure 5-10 Experimental results show the sprayed powders at 300 m/s with (a) Al ₂ O ₃ before and after (b) Cu before and after on the polyamide substrate (Scale bar is 50 μm in all figures)	82
Figure 5-11 Experimental results show the sprayed powders at 200 m/s (a) Al ₂ O ₃ before and after (b) Cu before and after on the polyamide substrate (Scale bar is 50 μm in all figures)	82
Figure 5-12 Simulation results show the particle at 300 m/s (a) Al ₂ O ₃ (b) Cu	83
Figure 5-13 Particle at 300 m/s and 200 m/s with the response of the η, particle counts, and the cumulative particle distribution for (a) Al ₂ O ₃ (b) Cu after impacting polyamide substrate.....	83
Figure 6-1 SEM image of the starting Sn powder morphology used in this study	88
Figure 6-2 Polyamide 6,6 tensile dog-bone specimens (a) after cold spray Sn (b) sprayed speckle pattern (c) after tensile test.....	89
Figure 6-3 A schematic cartoon drawing of an in-situ electrical-mechanical tensile test device. 90	
Figure 6-4 The microscopy image of the Sn coated on polyamide 6,6 substrate at strain 0.24 ...	91
Figure 6-5 Stress-strain results of bulk substrate and the coated substrate with the spray speed at 0.01 m/s, 0.05 m/s, 0.1 m/s, 0.15 m/s (color online).....	93
Figure 6-6 Sn coating on polyamide 6,6 substrate (a) Surface (b) cross-section of the specimen	93

Figure 6-7 Coated specimens optical images, the surface profile, and the surface roughness/thickness (a) 0.01 m/s (b) 0.05 m/s (c) 0.1 m/s (d) 0.15 m/s	94
Figure 6-8 Crack density and the fragment length as a function of engineering strain at spray speed (a) 0.01 m/s (b) 0.05 m/s (c) 0.1 m/s (d) 0.15 m/s	95
Figure 6-9 The modified Weibull distribution curve	98
Figure 6-10 (a) Spray speed at 0.05 m/s with the decrease of fragment length plotted with the coated strength distribution (b) All four coated specimens coated mean strength distribution with increasing fragment length.....	101
Figure 6-11 Four different thickness specimens (a) Coating strength vs. the coating thickness (b) The interfacial shear strength value with the engineering strain	102
Figure 6-12 Relative electrical resistance as a function of engineering strain	103
Figure 7-1 (a) Schematic of a typical cold spray process, (b) experimental setup	108
Figure 7-2 Morphology of copper (Cu) particles.....	109
Figure 7-3 Simulation results of single Cu particle (40 μm) impacting on the polymer surface at an impact velocity of (a) 50 m/s, (b)150 m/s, (c) 300 m/s particle velocities; (d) Cu particle compression ratio after a rebound for different impact velocities, (e) rebound velocity and kinetic energy variation against particle impact velocity	112
Figure 7-4 Simulation results of different-size single Cu particle impacting on the polymer surface at a constant impact velocity of 300 m/s; (a) 5 μm , (b)10 μm , (c) 40 μm particle velocities; (d) Cu particle compression ratio after a rebound for different particle sizes, (e) rebound velocity and kinetic energy variation against particle size	113
Figure 7-5 Surface morphology of (a) as-sprayed and eletroless-plating (b) 2 (c) 4 (d) 8 (e) 16 (f) 24 hrs.....	114
Figure 7-6 Cross-section of (a) as-sprayed and eletroless-plating (b) 2 (c) 4 (d) 8 (e) 16 (f) 24 hrs	115
Figure 7-7 (a) Schematic of the pull-off adhesion test, (b) stress-strain results of bulk and as-cold sprayed polyamide 6 polymers	116
Figure 7-8 Four-point probe measurement; (a) a schematic of setup (b) experimental setup	118
Figure 7-9 Cyclic voltammetry results of 24 hrs electroless plating specimen	119
Figure 8-1 Cold spray system setup.....	122
Figure 8-2 DSC results of (a) PA 6 and (b) PP	123
Figure 8-3 SEM powder morphology of (a) Sn (b) Cu and XRD results of (c) Sn and (d) Cu before cold spray	124
Figure 8-4 Specimens of cold spray Cu and Sn on PA 6, PP and continue to spray Sn or Cu to build the dual-layer	125

Figure 8-5 XRD results of cold sprayed Cu on PA 6 comparing with only Cu powders	126
Figure 8-6 SEM images of surface morphology (a) PP (Cu) (b) PA 6 (Cu) (c) PP (Sn) (d) PA 6 (Sn).....	127
Figure 8-7 Cu particle impinges into the PA 6 substrate	127
Figure 8-8 SEM images of surface morphology (a) PP (Cu/Sn) (b) PA 6 (Cu/Sn) (c) PP (Sn/Cu) (d) PA 6 (Sn/Cu)	128
Figure 8-9 on PA 6 (Cu/Sn/Cu) (a) SEM of the polished cross-section (b) EDS map results ...	129
Figure 8-10 Stress and strain results of bulk and coated (a) PA 6 specimens (b) PP specimens	130
Figure 8-11 Crack behavior observation on specimens surface of (a) PP (Cu) (b) PA 6 (Cu) (c) PP (Sn) (d) PA 6 (Sn) (e) PP (Sn/Cu) (f) PA 6 (Sn/Cu) (g) PP (Cu/Sn) (h) PA 6 (Cu/Sn)	131

ABSTRACT

Cold sprayed metallic coatings on polymers provide the benefits of a non-traditional manufacturing solution. However, the process steps for formulating the coating layer often require trial and error to secure an optimal coating. Many common testing methods for interface adhesion and the coating's mechanical performances only give semi-quantitative measurements. As a result, it's challenging to build the connection between the process-structural relationships of the coated materials. This work established a process simulation framework and created an experimental material characterization method to quantify the mechanical strength of cold spray coatings onto polymer substrates.

Particle velocity, mass flow rate, and powder flowability were measured from a low-pressure cold spray system. Increases in mass flow rate are a consequence of good powder flowability. The developed tools and the measurement devices allow quantifying the powder flowability to deposition efficacy in cold spray coatings. Knowing the experimental parameters, this research utilized a three-network polymer model based on high strain-rate impact tests to simulate the nonlinear time-dependent response of polymer deformation during the cold spray impact with both rigid and deformable particles. The particle's material properties, velocity, and size were systematically studied to obtain various responses from the finite element analysis of the polymer deformation. The numerical results were mapped into diagrams and validated with the experimental results of cold spraying Cu and Al₂O₃ powders.

The cold spray process controls the adhesion strength between the coating and the substrate but does create a relatively wide distribution of film thickness and properties. Therefore, a mechanical test fixture was built to track electrical conductivity and coating fragmentation during tensile testing of metalized polymers. A modified Weibull model used the crack density, fragment length, and the measured specimens strength/strain to calculate the coated strength distribution at a fixed crack density and the mean strength as a function of fragment length. The coatings between 74 μm – 120 μm show an interfacial shear strength between 25 – 53 MPa and an energy release rate between 15 – 32 J/m². The interfacial shear strength of thinner coatings between 23 μm -37 μm reaches as high as 250 MPa but eventually saturate, and the energy release rate range between 43 – 45 J/m². In addition, results show that both interfacial shear strength and energy release rate increase as the coating thickness decreases.

Cold sprayed multi-layer (Sn/Cu) and electroless plated specimens were built successfully using the information from the process simulation model. Cold spray coating increases the engineering performance of the coated substrate. The studies have demonstrated selecting appropriate process parameters for multiple metal/polymer combinations to achieve a successful coating.

Keywords: Cold spray, powder flowability, particle velocity, three-network polymer model, interfacial shear strength, energy release rate, multi-layer, and electroless plating

1. INTRODUCTION

1.1 Motivation

Coating metals or ceramics onto polymer materials may enable many advanced applications. For example, food packaging benefits from an oxide coating to preserve and protect food. Electronic devices gain the advantage of electrically conductive coating for electronic displays and solar cells. Furthermore, from building lightweight and high-strength materials, hybrid additive manufacturing which considers a polymer-metal base is another step towards advanced manufacturing. The wide range of applications suggests the need for studying heterogeneous bonding in material systems. Articles have already demonstrated heterogeneous bonding materials via cold spray coating [1]. Others have suggested using high-impact velocity such as ballistic impact to achieve the goal [2]. However, there are long-standing questions of how to quantify the measurement of adhesion in systems with engineering morphologies, including but not limited to as-machined or as-deposited surface finishes.

A continuous effort has been made in quantifying the cold spray coating metal or ceramic coating on a polymer substrate. The recent focus has shifted towards polymer matrix composite (PMC). From spraying Al to Sn powders towards carbon fiber reinforced polymers. The tuning process parameter such as inlet air, pressure, and temperature is always [3-5]. Thus, the importance of controlling the process parameters to the effectiveness of bonding strength measurements is vital in cold spray coating. As a result, researchers have to produce experimental-oriented analyses to optimize the effort of cold spray coating on polymer substrate. Difficulties often arise if the process condition parameters are adjusted; thus, the coating performances immediately change. Finally, without an adequate analysis of the bonding mechanism that results in the optimal coating parameters, designers may undervalue the cold spray coating, ultimately leading to a trial and error process in developing a coated system.

To date, there are available measuring devices for quantifying process parameters or property performances, but often it's time-consuming for data post-processing or high maintenance of apparatus expenditure. Furthermore, simulation studies are seldom investigated of polymer deform under high-strain rate impact. Recent research has used the Johnson-Cook plasticity model to describe the PEEK plastic deformation of one single particle impact [6]. Tang, et al. [7] has used

a modified Johnson-Cook plasticity model to describe the PEEK plastic deformation instead of multiple Cu particles impacts. This research continues in the effort to establish the material science perspective of process-structure-property relationships.

This thesis will focus on improving the mechanical properties of cold spray metalized polymers. The thesis aims to remedy this gap in the existing literature by analyzing how the polymer material successfully interlocks the metals, forms a coated layer, and addresses the practical nature of roughened and as-finished surfaces to quantify strength and adhesion to the metalized coating on polymers.

1.2 Objectives

Based on the above motivation, the main aim is to address a practical solution for cold spray process control and interface bonding between the coated layer and the polymer substrate to achieve metalized polymer materials. This research has listed four objectives as below.

First, address a systematic approach for defining process windows using conventional simulation tools to optimize metal-polymer adhesion and reliability. The method will mitigate trial and error processes for achieving first layer coating on polymer substrate. Furthermore, the simulation results can produce a reliable process window for cold spray coating during parameters changes.

Secondly, the simulated process window needs to be validated. Thus tools and measurement devices will be built for allowing quantifying the powder flowability to deposition efficacy in cold spray coatings. This would provide quick and easy measurements of cold spray process parameters. Furthermore, particle velocity, mass flow rate, and powder flowability should be addressed in the cold spray system that affects the cold spray deposition efficiency.

Thirdly, this research will investigate the cold spray process controlling the adhesion strength relationships between the coating and the substrate. This will be done by first building an in-situ tensile test for measuring crack density. Next, the coated stress distribution will be calculated by the fragmentation tests and a modified Weibull modulus. Finally, the adhesion strength of the cold spray coating can be measured.

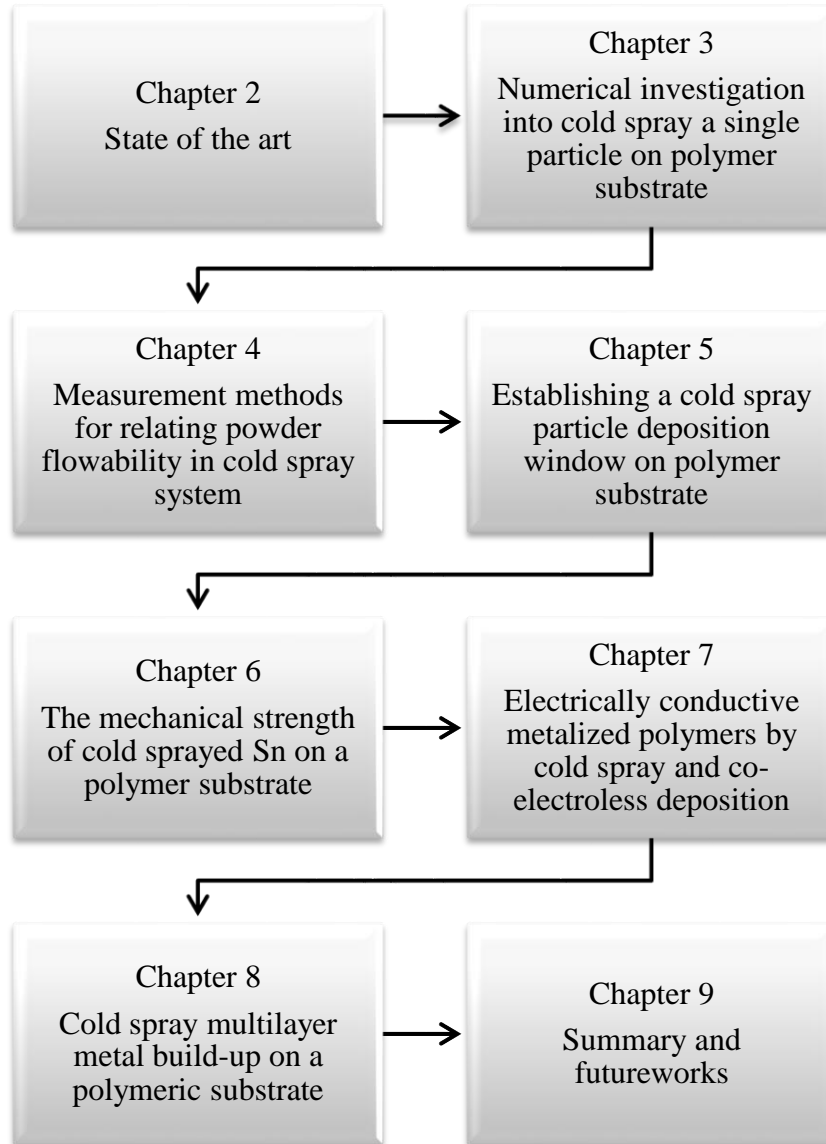
Lastly, a study of the microstructure and the structural integrity of cold spray coated materials. The previously accomplished process simulation will assist two main aims: to construct

a multi-layer coating from a low-pressure cold spray system. The second is to achieve an electroless deposition from a single layer cold spray metalized polymer substrate.

1.3 Thesis organization

This thesis is arranged in the following order shown in Table 1. A literature review that is focused on this work is presented in chapter 2. The process of verification and validation of the numerical model is presented in chapter 3. The devices and techniques for measuring cold spray process parameters and the correlations are in chapter 4. A simulated process window for providing cold spray coating is in chapter 5. The results of adhesion measurements are discussed in chapter 6. The microstructure and the property relationships for multi-layer coating and electroless plating are in chapters 7 and 8. Finally, chapter 9 is the summary of findings and future work.

Table 1 The flow chart of this work



2. STATE OF THE ART

Cold spray is a part of the thermal spray family. However, the term "cold" seems to be misleading. Cold spray technology does operate with temperature (gas temperature preheated from 100 °C to 800 °C). Still, the temperature is relatively lower than the thermal spray (High-velocity oxygen fuel- HVOF thermal spray operates around 2800 °C) [8]. Thus, cold spray is indeed categorized as part of the thermal spray family. In addition, there's a long history and research about thermal spray technology. Traditionally much of the focus on cold spray technologies has emphasized metal to metal, ceramic to ceramic, or metal to ceramic, from experimentally to the current decade's robustness of simulation models. The investment of the technology and R&D primarily deals with national defense or aerospace industries. There are other developments, but the expenditure is relatively more minor. On a global scale, the research area in this field has some large active research groups that have established well-understood mechanisms and standards [9-15].

The focus of the research carried out in this thesis is on the cold spray of metal or ceramic coatings on polymeric materials. A significant difference between the current work and many prior studies is the large mismatch between elastic and plastic deformation conditions between the coating and the material to be coated; for instance, a modulus mismatch of 50x is typical for many metal-polymer combinations, whereas a metal-metal coating may only have a modulus mismatch of 2x. Therefore, this chapter will be focusing on the literature review of cold spray coating metal/ceramic on polymer materials, from the simulation to the experimental and from the theory to the application side. Some literature reviews have already carried out substantial reviews on cold spray polymer materials [16-20]. However, to the author's knowledge, there are still areas that need to be investigated. Therefore, three sections are addressed in this chapter as follows. The first section is a general introduction of cold spray, providing some common terminology that is often used to define a successful coating and giving the cons and pros of cold spray technology. The main goal is to highlight the cold spray process to create metal-coated polymer substrates.

The second section is about the structure-properties relationships of cold spray coated polymer specimens. First, this aims to provide an understanding of coated microstructure and characterize the structural differences of the coating. Second, the bonding mechanism (adhesion) between the metal and the polymer substrate. Determining what process reflects the best bonding strength and

the most significant process parameters is required. Also, other methods to achieve a thick coating layer via low-pressure cold spray will be reviewed. Lastly, the method and techniques of electrical conductivity measurements on the coated specimens after achieving a coated layer are summarized.

Finally, the last section provides the potential application for using cold spray coating on polymeric materials. This section brings current researches done in the area of cold spray technology. There's a need for future application, and the cold spray coating assists in closing the gap between metal/ceramic bonding onto polymer materials.

2.1 Cold spray introduction

Figure 2-1 shows a holistic view of the process-structure-property relationships of the cold spray coating. When addressing the process-structure or structure-property relationship of the cold spray coating, it is often hard to combine all the process conditions and draw conclusions that will inform all individual experiments. The purpose of Figure 2-1 was to give a comprehensive view of the cold spray manufacturing studies. This general overview provides an understanding of the cold spray coating and would narrow down the criteria for coating success. From Figure 2-1, looking into the process, there are three general measures: the cold spray process (materials processing), spraying conditions (robotic arm and device capabilities), and finally, the cold spray tool path. Each of these manufacturing processes influences the coating microstructure and deposition efficiency. As the microstructure reveals the disparity between processes, a material database should be considered to collect the following experimental data. The material microstructure, material modeling, and material database are interconnected, dictating the material's final property performances. The material property before and after the coating is vital for determining coating efficiency.

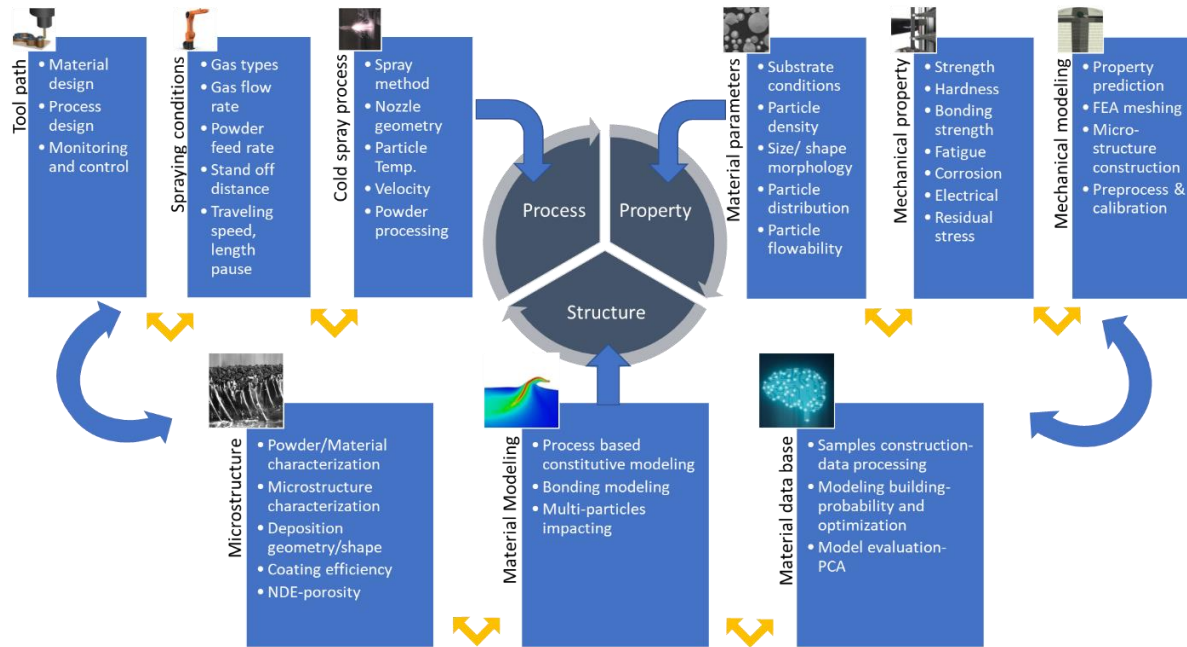


Figure 2-1 The process-structure-property relationships of the cold spray coating

2.1.1 Cold spray mechanism

The cold spray was first documented in the 1980s at the Russian Academy of Sciences [16]. The objective of the application has traditionally been (i) Maintaining expensive parts by structural and geometrical surface repair or from preventing crack growth, (ii) Corrosion protection by coating dissimilar materials, and (iii) Additive manufacturing for small part components.

The cold spray process effectively uses solid powders (1-100 μm in diameter) flowing through the channel and sprayed out through a designed nozzle at high (often supersonic) speeds. Figure 2-2 shows a schematic of a typical design of a cold spray apparatus. Compressed air (1-4 MPa) first flows through the system. The gas is not limited to relatively inert gases such as Helium or Nitrogen. The flow channel is generally preheated to the temperature of 100 $^{\circ}\text{C}$ – 800 $^{\circ}\text{C}$ and merges with the path of the powder feeder. The spray nozzle is designed with a converging/diverging de Laval-type form [8]. The gas and the particle eventually reach supersonic speed on the exit from the nozzle towards the surface [19].

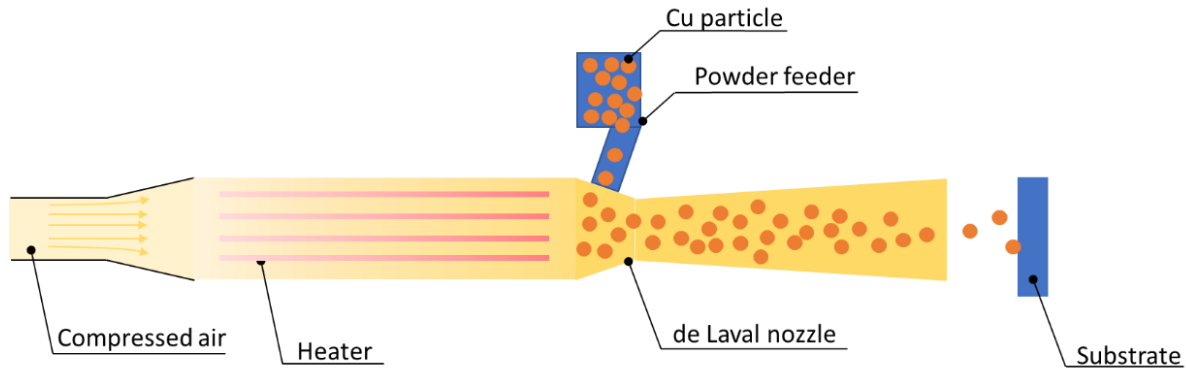


Figure 2-2 Schematic of cold spray process

Compared to thermal spraying, cold spray is relatively low-temperature (High-velocity oxygen fuel- HVOF thermal spray operates around 2800°C). The particles are accelerated through the nozzle, typically at a velocity of 300-1200 m/s. Three types of cold spray flow velocity can be categorized [17]:

- i) Low-pressure cold spray: pressure below 1 MPa with particle velocity 300-600 m/s
- ii) High-pressure cold spray: pressure 1~4 MPa with particle velocity 800-1400 m/s
- iii) Pulsed-gas dynamic spraying: a similar design of cold spray system but by manipulating a fixed frequency shock wave to reduce critical velocity (min. velocity for particles to adhere to the substrate)

Research in cold spray metal particles onto polymer-based materials has been previously done [19-21]. It was concluded that a ductile metal with a low melting temperature is more suitable for deposition on a polymer substrate [20]. As the literature review shows, metal powders for cold spray such as aluminum, zinc, tin, and copper are among the most studied and explored [1, 16, 17, 21-27].

2.1.2 The success factor for evaluating cold spray coating on a polymeric substrate

Achieving a good coating depends on several factors such as the morphology of the powder, type of substrate and the roughness of the surface, the type of spray gas, pressure, and temperature. In addition, process parameters such as standoff distance and particle velocity to the substrate are also factors. The quantitative characterization of the quality of the cold spray process is referred to as deposition efficiency [19]. The deposition efficiency of the cold spray process largely

depends on the (i) critical velocity of the particles and (ii) gas temperature and pressure of the cold spray apparatus. Each of these will be discussed in the following section.

Deposition efficiency is the main index for determining the percentages of particles deposited on the surface. Che, et al. [28] showed that the maximum deposition efficiency could reach up to 44% on polymer coating (inlet pressure at 0.4 MPa and 300 °C). The deposition efficiency is the weight ratio between the particles attached to the substrate (m_s) and the feedstock material supplied to the cold spray apparatus (M_p), as (1)

$$\text{Deposition efficiency} = \frac{m_s}{M_p} \times 100\% \quad (1)$$

A cold spray critical velocity (V_{cr}) is the minimum particle velocity for a particle to adhere to the substrate. Assadi, et al. [9] developed a semi-empirical equation based on the concept of adiabatic shear instability (ASI). This concept explains how a sprayed particle during a high-speed impact causes a localized shear deformation at the particle-particle or particle-substrate interface. The high-speed impact between a particle (powder) and a substrate eliminates the oxide layer from a particle and further increases the bonding at the particle/substrate interface. The expression for the critical velocity (V_{cr}) is given by (2):

$$V_{cr} = 667 - 0.014\rho + 0.08 (T_m - T_{Ref}) + 10^{-7}\sigma_{uts} - 0.4(T_i - T_{Ref}) \quad (2)$$

where ρ is the density in kg/m³, T_m is the melting temperature in °C, σ_{uts} is the ultimate strength in Pa, T_i is the initial particle temperature in °C, and T_{Ref} is the room temperature in °C.

This method provides an idea of the critical velocity of a metal particle that needs to be bonded under small materials and process changes. If the particle velocity is lower than V_{cr} , the particle may impact and abrade the surface without adhering to it. Particle velocity lower than the critical velocity will cause the particles to bounce back after impacting the substrate surface. A bounced-back particle fails to adhere to the substrate but yet may damage and erode the substrate surface. One solution is to increase the V_{cr} to proportionally increase the deposition efficiency of particles, such that the coated surface is covered and compacted with more particles. The quality of coating influences the mechanical and electrical properties of the substrate. The quality of the

coating is not solely defined by the magnitude of V_{cr} but is also influenced by the properties of the feedstock materials and processing parameters [20].

Gas temperature, pressure, and gas type are other process parameters for cold spray. Nitrogen is mainly used for cold spray due to the cost [19]. Although the outlet of the nozzle can adjust pressure, the gas temperature also influences pressure. Bortolussi, et al. [29] showed that the velocity of the compressed air/particle increases as the gas temperature increases. Higher temperature means that the plastic deformation caused by the dislocation between the metal interface has annealed between the particle-particle interface. The relation between the temperature, pressure, and the velocity of the gas is (3):

$$v = \sqrt{\frac{\gamma RT}{M_w}} \quad (3)$$

where γ is the ratio of constant pressure and constant volume-specific heat, which is approximate 1.4 (nitrogen), R is the gas constant, T is the gas temperature, and M_w is the molecular weight of the gas.

2.1.3 Advantages limitations of cold spray on polymeric materials

The cold spray differs from the thermal spray process. The particle velocity travels at a subsonic to supersonic velocity to achieve the bonding. This is an advantage for the particles that are temperature or oxygen-sensitive, such as Cu, Sn, and Al. Thermal spraying entails high process temperatures, generating residual thermal stress, thermal shrinkage, and oxidation on the resulting surface [17]. Thus, a cold spray process is characterized by a relatively low temperature, a well-bonded surface, and low surface porosities. However, a cold spray process has limitations, such as particles may clog the nozzle and further affect the deposition rates. Cold spray is also limited to ductile particles since they must undergo plastic deformation for the particle-particle and particle-substrate interfaces to be bonded. The high energy impact during the cold spray process may deteriorate the structure of the polymer materials [16].

2.2 Structure-properties relationship of cold spray metal deposition on polymer

The cold spray deposition process affects the mechanical properties of the substrate. A relationship between the microstructure and the properties of a coated layer (film) sprayed onto polymeric material was investigated [18-21, 30]. Understanding the results of a cold spray process would aid in controlling (i) the microstructure of deposited coating, (ii) the overall adhesion and mechanical performance of coated polymer substrates, and (iii) the mechanism of the metalized polymer substrate. The cold spray process typically does not provide a uniform quality of the coating layer, both in terms of microstructure and local DE and layer thickness, which may affect the performance of coated polymers [1]. This section addresses the process parameters influencing the microstructure evolution and a deposited conductive film's mechanical and electrical properties on polymeric materials.

2.2.1 Microstructure characteristics of metalized polymer

The cold spray feedstock is generally manufactured by water or gas-atomized powders [8]. Different powder morphologies influence the microstructures deposited on the substrate. Particles with irregular shapes have a better opportunity to interlock on the substrate [24]. Bortolussi, et al. [29] showed that powders with irregular shapes had a better coating build-up layer than spherically shaped powders. Microstructure results show that the irregular shape particle is anchored into the polymer substrate than spherical particles. During the cold spray process, the deposition of particles may deplete the original coated substrate surface. Erosion on the substrate surface is one of the reasons why the deposition efficiency is low. Optical Microscopy (OM) and Scanning Electronic Microscopy (SEM) are utilized to investigate the particle microstructure at the interface and substrate surface morphology. Specific features such as splat morphology, voids, defects, and interface boundaries between the particle-particle and particle-substrate junctions can be observed. For example, when Cu/Sn particles are cold sprayed onto polymers [18, 27], the structure shows partial melting of Sn particles. At the same time, the core remains solid after the deposition of the first coating layer. The subsequent deposition of particles causes an adiabatic shear deformation to the interface with the second layer of particles.

Work has been done to study cold spray's penetration and embed Cu particles into polymer substrate [1]. As the results indicate, the process depends on polymer characteristics such as the

glass transition temperature and melting temperature. In other words, the thermal softening of the substrate will determine the penetration depth of particles by manipulating process parameters such as spray temperature and transverse speed of the nozzle. An average embedment depth of 50 μm was measured after spraying the Cu particles onto the polyethylene or polyurethane substrate. Cold spray is a high kinetic process, and the deposited particle undergoes severe microstructure modifications and deformations [31]. One of the concerns is that cold sprayed particles may degrade the polymer after spraying. Spectroscopy was employed to investigate the wavelength shift. Based on the Raman spectra, the results indicate that the polymer still retains its structure after the high-velocity impact of Cu powders [32]. However, continued deposition caused the surface to be unevenly contoured. Surface morphology revealed the particles bombard the surface leading to waviness and irregularity in the surface morphology of the substrate. The roughness test showed that sprayed surfaces' average roughness (Ra) is higher than un-sprayed surfaces [1].

2.2.2 Adhesion and mechanical performance metalized polymer

Adiabatic shear instability (ASI) is a general theory for explaining the bonding mechanisms between the particle-particle and particle-substrate interfaces created by cold spray. The cold spray technique limits the extent of metal particle oxidation while solid bonds can be formed at the particle-particle and the particle-substrate interfaces [9, 10, 16, 33-35]. Assadi, Gärtner [18] developed a semi-empirical approach to adhesion; however, they do not consider the particle size. Furthermore, this mechanism does not consider the substrate as a viscoelastic material. Current research has observed that the polymer substrate mechanically interlocks the metal particles onto the substrate. Therefore, particles within the substrate retain their original shape shown in Figure 2-3.

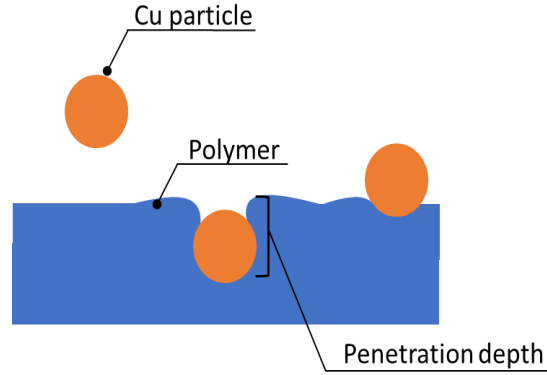


Figure 2-3 Bonding mechanism schematic for cold spray particles on polymers

Che, et al. [36] proposed a process parameter window for cold spraying onto polymer substrates. The window for depositing the first layer coating on the polymer is defined as $v_{cr} < v < v_{ero}$, where v_{cr} is the velocity for the particle to be mechanical interlock onto the surface, v_{ero} is the velocity for the particle to erode the surface without any mechanical interlock. This deposition window is effective only for the first layer of deposition. As the deposition process continues, the impact of the particles may peel off or erode the first layer deposition. The v_{cr} parameter in the past was only focus obtaining metal particles to the metal substrate. Also, more research needs to be conducted to determine the v_{cr} parameter for polymer.

Cold sprayed of copper particles onto polymer substrates such as polyurethane, high-density polyethylene, polypropylene, polyamide 6, polytetrafluoroethylene, and polycarbonate were studied [1]. A general trend revealed that increasing spray temperature allowed deeper penetration. The thermal softening of the polymer has a significant impact on the penetration depth. Finite element analysis was constructed to support the experimental observations by Chen, et al. [32]. The deposition of a single Cu particle onto the PEEK substrate was first simulated. When the Cu-particle impacts the PEEK, the PEEK is covered around the Cu-particle, causing the polymer to interlock the particle. Increasing the propelling gas pressure increases the PEEK jetting surrounding the Cu-particle. Cu-particles have been successfully sprayed onto polyether ether ketone (PEEK). Cold spray on a thermoplastic substrate has many applications such as Vucko, et al. [25] have considered cold spray of Cu-powders onto the HDPE for an antifouling organism. Results showed that a Cu-embedded polymer substrate prevents fouling for more than 250 days. Cold spraying on thermoset polymer substrates remains challenging. Particles attached to the surface are limited, and the localized fracture was observed on the substrate surface in the cold

spray experiment performed by Ganesan, et al. [24]. The aforementioned studies can be a starting point for developing a cold spray process for a metalized polymer. In addition, they provide some valuable hints about which polymers are more feasible for the cold spray procedure. Research is needed to determine the v_{cr} parameter for a polymer substrate. The cold spray process simulation parameters should include material properties such as the polymer elastic modulus, glass transition temperature, polymer's melting temperature, and the particle velocity to embed a particle.

Microhardness measurements give an insight into various mechanical properties across the cold spray deposits on the substrate surface. For example, by raising the gas pressure in the cold spray process, the microhardness of the metal-coated surface increases. As a result, Cu particles encounter high plastic deformation towards the substrate. The peening effect of the particles onto the substrate causes a work-hardening instead of thermo-softening of the substrate, and therefore the microhardness increases [32].

According to ASTM C633 [37], the adhesive strength of the substrate/coating interface is measured by adhesively attaching the substrate/coating specimen to the caps (fixtures) and then applying a tensile force onto the fixtures, as shown in Figure 2-4 to cause the substrate/coating disbonding. The substrate/coating can display a cohesive fracture with crack propagating through the coating layer or an adhesive fracture at the substrate-coating interface. The test results are disregarded if the substrate/coating disbands from the caps. The adhesion strength of the coating on polymer (<20 MPa) is typically much lower than the adhesive strength of the specimen/fixture bond (250 MPa) [26, 28, 29, 32, 36, 38-40]. Therefore, high adhesion strength on a coated substrate, process factors such as particle velocity, gas temperature, pressure, standoff distance, surface roughness, and spray angle must be optimized [19].

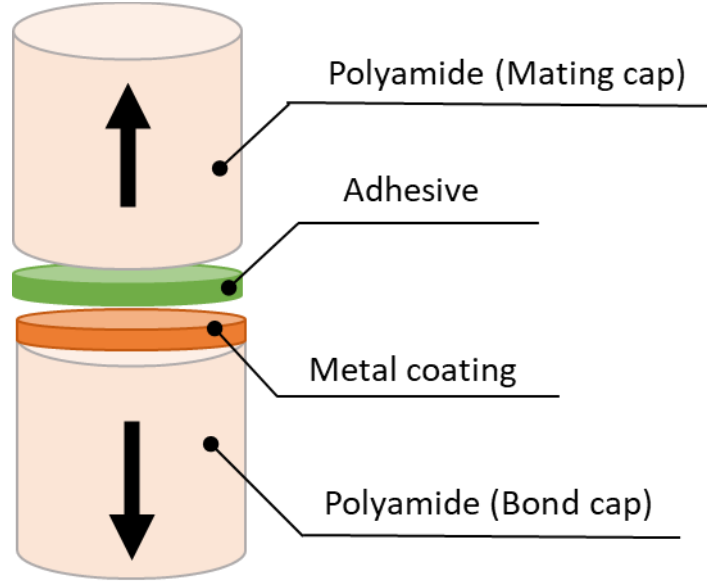


Figure 2-4 Test coupon for bond test

2.2.3 Electrical properties of metalized polymer

The electrical resistivity of cold spray coatings can be measured using a four-point probe apparatus on a coated substrate, as reported by Affi, et al. [39]. The method measured the electrical resistivity of a thin film or coated line on the substrate. The four-point probe was designed with the outer two probes measuring current and the inner two probes measuring voltage; this method is analogous to any conventional four-point probe measurement. Several coated distances were measured to determine the volume resistivity per-cross-sectional area by utilizing the following equation (4):

$$R = \rho \frac{\ell}{A} \quad (4)$$

where R is the electrical resistance of the coating layer on the substrate calculated from the measured current and voltage; ρ is the electrical volume resistivity; ℓ is the length of the coated specimen; A is the cross-section coated area.

As an example of the differences between bulk materials and the properties of the cold spray coating, studies have shown that the electrical conductivity values of bulk copper are typical,

around 59 MS/m however, the value of cold spray copper/PEEK on CFRP is one-third to half the value of bulk copper measurement (Table 2 shows an organized conductivity after cold spray on the substrate). High conductivity can be achieved by reducing the defects associated with the coating, decreasing the substrate surface's roughness, and increasing the cohesion strength of the coating. One way is to increase the gas pressure, and this will proportionally increase the impact velocity and reduce the porosity and inter-particle connection between the particles [32]. However, this is not a promising method because the substrate hardness varies. High gas pressure can cause the particle to bounce off instead of attaching onto the surface, and material particles will be wasted. Che, et al. [28] used a mixed ratio of powder Sn and Cu. It shows a better coating adhesion towards the substrate. This is because Sn has a low melting temperature. During the high impact velocity, Sn was melted and mechanically interlocked onto the rough surface of the polymer. The Sn on the surface has an irregular shape that increases the adhesion strength. The continuously mixed ratio of Cu and Sn was sprayed onto the Sn coating. This method succeeded in building a relatively thick layer of coating. Nevertheless, no substantial improvement in the electrical performance was achieved by adjusting the Cu/Sn metal ratio. It was concluded that the Cu/Sn interfaces might be a barrier to low conductivity. Another solution is to anneal the samples after Cold Spraying the metal particles. This method ensures particles on the surface to recover, recrystallize and further grain growth for a compact structure. The results indicate the conductivity of Cu/Sn increases to the maximum 367 % under a certain Cu/Sn ratio. The increase of electrical conductivity is achieved because of the reduction of voids between the particle-particle and particle-substrate interfaces [28]. It was also reported that a particle morphology with an irregular shape tends to have higher electrical conductivity than a spherical shape [29]. Studies needed to be conducted to explain the connection of coated thickness towards conductivity on the polymer substrate. In future research, the deposition of Cu/Sn can act as an electrode or a design conductive grid pattern for smart-functional polymer sensors.

Table 2 The overall conductivity of cold spray on polymer substrate

Powder	Bulk material σ (S/m)at 20 °C	Coated on polymer σ (S/m)at 20 °C	References
Copper/PEEK	5.96×10^7	5×10^3	[29]
Aluminum	3.5×10^7	5.8×10^6	[39]
Tin	9.17×10^6	4.5×10^6	[28]
Cu-10Zn	NA	5×10^6	[28]
Cu-90Sn	NA	4.5×10^6	[28]
Cu-90Sn (Anneal for 1 hour)	NA	7.3×10^6	[28]

2.3 Future cold spray applications

This work focused on cold spray coating on polymer substrate. Two primary objectives of current work are improving the mechanical and material strength performances, and the other is the increase the electrical performance of the coating. Below are some potential applications or ongoing studies relevant to this work and can be further explored and investigated. For mechanical and materials strength applications:

Composite laminate armor: the coated surface provided the potential ability to blunt the tip of the missile before cutting into the substrate. The coated metal surface has higher binding energy than the polymer, which benefits multilayer build-up. The coating itself can be a laminate structure of soft and hard materials [41, 42]. For example, an array of the elastomer-steel panel has been found to resist the penetration of missiles [43]. In addition, the multilayer build-up inhibits the fracture propagation of cracks in the longitudinal direction [44].

Alternative solution for shot peening: cold spray functions similarly to shot peening but operates in higher kinetic energy that causes the surface plastic deformation and retain residual stresses. The same applies to shot peening can be made in cold spray coating, which releases tensile stresses and introduces compressive stress on the surfaces instead. In addition, the cold spray coating can focus on a region of interest and control the residual stresses for maximizing the mechanical parts of property performances. The coated substrate can also increase its wear and erosive protection [1, 45].

Polymers in extreme environments: exploring the cold spray particles impact behavior of polymer and ultimately polymer composites. At the same time, the cold spray is a high kinetic spray. Therefore, the polymer property performance may be manipulated using cold spray tools to alter its material structure and achieve high mechanical performance [46-49].

One of the most significant advantages of using the cold spray is that the metal powders are not likely to oxidize. Many papers have already emphasized the advantages of electrical conductive applications:

Flexible EMI/RFI shielding and lightning strike protection: cold spray coating comes in handy when the products are already manufactured. An additional function can be added to the device. Composite materials can increase their electrical conductivity by coating Cu coating. In contrast, this increases the protection for lightning strikes and, at the same time, has the flexibility for EMI/RFI shielding for security usages [36, 50].

Structural health monitoring: big construction sites such as bridges, dams, and tunnels often require sensor measurements to monitor or surveillance the structural integrity. The cold spray has been used as a material repair operation (MRO) device for fast and effective repair for army aircraft or navy vehicles in the past. The technology can be adapted into infrastructures facility, while used as an MRO device. Still, at the same time, a conductive coated pattern can also be used to function as a large area strain gauge or sensor detections.

Cold spray for biomaterials application has been done mainly in antifouling and surface coating for sterilization [51]. Often this does not require the coating to be electrically conductive but requires large area coating and disperse distribution. However, there remain some challenges in using cold spray coating in biomaterials. The challenging part is that bio-applications often require consistent coating quality with fine design patterns. It is possible to control the coating processes to be similar to inkjet printing and screen-printing [52, 53]. However, the cost may be extensive and not economical. Therefore, designing a cold spray nozzle and optimized process parameters is one of the important topics as well.

Cold spray for sensor application: have been another potential field. Cold spray coating as electrical conductive electrodes can be made by cold spray coating. Examples include cold spraying accessible and affordable Sn electrodes for analysis in citrate buffer solutions [54], Ni/Cu electrodes for uric acid analysis [55], human urine using cyclic voltammetry, or Zn coating for selective electrical reduction of CO₂ formate in aqueous solutions [56].

2.4 Conclusion

This chapter mainly discusses the state of the art of using cold spraying metalized polymers. The perspective of looking into the process control of the cold spray and the structure-properties

relationships of the coated materials have been comprehensively done. Finally, the potential application of cold spray metalized polymers. The robustness of bonding heterogonous material via cold spray is beneficial, and there's a need to understand the coating mechanism for maximized the engineering performances.

3. NUMERICAL INVESTIGATION INTO COLD SPRAY A SINGLE METAL PARTICLE ON POLYMER SUBSTRATE

Cold spray deposition of a metallic layer on a polymer substrate was numerically simulated using a calibrated three-network polymer model to capture the non-linear and time-dependent response of large strain polymer deformation during cold spray particle impact. Material parameters such as particle density, particle velocity, and particle size were studied to obtain the various responses of the polymer deformation. The material parameters were then varied to construct processing windows that showcase the overall results in a map diagram. The particle's fraction of kinetic energy lost is the parameter that best represents the trend of particle adherence onto the polymer substrate. Spherical Cu powders were cold sprayed onto polyamide 6, and the process parameters agree well with the simulation results. The process windows narrow the interest region for experimental optimization to improve cold spray coating adhesion on a polymer material. This work contributes to predicting the cold spray metal particles depositing on a polymer substrate.

3.1 Introduction

Numerical modeling for high-velocity metal to metal impact has been widely studied [9-11, 57]. Conventional methods are by using the Lagrangian formulation to solve the elastic-plastic deformation of particle-particle impacts. However, this method may be limited by the heavily plastic deformation of the material and causing the calculation to be inaccurate or aborted. One way to solve this issue is by using SPH (smooth particle hydrodynamics). SPH is a technique for simulating fluid dynamics, a mesh-free adaptive Lagrangian computational method. But the trade-off increases computational time and difficulties in setting the boundary conditions [58]. Other alternatives, such as CEL (coupled Eulerian-Lagrangian), are Eulerian elements that interact with Lagrangian elements used in fluid-structure interaction. Nevertheless, the above two methods are very effective in describing materials with high-speed impact [33].

Constitutive equations, such as the Johnson-Cook (JC) plasticity model, often describe metal deformation in moderately high strain rate operations such as machining. However, in high-speed impacts such as cold spray, the strain rate of the particle can reach over 10^6 s^{-1} . Researchers have pointed out that the flow stress bilinear changes with the increased strain rate at high strain rate

impact [59-63]. As demonstrated by previous studies, metals such as copper strain soften at $\approx 10^3$ s⁻¹ [64-70]. One of the reasons is the depletion of dislocation at the grain boundaries, causing the strength to soften. Thus, the JC model may not be suitable for this type of modeling. Rahmati and Ghaei [71] have compared six models describing high strain rate plasticity under metal to metal impacting for the simulation model to mimic such a phenomenon. The six different models are JC, Modified Zerilli Armstrong (MZA), Voyiadjis Abed (VA), Preston Tonk Wallace (PTW), Modified Khan Huang Liang (MKHL), and Gao Zhang (GZ) models. The simulated particle deformed shape compared with the experiment results, and among the six models, the PTW provides the closest shape morphology compared to the experiment results after impact. Others have proposed to adjust the JC model by adding conditions for separating the strain hardening and the strain-softening portion once it reaches the bilinear changes of the flow stress. This alternative was also valuable in capturing the metal coating onto metal layers.

The response of polymer in high strain rate deformation is studied extensively, including testing equipment such as Hopkinson bar, Taylor impact, and transverse impact is implemented in various strain rates testing to observe the response of polymers [42, 46, 49, 72, 73]. A time-temperature superposition for predicting the response of high strain rate polymer was accomplished with a low strain rate input. Church, et al. [74] propose a thermomechanical model that considers the effect of temperature, strain rate, and pressure. The model examines the flow rule, the strain-softening mechanism, and the orientation hardening. Simulation results show good agreement with the experimental results from the PMMA and PC. Sarva, et al. [42] did a study; two types of polymer, PC and PVDF, show an increasing strain rate with the increased temperature. The yield stress shows a bilinear that depends on the strain rate scale. The phenomenon was caused by the beta transition in PC and the glass transition in PVDF at a strain rate between 0.001 to 5000 s⁻¹. A visco-elastoplastic constitutive model, which includes the material after yielding, shows a softening and hardening phenomenon response, was included in the model.

This study implemented a constitutive polymer model in the finite element (FE) frameset to simulate a Cu particle impacting a polyamide substrate. The polymer model was calibrated with already available polymer high strain-rate impact results through PolyUMod[®]. A range of parameters from the defaulting setting of the FEA, such as mesh sensitivity, section control, and contact interaction, was conducted. The goal was to improve the performance of particles impacting the substrate, increase computational efficiency, and mitigate the excessive distortion

between particle contacts. Material properties such as material friction, material damage parameters, particle velocity, particle size, and particle density were also studied to understand the influence of mechanical attachment of the particle onto the polymer substrate. This work contributes to building the simulated and optimized model effectively.

3.2 Numerical methods

3.2.1 Material models

The following details about the materials constitutive equations (including the material constants) and boundary conditions can be found in chapter 5.3.1.

3.2.2 Simulation properties

The conditions for particle/substrate ratios are shown in Table 3. Condition 1 and 2 for particle/polymer ratios are the most commonly suggested [75-78]. The infinite element was added on the side of the polymer substrate, which shows in condition 3. The objective is to evaluate whether the stress propagates during the impact on the substrate with different size ratios of particle/substrate. The size geometry was evaluated without increasing the computational time but still maintained an accurate numerical calculation. The rebound velocity was compared with these three conditions. The output results show that the rebound velocity remains the same for all three cases. Condition 3 has the lowest computation time, while condition 2 has the highest computation time. Also, condition 1 and condition 3 have the lowest artificial energy/internal energy ratio (AE/IE) compared to case 2.

Table 3 The studies of geometry size for particle impacting polymer substrate at 400m/s

Conditions	1	2	3
Particle/substrate	1:5	1:10	Infinite element 1:5
Rebound velocity	0 m/s	0 m/s	0 m/s
Relative CPU time	4	25	3
Energy AE/IE	3.1%	5.9%	2.9%

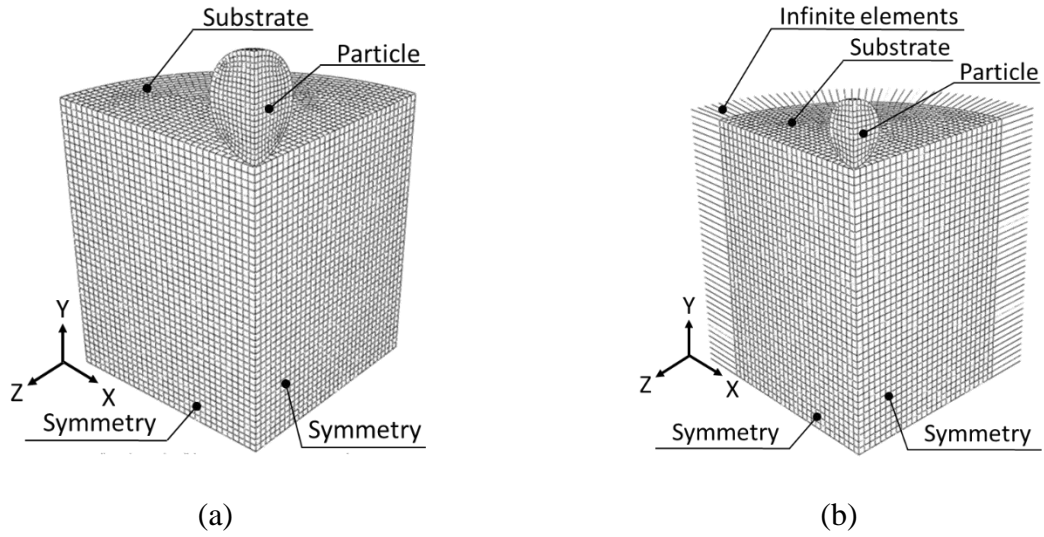


Figure 3-1 shows the geometry size for (a) condition 1 and (b) condition 3

Researchers have suggested that hexahedral elements are best for impact and bending simulations [79-81]. Figure 3-1 shows the particle selected as tetrahedron and hexahedral elements. Wang, et al. [79] explained that tetrahedron elements usually are more rigid. It is because the tetrahedron is more rigid compared with the hexahedral elements. Therefore, particles with tetrahedron elements have a lower AE/IE ratio. However, both cases in Table 4 show the same relative computation time and the same rebound velocity. Thus, setting elements as a tetrahedron or hexahedral may not have much influence on the study.

Table 4 The effect of element for particle impacting polymer substrate at 400m/s

Conditions	4	5
Particle/substrate	1:5	1:5
Particle	C3D4	C3D8
Substrate	C3D8	C3D8
Relative CPU time	4	4
Rebound velocity	0 m/s	0 m/s
Energy AE/IE	2.39%	3.1%

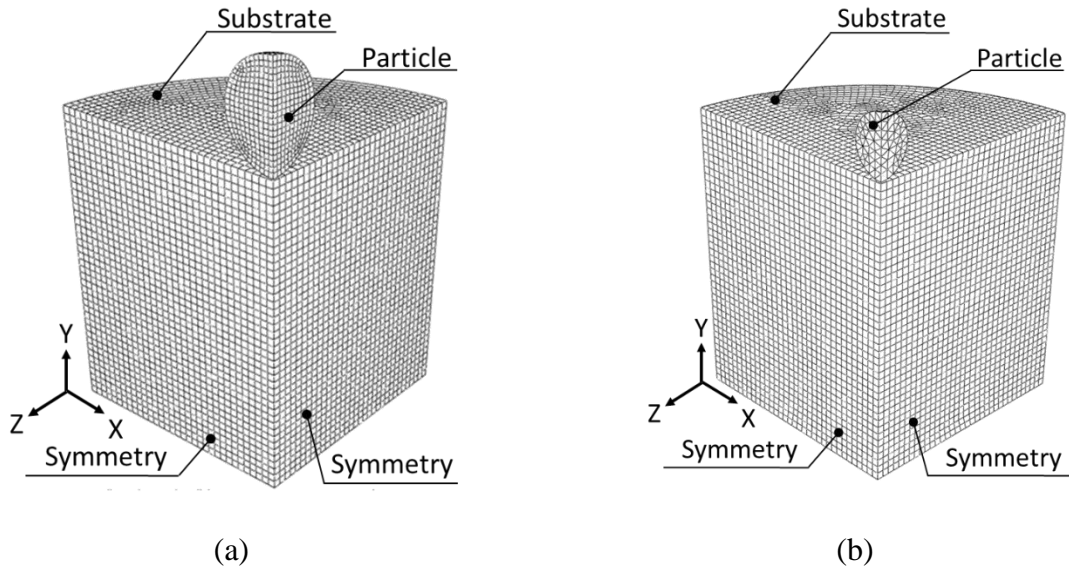


Figure 3-2 shows the element size for (a) condition 4 and (b) condition 5

3.3 Numerical results and discussion

3.3.1 Numerical FEA factors

The effect of the mesh size and hourglass control is shown in Table 5. The objective is to compare the mesh dependency while using the hourglass control to mitigate the mesh distortion from particle impact. The meshing size for the particle was $2\text{ }\mu\text{m}$ for a $30\text{ }\mu\text{m}$ particle (the meshing resolution is $1/15\text{ dp}$). Cases 6-8 and 11-12 have the same mesh size for the particle and the substrate. Cases 9-10 have the particle mesh size smaller than the substrate size. The conditions for the hourglass control are chosen in this study as default (D), enhance (E), or combine (C), which is available in the simulation software. The relative CPU time, rebound velocity, and energy ratio were the three essential factors compared for the seven cases in Table 5. Results show that case 4 requires less computation time, with the smallest AE/IE energy ratio. The rebound velocity is the same compared with the other cases.

Table 5 The effect of mesh size for particle impacting polymer substrate at 400m/s

Cases	6	7	8	9	10	11	12
Hourglass control	D	E	C	D	E	D	E
Particle	$\frac{d_p}{10}$	$\frac{d_p}{10}$	$\frac{d_p}{10}$	$\frac{d_p}{15}$	$\frac{d_p}{15}$	$\frac{d_p}{15}$	$\frac{d_p}{15}$
Substrate	$\frac{d_p}{10}$	$\frac{d_p}{10}$	$\frac{d_p}{10}$	$\frac{d_p}{10}$	$\frac{d_p}{10}$	$\frac{d_p}{15}$	$\frac{d_p}{15}$
Relative CPU time	NA	4	5	4	5	NA	13
Rebound velocity	NA	0 m/s	0 m/s	0 m/s	0 m/s	NA	0 m/s
Energy AE/IE	NA	29%	24%	3.1%	27%	NA	22.2%

Note: 6(D) aborted, the same as 11(D)

3.3.2 Numerical material factors

Figure 3-3 shows the results of the polymer substrate at the strain failure set as 0.6, 1, and 1.4 with the particle size as 30 μm and impact speed at 400 m/s. The finite elements delete under the condition when the failure criteria are satisfied. With the particle traveling at a high velocity, the contact region of the polymer substrate plastic deform and fracture. The failure parameters are taken into consideration to inspect the influence on the rebound velocity of the particle. The three-strain failure indicates that the particle remains in the polymer substrate. Table 6 shows the relative CPU time, the rebound velocity, and the energy AE/IE for the three strain failure parameters. Results show that the particle penetrates deeper in the polymer substrate with strain failure at 0.6 and vise versa.

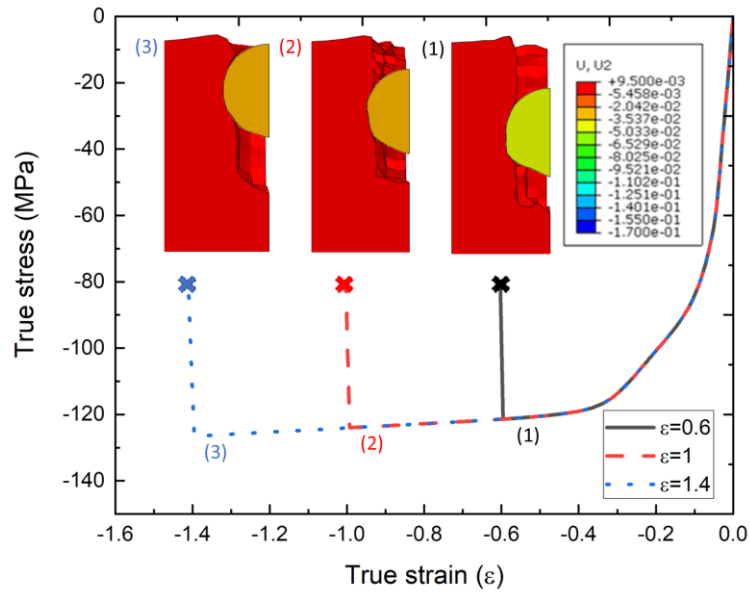
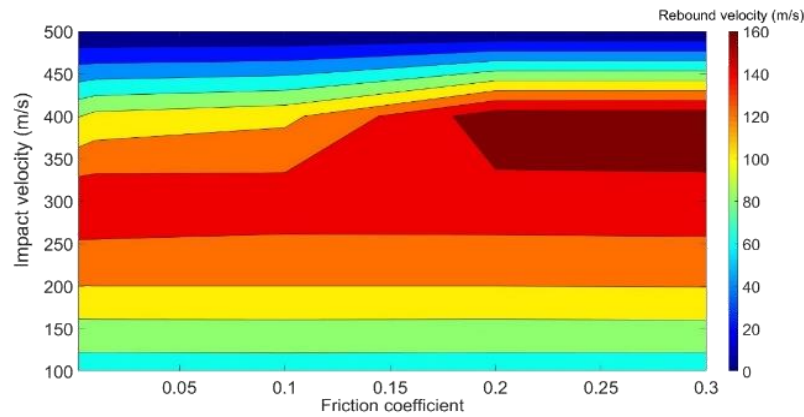


Figure 3-3 Polyamide 6 true stress-strain for strain failure at 0.6, 1, and 1.4

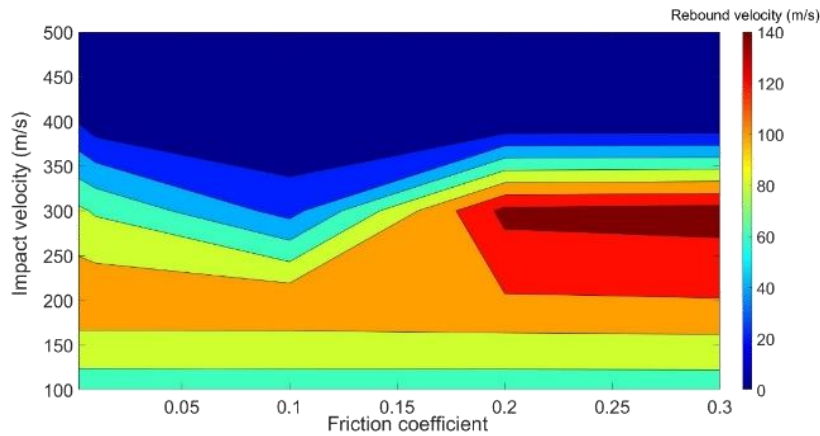
Table 6 Material damage criteria

Cases	9-1	9-2	9-3
Von mises (true) strain	0.6	1	1.4
Relative CPU time	5	4	4
Rebound velocity	0 m/s	0 m/s	0 m/s
Energy AE/IE	5.57	4.72	3.1%

Figure 3-4 (a) shows the particle size at $30\text{ }\mu\text{m}$ and the density at 4.96 g/cm^3 , with the y-axis as the increasing impact velocity and the x-axis as the increased friction coefficient. The impact velocity between $100\text{--}500\text{ m/s}$ shows the differences with the increase of friction coefficient. The particle's rebound velocity is higher with the increase of friction coefficient and vice versa. This trend shows the same results for particle size at $30\text{ }\mu\text{m}$ with a density set at 8.96 g/cm^3 (Figure 3-4 (b)). The particle penetrates deeper into the polymer substrate with a lower friction coefficient, while the particle penetrates less into the polymer substrate with a higher friction coefficient. This simulation result demonstrates that the friction coefficient plays a significant role in particle impacting polymer substrate.



(a)



(b)

Figure 3-4 The impact velocity vs. friction coefficient (a) density at 4.96 g/cm^3 (b) density at 8.96 g/cm^3

3.4 Experimental results

Simulation often accounts for only one particle impact and observes the response of the particle and the substrate. However, during the experiment, a large number of particles impact a region of interest. This may make correlating the simulation results more challenging. Process parameters such as the nozzle spray speed and the powder mass flow rate can be manually controlled. For example, a high mass flow rate with a low nozzle spray speed will result in powders impacting the surface and eventually being embedded into the substrate. One of the alternatives is to look at a close-by region of the spray area; this can avoid multiple particle impacts and correlate well with the simulation results.

For this experiment, we have chosen spherical Cu powders (Chemical Store Inc.) with a minimum purity of 99.99 %, shown in Figure 3-5 (a). The particle size range was measured between 5-44 μm (Malvern Instruments Ltd, UK). The cold spray device is a K205/407R model attached to a six-axis robotic arm and cold spray at a fixed distance of 20 mm from the substrate. An input compressed air was controlled at 0.65 MPa. The sprayed particle has a particle speed of 320 m/s (used a two-disk plate rotary system to measure particle velocity in chapter 4.2.3). In addition, the experiment was done with one path of spray onto a polyamide 6 substrates shown in Figure 3-5 (b).

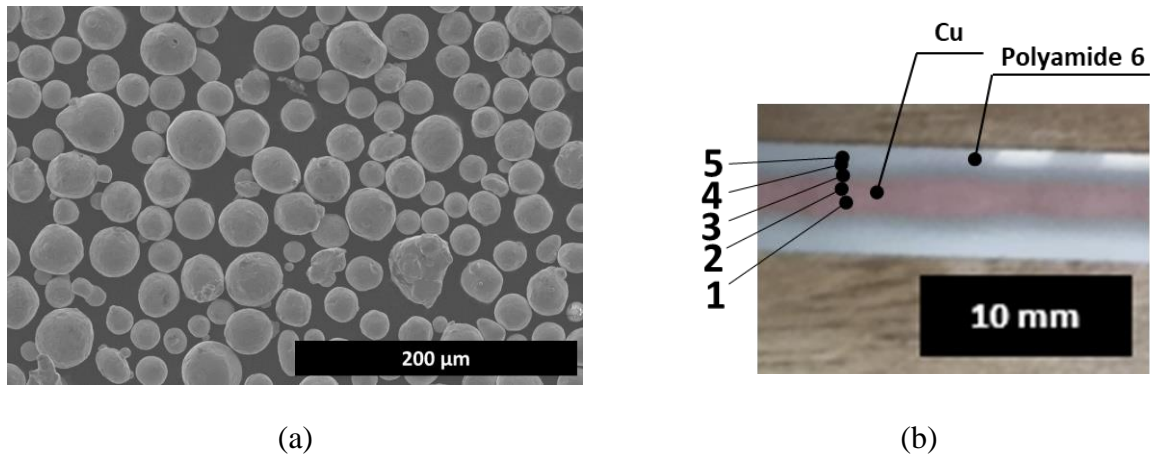


Figure 3-5 (a) Spherical Cu powders before cold spray (b) cold sprayed Cu on the polyamide 6 substrate

Figure 3-6 shows the cold sprayed region surface morphology; a continuous section of SEM images was taken, marked in Figure 3-6 (a and b). Figure 3-6 (b) to Figure 3-6 (f) show a coated dense region of Cu and move to a none coated region but with crater morphology on the surface. The results show that there's more particle impacting at the vertical direction of the cold spray nozzle to the substrate, and thus particles are attached. While as the coated region moves further away from the spray nozzle, fewer particles are attached. Region slightly away from the cold spray nozzle eliminates the concentrated particle's continuous impact and focuses on a single particle embedded in the polymer substrate.

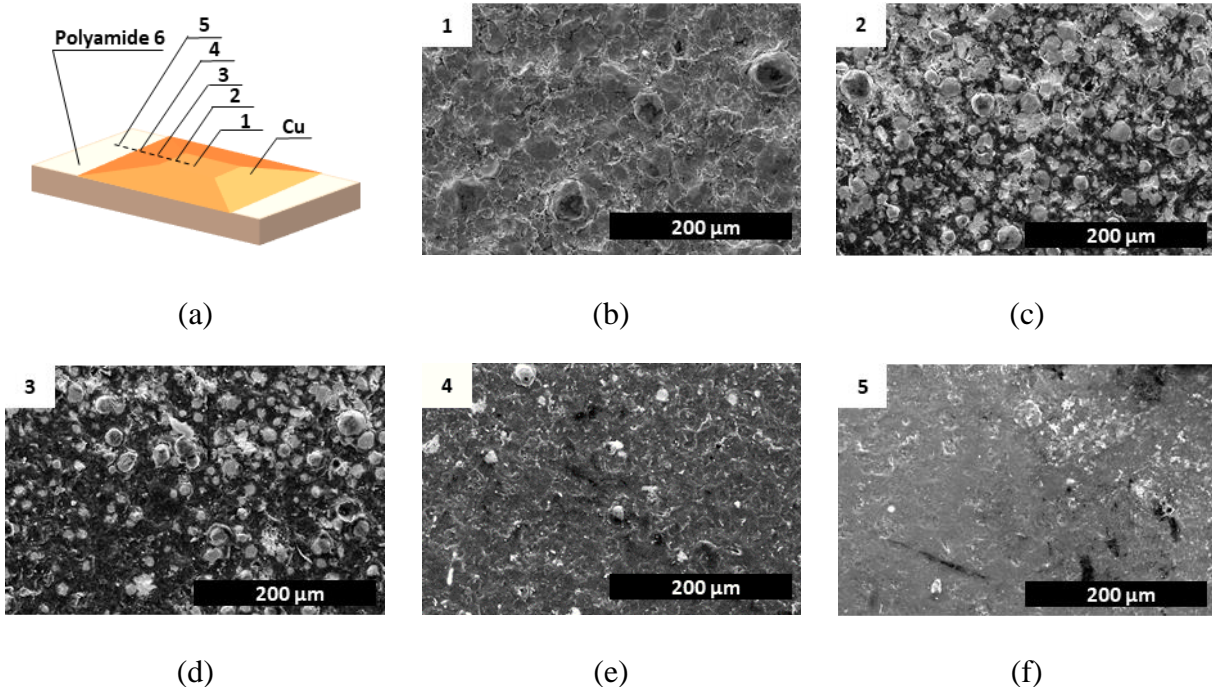


Figure 3-6 Cold spray region of interests (a) cold spray process and coated region (b) surface covered with Cu (c) surface mostly covered with Cu (d) surface partially covered with Cu (e) surface few Cu particle attached but predominantly polymer deform morphology (f) surface reveal crater impact images but no particle attachment

Figure 3-7 shows the cross-section of the particle mechanically interlock in the polymer substrate. Figure 3-7 (a) is the cross-section of the surface image in Figure 3-6 (b). The cross-section images show that particles are embedded in the polymer substrate and severely deform into flat shapes. The particle undergoes a multiple particle impact results the morphology being flattened eventually. Figure 3-7 (b) shows the cross-section of the region in Figure 3-6 (c). While the coated region in Figure 3-6 (c) is not directly under the cold spray nozzle, the particle is embedded in the polymer substrate but retains its spherical shape. The measured particle velocity under the nozzle was 350 m/s, and likely, the particle speed may decrease as it moves away from the center of the nozzle.

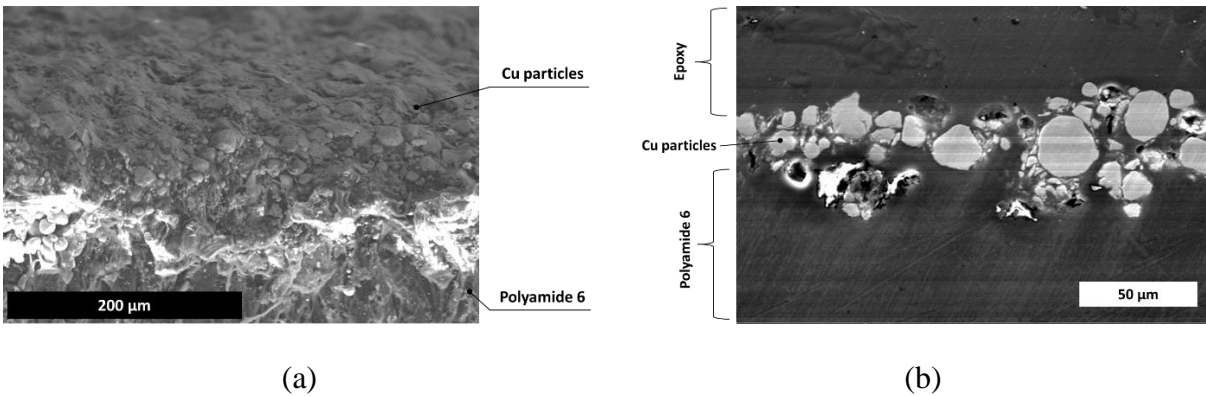


Figure 3-7 Cross-section of (a) surface morphology area 1 (b) surface morphology area 2

3.5 Conclusion

This study provides a simulation process that would predict cold spray metal particle deposition on polymer substrates, embedding the particle within the polymeric substrate as the primary actor for adhesion. The work was accomplished by using a three-network polymer model at a high strain rate response from the impact of the metal particle. After confirming the stability of the polymer model, the general setting in the FEA factor, such as mesh size and hourglass control, were studied to maximize the efficiency of numerical calculation. The material factors such as particle density, particle velocity, and particle size were also studied in this research. The results were visualized by examining the response of the particle rebound velocity and energy after the impact. The mapped diagram was established by considering all the above material factors in the cold spray process. This would benefit by showing which process parameters are more inclined

to cause the metal particle to be mechanically interlocked in the polymer substrate. Finally, a cold spray spherical Cu was coated on the polyamide 6 experimentally and agreed well with the predicted model. This work provides the necessary steps for building the numerical simulation of cold spraying on a polymer substrate.

4. MEASUREMENT METHODS FOR RELATING POWDER FLOWABILITY IN COLD SPRAY SYSTEM

The content of this chapter is submitted to a peer-reviewed journal.

Powder flowability is a factor in influencing the performance of mass flow rate in the cold spray system. The flowability of four powders Cu, Al₂O₃, Al, and Sn, with different particle morphology, size, and density, was investigated for cold spray applications. Good powder flowability is impacted by powder morphology and size distribution. Cold spray particle velocity was quantitatively measured with a double disk rotary system. The particle velocity increases with the increase of inlet pressure and temperature. The mass flow rate is measured from the hopper and the output of cold spray individually. Results show that the increase of the mass flow rate is a consequence of good powder flowability. A high mass flow rate indicates that the inlet pressure in the cold spray system plays a significant role in transporting the powder without powder clogging in the system. The described method, tools, and findings can be easily made with cost-effective and on-the-spot measurements.

4.1 Introduction

Cold spray is a promising technology for spraying temperature-sensitive materials and oxide layer materials. However, the feedstock particle preparation strongly affects solid-state coating methods, thus influencing the final particle velocity [82] [9, 83]. While increasing the inlet pressure will undoubtedly increase the particle velocity, the outcome of powder velocities depends on material and morphological characteristics. Thus, there is a need to demonstrate the relative effectiveness of powder chemistry and morphology related to process parameters such as input pressure and output mass flow rate.

Particle morphology, powder density, and particle size distribution affect the powder flowability in the cold spray system before injection into the accelerating nozzle. Powders must have good flowability into the cold spray nozzle to ensure a consistent coating [35, 84, 85]. Therefore, it would be advantageous if quantified measurements for the powder dynamic/flowability in the cold spray system could be connected with the coating process. With recent automatic technology updates, powder characterization techniques such as powder

flowability (angle of response, bulk/ tap density, and indexes such as the Hausner and Carr indexes) can be measured accurately and precisely. The measurement details such as the theory, reproducibility, accuracy, and resolution using commercial flowability measurements have been comprehensively studied by others [86-89].

Particle velocity is essential for determining the coating efficacy and efficiency in cold spray. A common way to measure the cold spray particle's velocity is by emitting a laser pulse at the sprayed area's vertical direction and simultaneously capturing the wavelength change from the high-speed camera. Synchronization between the camera and the laser needs to be designed carefully. This method can be expensive in terms of equipment and time-consuming. In this current work, a method for measuring particle velocity was adopted from systems used to measure abrasive particle velocity in erosion testing [90-94]. Details of the setup can be found in section 2.3.

According to ASTM B213 and ISO 4490, the method for quantifying the flow rate of metallic powders is by passing through a specified test orifice via gravitation. This testing method inspects the powder's flowability and minimizes external contact devices with the powders. However, although this testing method is a system-independent measurement of powder flowability, application of this method to cold spray may also be influenced by commercially common actions such as the hopper vibration rate, the input pressure into the cold spray nozzle, and the transporting devices' that influences the powders [95, 96]. Therefore, ASTM B213 and ISO 4490 still have a gap in directly applying powder flowability in the cold spray system, and users would benefit from measurement techniques that would directly apply to many cold spray systems, such as determining total mass flow rate and the powder feed rate measurements from the hopper.

Cyclone dust collectors are widely used in dust removal, mist, dissolved gases from a liquid stream, and recovery of spray particles, and the theory and application for cyclone dust collectors have been widely studied [97]. In the current study, we measure the mass flow rate in the cold spray system using a cyclone dust collector. The cyclone injects a centrifugal force, forms a circular vortex flow, and spins the dust to the chamber's outer wall, decreasing the particle velocity and eventually depositing into a container at the bottom of the cyclone. More information for the cyclone dust collector paper that addresses the design, CFD simulation and experiment results can be found in [98-100].

This research aims to investigate an experimental device for measuring cold spray particle velocity under different process conditions and, in addition, linking the relationships between powder morphology, powder size distribution, and the mass flow rate for quantifying the cold spray coating deposition efficiency shown in Figure 4-1. Furthermore, this study provides quantified cold spray process measurements to minimize the trial and error needed to achieve the coating's maximum output.

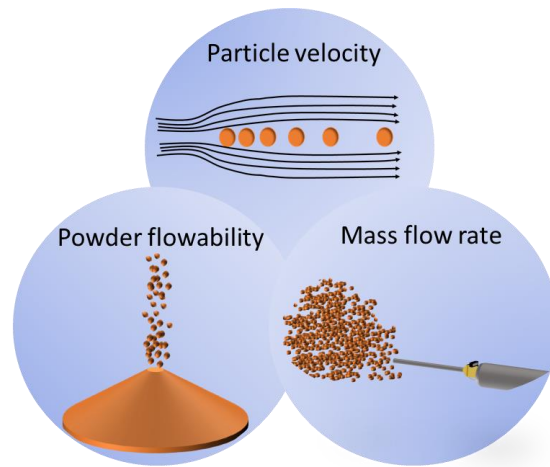


Figure 4-1 The connection between powder flowability, particle velocity, and mass flow rate

4.2 Material and methods

4.2.1 Material selection and process

Four commercially available powders, Cu, Al, Al_2O_3 , and Sn, were studied in this research. Powder information is summarized in Table 7. Cu powder is additionally added with a small portion of Al and Al_2O_3 . Adding a small portion of other powder to a base metal system is a common strategy for increasing the coating strength for the cold spray coating process. Powders size and shape distribution were measured with a Malvern Morphologi G3-ID Particle shape analyzer. The measured results agree with the information provided by the vendor. In addition, scanning Electron Microscopy (SEM) (Quanta 650 FEG) was used to observe the powder size and morphology.

Table 7 Feedstock powders information

Material	Commercial Supplier	Nominal particle size range (μm)
Cu	CenterLine	5-45
Al	Metal Powders USA	<44
Al ₂ O ₃	Inframat Advanced Materials, Inc.	5-45
Sn	CenterLine	5-45

This research's low-pressure cold spray system was a Cold Spray K205/407R model made by Rus Sonic Technology, Inc., a portable device for quick coating and repair. The cold spray system is composed of three major parts: 1. Hopper (feed rate controller from 1-10) 2. Controllable inlet pressure (0.4 - 0.8 MPa) and temperature controller (T1-T5) 3. Cold spray nozzle (CD/de Laval type nozzle). The temperature inside the nozzle can be heated between 200 °C to 600 °C (T1-T5). The parameters, such as the hopper feed rate, inlet pressure, and temperature, are studied to understand the correlations between each parameter.

4.2.2 Powder flowability measurement

A Granudrum (Awans, Belgium) was utilized to determine the powder flowability, quantified by the flow angle and the powders' cohesive index. It tests the powder dynamic flow, which we use to mimic the powder flowability in transferring the powder from the hopper to the cold spray nozzle. Figure 4-2 (a) shows the Granudrum is set up with a CCD camera placed in front of the drum for taking multiple images while the drum is rolling. Figure 4-2 (b) shows the acquisition process. The powders images taken from the CCD camera are shown in black images, while the air displaces a white background. The cohesive index is calculated from the powder/air interface fluctuation from the rotating drum's averaged images. The flowing angle was measured from the average images of the rotating drum. The cohesive index indicates the cohesion inside the powders (Van der Waals, secondary forces between the particle). The flow angle is characterized as the flowability of the powder.

A volume of 30-50 cc powder is usually poured into the drum. Afterward, the drum is placed onto a fixed stage to allow the drum to roll. All tests were conducted for the drum to rotate from 2-10 RPM with 2 RPM intervals. This speed range is to make sure the powder is flat while the drum rotates. For each RPM increment, 20 images were collected and averaged—the results of flow angle and the cohesive index are reported from each RPM average.

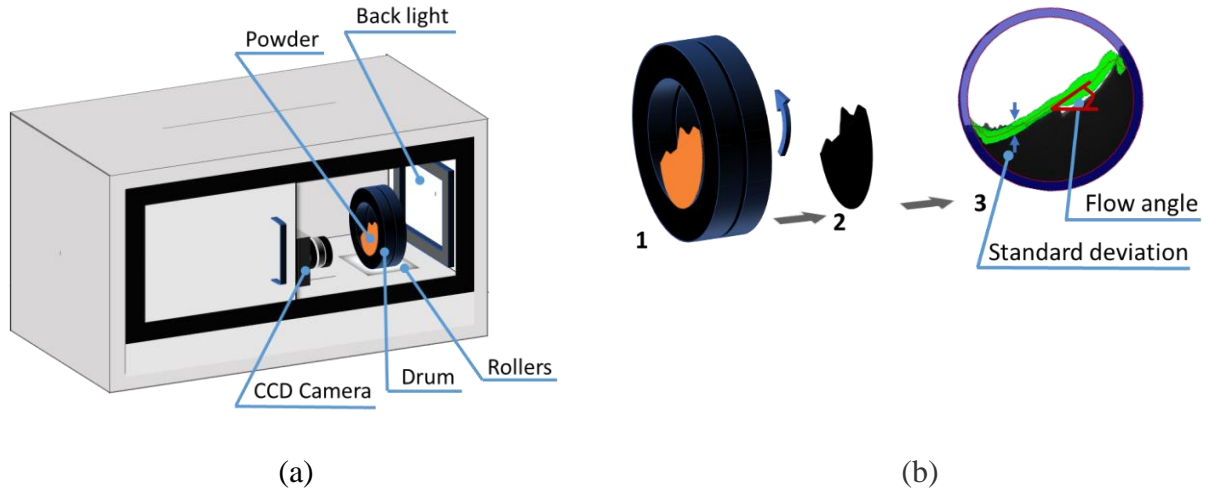


Figure 4-2 Schematic of the Granudrum device (a) the drum is placed in a cabinet while rotating, a CCD camera taking images (b) posting processing steps

Tap density was measured using a Granupack (Awans, Belgium), shown schematically in Figure 4-3 (a) and in cross-section in Figure 4-3 (b). The Hausner ratio is the most commonly used standard for measuring powder flowability in manufacturing processes like pharmaceuticals and additive manufacturing [86, 89]. It is defined as the ratio of tapped (bulk) density divided by initial bulk density. The packing fraction is calculated from the tapped density divided by the true density of the material. Therefore, the $n_{0.5}$ and the $\rho(\infty)$ are provided as well. The $n_{0.5}$ is the number of taps for reaching the middle of compaction. The $\rho(\infty)$ is a fitted parameter of the asymptotic volume fraction. Granupack's measurement helps understand the impact of the powder vibration process in the hopper.

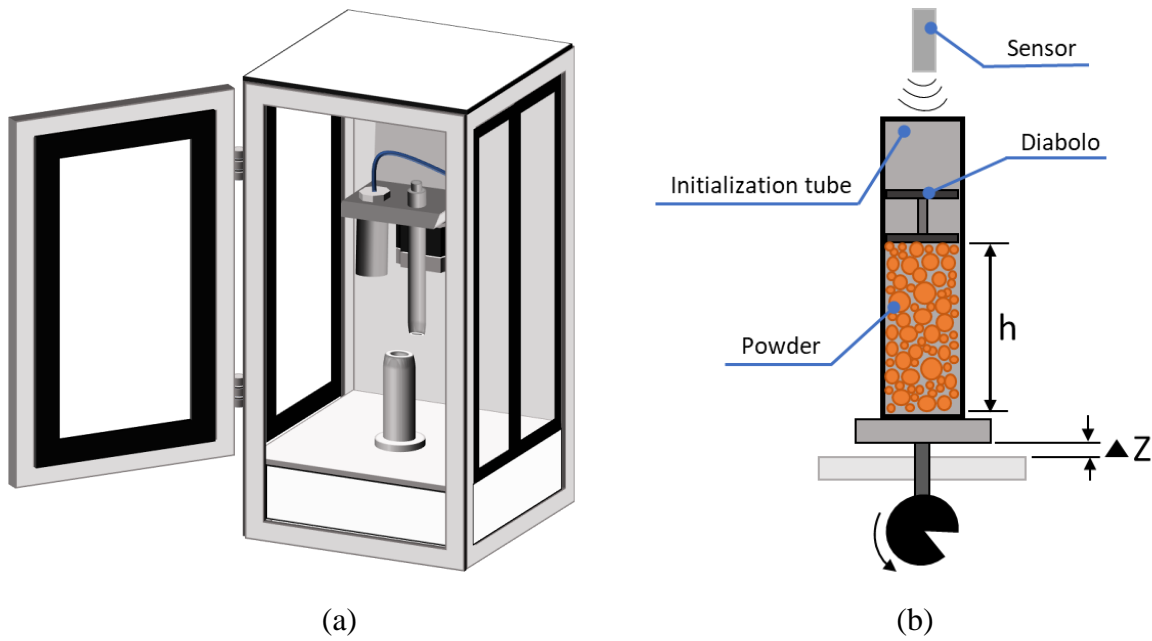


Figure 4-3 (a) Schematic of the Granupack device (b) The cross-section of the compact measurement device

4.2.3 Powder velocity measurement

Figure 4-4 shows the two plates rotary system combined with the cold spray system setup. In the left bottom corner is an example of the sprayed coated angle differences. The two-plate rotary original concept was adapted for measuring solid particles, mainly applied for air blasting (erosion) substrates [94]. The design involved two discs rotated on a shaft with a notch on the first disc. The plates rotate at a constant speed while particles traveling through the notch on the first plate impact the second plate. As a result, the particles' marking on the second plate and the notch on the first plate produce an angle difference. The bottom left corner of Figure 4-4 shows an example of the coated results. The angle differences are measured between the original point (red dot) to the coated spot (white spot- Al_2O_3 powders). The measured distances between the coated spot to the original point increases with decreasing particle velocity. This method provides a rapid, simple, and cost-effective measurement of particle velocity.

For this study, the input pressure is set between 0.4 - 0.6 MPa, the nozzle temperature is between room temperature to 220 °C, and the two plates are fixed rotating at 10,000 RPM. The distance between the cold spray nozzle to the second plate is 33 mm. After cold spraying particles

onto the second plate, the angle differences before and after sprayed are measured, and the particle impact velocity, v , can be calculated from (5):

$$v = \frac{\pi \cdot n \cdot S_0}{\xi} \quad (5)$$

where n is the rotational velocity of the disk, S_0 is the distance between the two disks, and ξ is the angular displacement.

The measured particle velocity is an average particle velocity from the cold spray system, affected by the particle size distribution, the distance from the substrate to the nozzle, the position of the airflow in the nozzle, etc. The measured average particle velocity is representative of all the individual particle traveling velocities. Four chosen powders are cold sprayed, and the particle velocity is measured. The powders are Al (2.7 g/cm^3), Al_2O_3 (3.95 g/cm^3), Sn (7.31 g/cm^3), and Cu (8.9 g/cm^3).

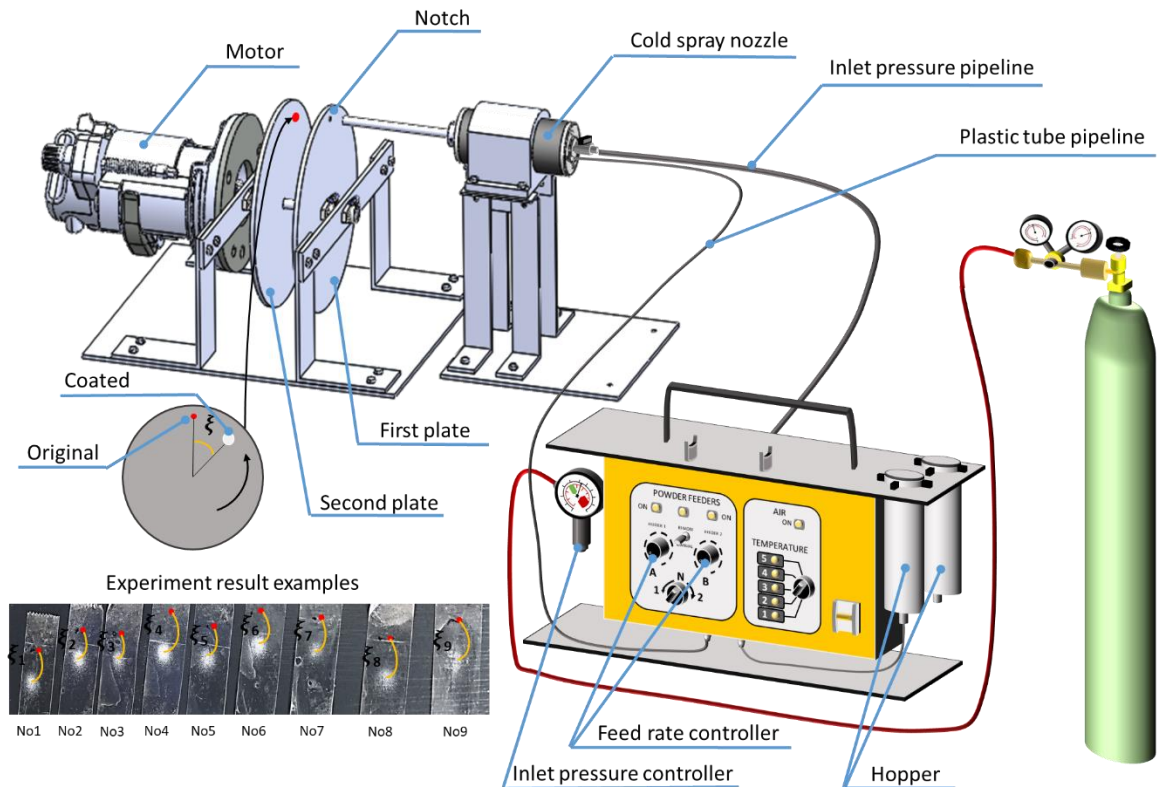


Figure 4-4 The setup schematic for measuring particle impact velocity

4.2.4 Mass flow rate measurement

Two separate measurements of mass flow rate were conducted. The first measurement is the powder collected from the hopper (hopper feed rate), and the second measurement is powder collected from the cold spray nozzle (mass flow rate). Each powder was poured separately into the hopper and the feed rate adjusted from 1-5 (low to high- hopper vibration frequency). Next, the hopper was detached from the cold spray system to measure the hopper feed rate individually. Finally, powders were collected at a fixed time and weighed.

The powder mass flow rate was measured through a cyclone dust collector via cold spray. Using cyclone dust collectors to measure the mass flow rate of the cold spray system benefits from separating the gas and the powders; besides, minor particles often flow out with the outlet gas. Therefore, cyclone design has much of the research focused on designing/simulating the gas cyclone dust for capturing the contaminants.

Figure 4-5 shows the cyclone geometry dimension and the cold spray system setup to measure the mass flow rate from the nozzle. The cold spray nozzle is fixed to the cyclone dust collector's inlet and cold sprayed for 30 seconds for each powder. The collection container is weighed before and after cold spraying powders. The powders were cold sprayed with increasing pressure from 0.4 – 0.56 MPa. It is assumed an increase in the inlet pressure; more powders are sprayed and collected. Particle sizes smaller than 1 μm can drastically affect the powder flows in the cyclone and often prove difficult to be captured [97]. The maximum particle size ($< 80 \mu\text{m}$) is set to avoid the nozzle's clogging for cold spray. Smaller particle sizes for cold spraying may prove difficult because of decreased kinetic energy and mass flow dynamics. The particles need to have a certain amount of mass to impact the substrate. Particle size of at least 10 μm is best for achieving critical velocity (no flow disturbance). Otherwise, smaller particles tend to deviate from the target trajectory. This simple device helps filter smaller particles while measuring the mass flow rate from the cold spray system.

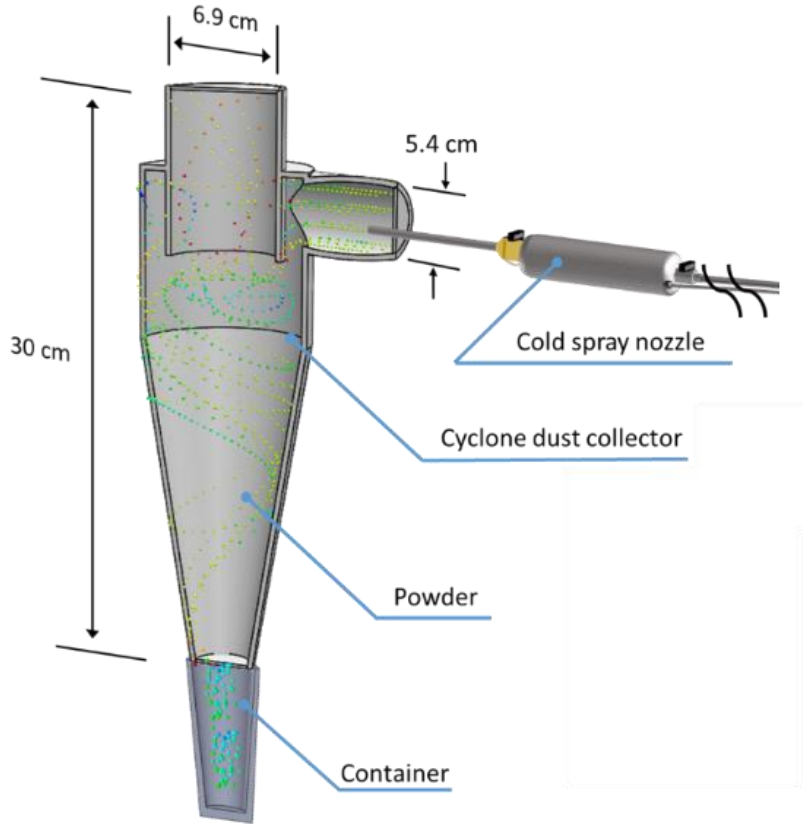


Figure 4-5 Cyclone geometry and the cold spray setup for the measurement of mass flow rate

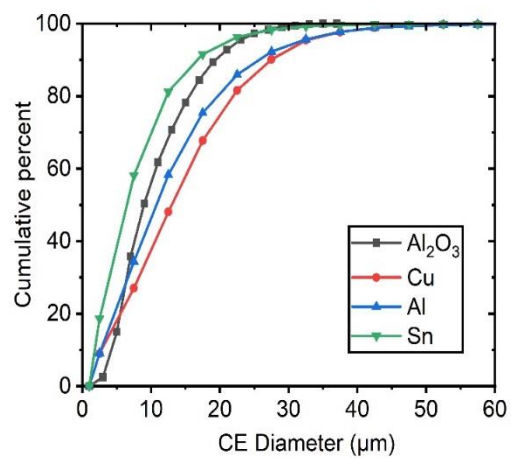
4.3 Results

4.3.1 Powder size distribution and morphology

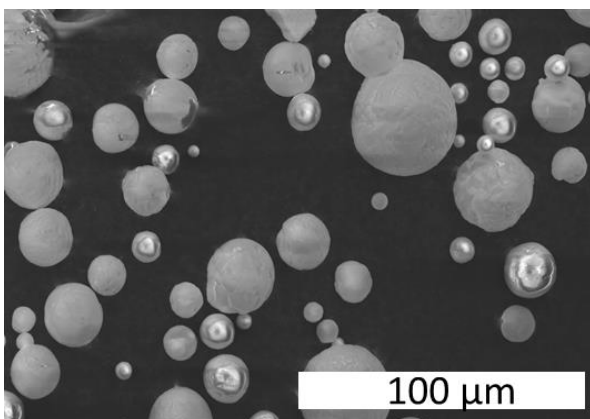
Figure 4-6 shows the powder morphology and size distribution for the materials in this study. SEM images show the spherical morphology of Al_2O_3 , Sn is mixed with an oval and spherical shape, and Cu and Al powders are mostly irregular shapes. CE (circular equivalent) particle size of D(0.1), D(0.5), and D(0.9) of all four powders are organized and listed in Table 8.

Table 8 The four powders size distributions (unit μm)

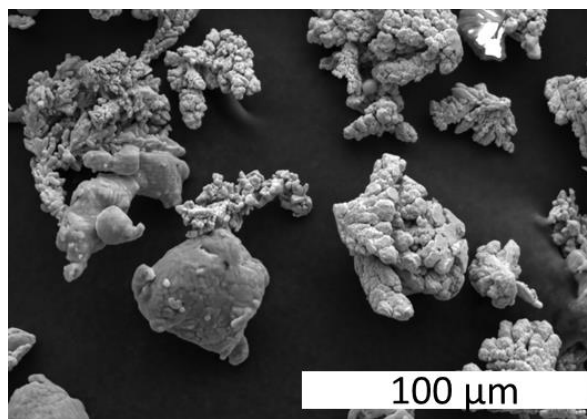
	D(0.1)	D(0.5)	D(0.9)
Al_2O_3	4.8	9	19
Cu (mixed)	3	13	27.5
Al	2.8	11.5	27
Sn	1.5	6.5	15



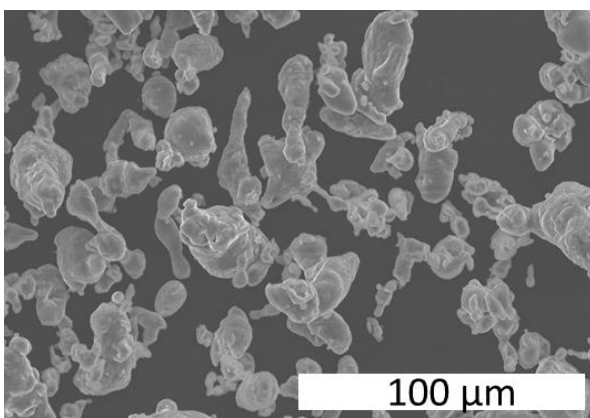
(a)



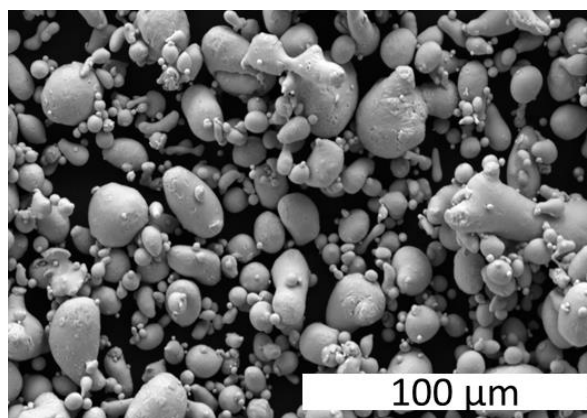
(b)



(c)



(d)



(e)

Figure 4-6 Particle size distribution (a) four powders and morphology of (b) Al_2O_3 (c) Cu (mixed) (d) Al (e) Sn

4.3.2 Powder flowability

Figure 4-7 shows the images taken from the Granudrum with four different powders rotating at 10 RPM. An average avalanche angle of results is collected from the Granudrum and represented in red line with a standard deviation plotted along (green line) in the images in Figure 4-7. A low flow angle indicates powders with good flowability and vice versa. Figure 4-8 (a) shows the powders' flow angles from 2 RPM to 10 RPM from a rotating speed. Al has the highest flow angle, and Sn has the lowest flow angle. Powders with a spherical shape are more inclined to have better flowability. According to the results in Figure 4-8 (b), good powder flowability can be ranked from $\text{Sn} > \text{Al}_2\text{O}_3 > \text{Cu} > \text{Al}$ (from good to poorly). Particle morphology and particle distribution determine the final powder flowability.

Figure 4-8 (b) shows the four powders' cohesion index with increasing rotating speed (RPM). The cohesion index's value is relatively constant with the four different powders at an increasing RPM. A low cohesive index indicates that powder is not likely to agglomerate while rotating in the drum. Powders with smaller sizes tend to agglomerate because of secondary force and moisture.

The statistical analysis is employed to determine if the flow angle depends significantly on the increasing rotation speed (RPM). A two-sample t-test compared the min. and max. rotating speed (RPM) of the measured four powders flow angle. The statistic test results determine if the hypothesis can be rejected or not at a certain significant level. If the p-value is less than 0.05 would result from the rejection of the null hypothesis that the two measured flow angles are the same. Statistical results in Table 9 of the flow angle compared with the two rotating speeds are no different at the 5 % significance level for Al_2O_3 , Cu, and Al; the null hypothesis can be rejected (p-value > 0.05) while Sn cannot be rejected (p-value < 0.05). Results show that the flow angle of Sn decreases as the rotating speed increases (shear-thinning). This result shows the same in decreasing cohesive index. While Al_2O_3 , Cu, and Al of the flow angle and cohesive index are consistent with increasing rotational speed (RPM).

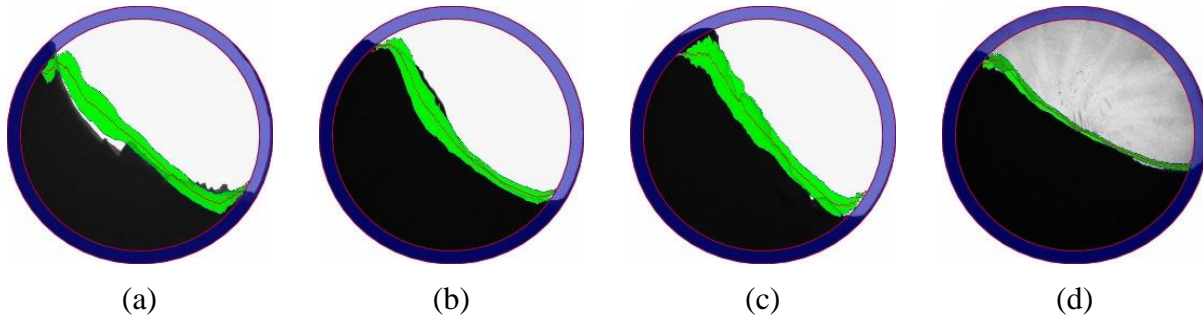


Figure 4-7 Images of (a) Al_2O_3 (b) Cu (c) Al (d) Sn from Granudrum at 10 RPM

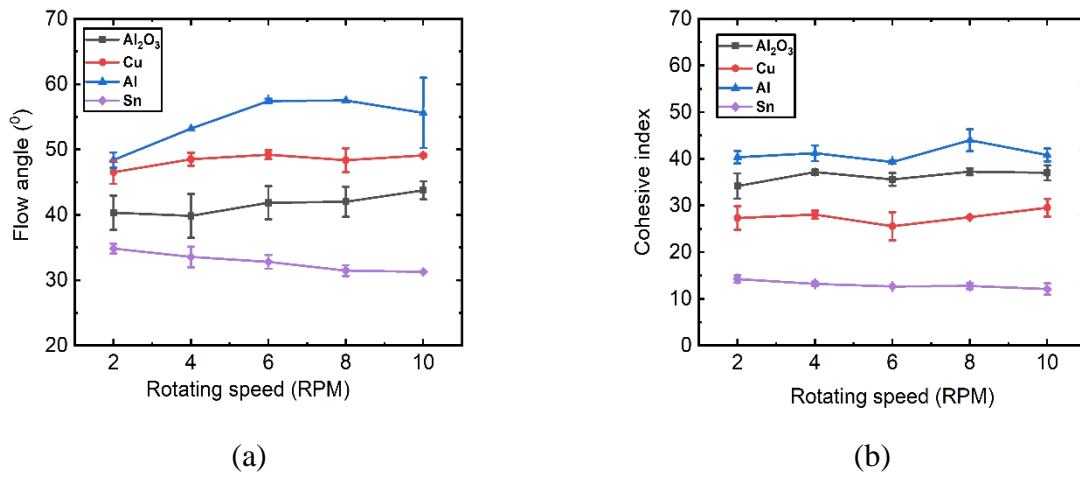


Figure 4-8 The four different powders at an increasing RPM with the function of (a) flow angle (b) cohesive index

Table 9 Statistical analysis of the four different powders flow angle with rotating speeds

Powder rotating speed (RPM)	Flow angle Avg.	Flow angle St. dev.	p-value (t-test) for the effect of rotating speed
Al_2O_3 (2) / (10)	40.34 / 43.75	2.64 / 1.38	0.48
Cu (2) / (10)	46.53 / 49.09	1.79 / 0.16	0.38
Al (2) / (10)	48.38 / 55.61	1.17 / 5.38	0.42
Sn (2) / (10)	34.84 / 31.28	0.77 / 0	0.01

When pouring the powders into the cold spray system's hopper, the constant vibration causes the powder bed's compactness to change. The Granupack instrument measured this research's powder tap density changes and plotted them in Figure 4-9. The parameters extracted from the curves in Figure 4-9, such as initial density, tapped density, tap number (n_0 and n_n) to reach the compaction ($n_{1/2}$), Hausner ratio, and $\rho(\infty)$ are organized and summarized in Table 10. The tap density is influenced by the powder's properties such as particle distribution, morphology, etc., and cohesion force such as Van der Waals forces. Lumay, et al. [88] has provided evidence of the correlation between the grain size/powder cohesive with the Hausner ratio (Hr) ($\rho(500)$ divided by $\rho(0)$). Powder with high cohesiveness increases the value of the Hausner ratio (Hr). A high Hr ratio means the powder tap density at $\rho(500)$ has a higher value than $\rho(0)$. Thus, the Hr ratio indicates the powder's cohesiveness differences. Results show that Sn (oval) has the lowest ratio (excellent flow), whereas Al (passable flow) has the highest ratio (Hr ratio indication can be found McGlinchey [101]). This measurement also agrees well with the results in Figure 4-8 (a) and Figure 4-8 (b).

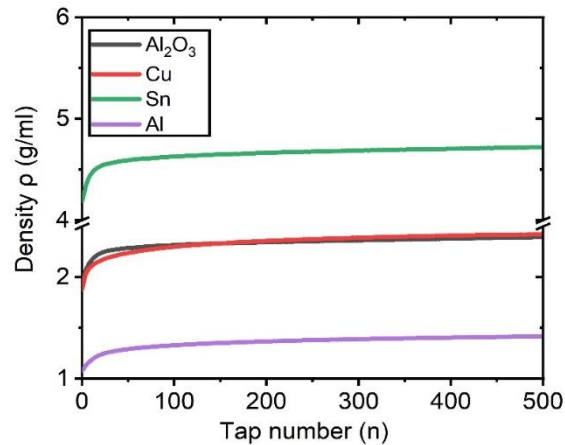


Figure 4-9 The tap density of four different powders

Table 10 Tap density measurement from the Granupack

Powders	$\rho(0)$	$\rho(500)$	n_0	n_n	$n_{1/2}$	Hr(500)	$\rho(\infty)$
Al ₂ O ₃	1.96	2.39	0.66	0.62	11.28	1.22	2.52
Cu (mixed)	1.88	2.42	0.21	0.27	17.87	1.29	2.62
Al	1.08	1.42	0.4	0.52	24.28	1.31	1.55
Sn	4.19	4.72	0.57	0.65	9.75	1.13	4.87

4.3.3 Particle velocity during cold spray

Figure 4-10 shows the results of particle velocity from the measurement of the two-plate rotary device with the function of input pressure vs. temperature (a) Sn (b) Cu (c) Al (d) Al_2O_3 . The mapped results show that the measured particle velocity increases with the increase of input pressure and temperature. Thus, the two-plate rotary device was able to measure the particle velocity with process parameters changes. Particle velocity variance between each of the particles can be observed in the map diagram. The measured variance from these four powders is affected by particle density, particle size, particle distribution, and particle morphology shown in Figure 4-6 and organized in Table 10. Although many factors may influence particle velocity, particle density may play a significant role in determining the final output of particle velocity—higher mass results of slow particle velocity and vice versa. Overall, the map results indicate that the decrease of particle density results in a higher particle velocity; for example, Al at the max input pressure and temperature have a higher particle velocity than Sn.

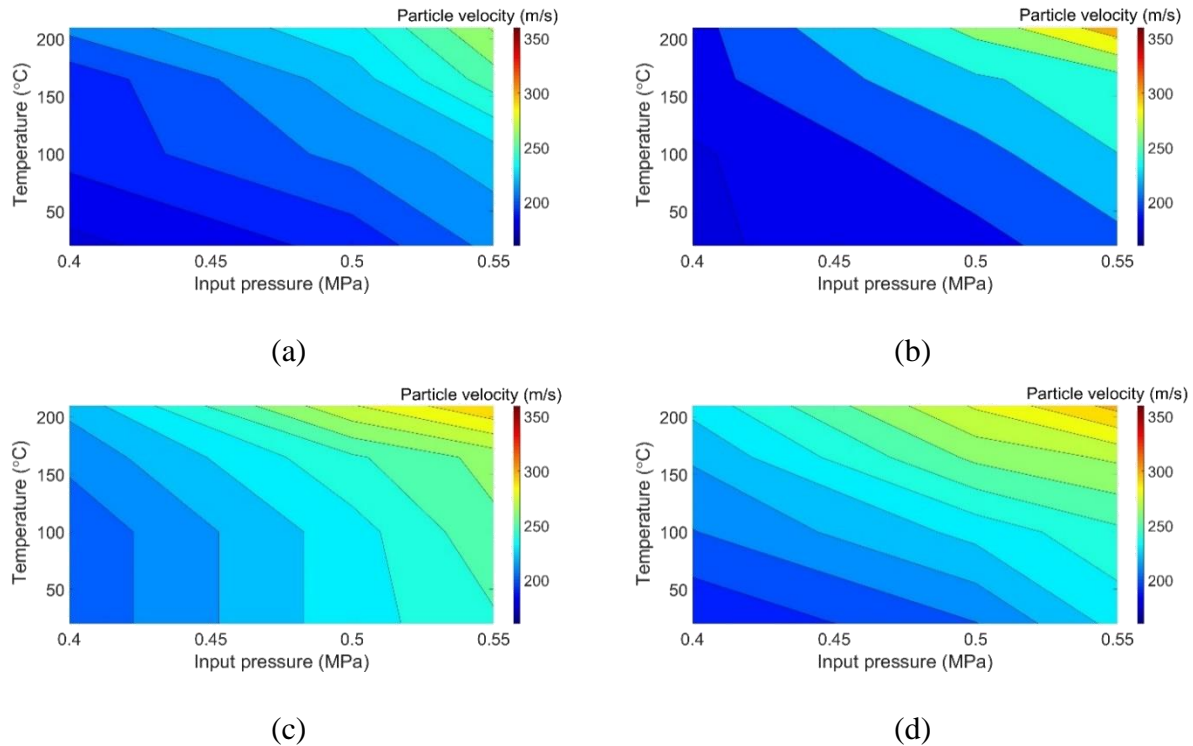


Figure 4-10 The measurement of particle velocity (a) Sn (b) Cu (c) Al (d) Al_2O_3 with the function of input pressure (MPa) and temperature

4.3.4 Mass flow rate

Figure 4-11 shows the hopper feed rate plotted with the function of inlet pressure. The output results show a mass flow rate distribution amount the four different powders Cu, Al₂O₃, Al, and Sn from the cold spray. Results show that the mass flow rate increases with the hopper feed rate in Figure 4-9 (a-d). Sn powders have the highest mass flow rate by increasing the inlet pressure, while Al has the lowest. It is interesting to observe that Al powders are less collected than the other three powders. Figure 4-8 shows that Al powders have poor powder flowability compared to Sn, but it also has a relatively low particle density, shown in Table 10. Figure 4-10 shows that Al has a higher particle velocity compared to the other three powders. The measured results in Figure 4-9 and Figure 4-10 provided a contrast difference by looking at the hopper feed rate, particle velocity, and mass flow rate. It is suggested that a high mass flow rate decreases particle velocity.

The overall mass flow rate does not always equal the hopper feed rate at a fixed amount of time. Generally, the results show that the cold spray nozzle's measured mass flow rate is higher than the hopper feed rate measurement. Increase hopper feed rate; there's a potential of powders not enough time to flow into the cold spray nozzle. Figure 4-11 (a-d) shows that increasing inlet pressure results in higher particle velocity (higher pressure differences) and increased powders collected in a fixed amount of time. While the hopper feed rate adjusts its vibration frequency, it still proportionally controls the powder feeding into the cold spray system. With increasing inlet pressure, the convergent size of the cold spray nozzle has a pressure variance between the hopper, which causes a strong absorption force; as the inlet pressure increases, a slightly higher mass flow rate than the hopper feed rate. Thus, integrating each device is essential for ensuring powders can be successfully transported without clogging the cold spray system.

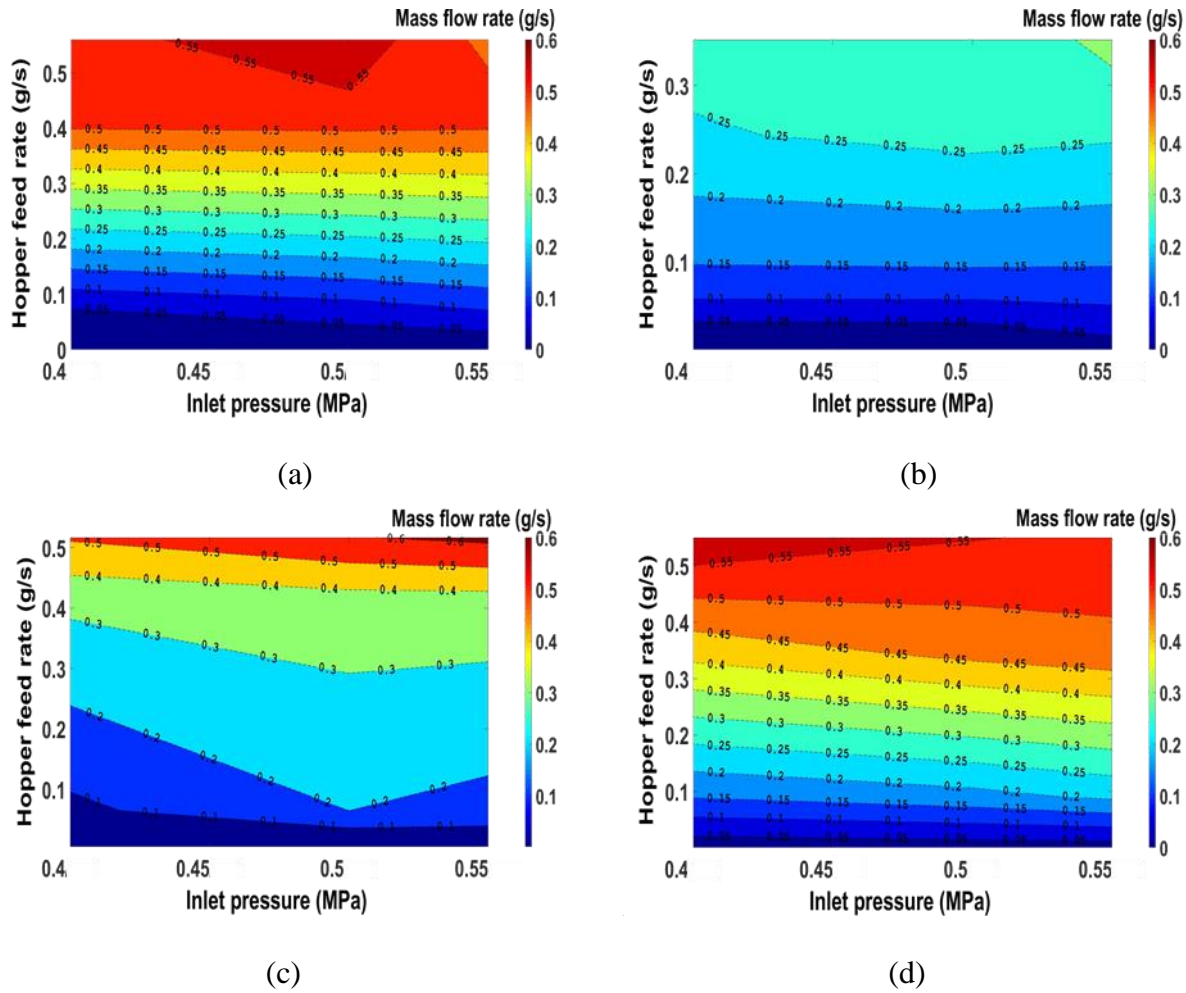


Figure 4-11 The measurements of the mass flow rate with the function of hopper feed rate and the inlet pressure (a) Sn (b) Al (c) Al_2O_3 (d) Cu

4.4 Discussion

Figure 4-12 (a) shows three hopper feed rates (from low to high) with the functions of powder flow angles. As the hopper vibration frequency increases, the results show that powder with a higher flow angle in the Granudrum has collected less than a similar density powder with smaller flow angles. Figure 4-12 (b) shows the volume flow rate plotted with the powder flow angles at three hopper feed rates. The volume flow rate is from the hopper feed rate divided by the density $\rho(\infty)$ in Table 10—the volume flow rate increases with increasing flow angle. The morphology and size distribution plays a role in the hopper's powder flowability. For example, a high volume flow rate suggests that powders are typically irregular shapes compared to a more

spherical shape with a lower volume flow rate. Conversely, a high volume with a lower mass flow rate results from a low powder flowability (high flow angle).

Figure 4-12 (c) shows the connection between powder flow angle (flowability) and the powder's mass flow rate with increasing hopper feed rate (from low to high). Figure 4-8 (a) shows the flow angle results with RPM fixed at 6. Increasing the inlet pressure with the mass flow rate measurements was also considered. The results are plotted as a standard deviation with each mass flow rate measurement. When the hopper feed rate increases, the mass flow rate decreases with increasing flow angle.

Figure 4-12 (d) shows the volume flow rate between the four powders' flow angles. The volume flow rate is calculated by taking the mass flow rate and divided by the tap density ρ (∞) in Table 10. The volume flow rate shows an increasing trend as the flow angle increases, and as the hopper feed rate increases, the volume flow rate at a specific flow angle reaches its highest rate. The higher the hopper feed rate, the more particle flows into the cold spray nozzle and may clog the nozzle without adequate inlet pressure. The trend of volume flow rate in Figure 4-12 (d) is similar to Figure 4-12 (b), and thus powder flowability impacts the cold spray performance and plays a vital role from the hopper to the cold spray deposition.

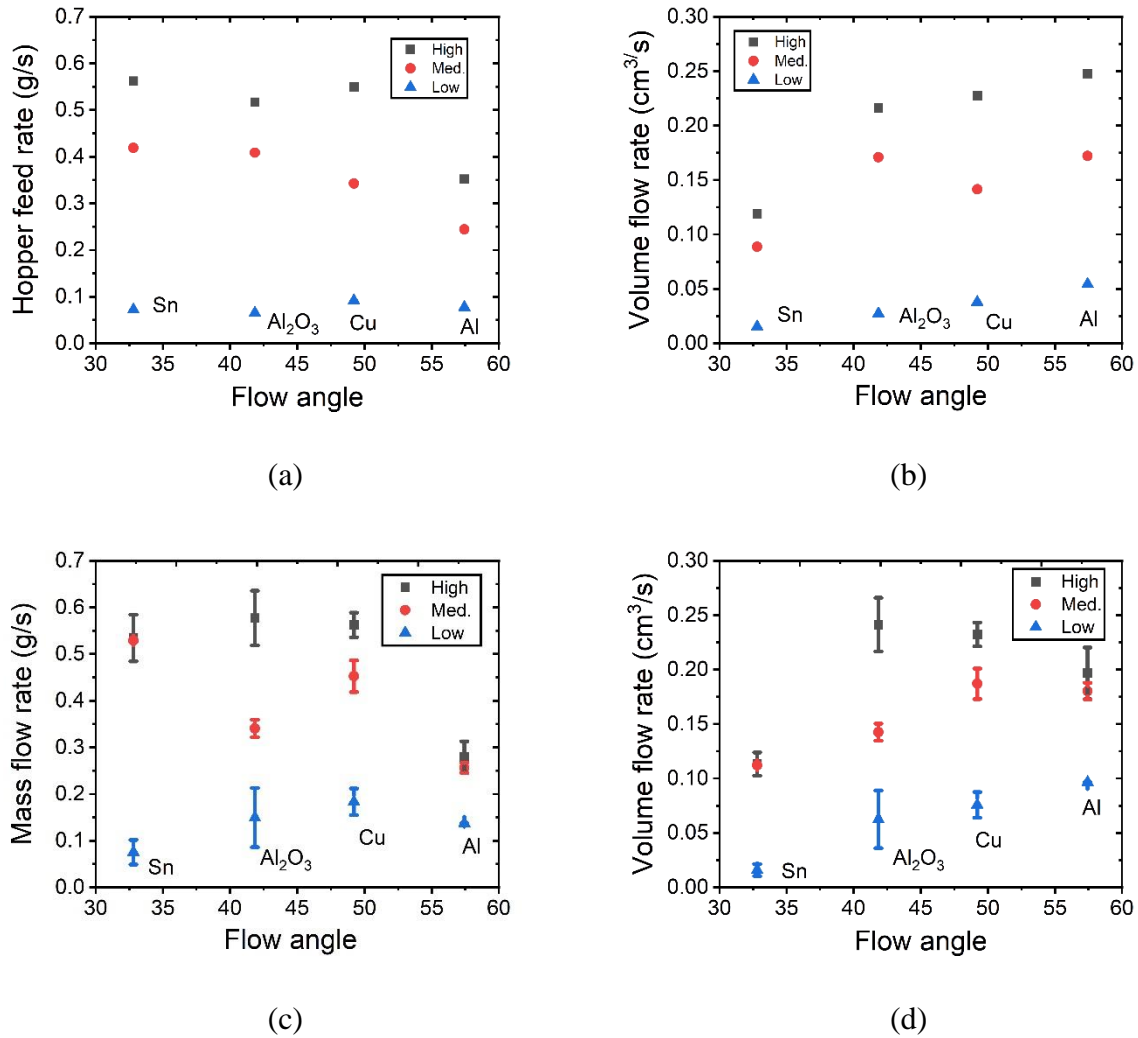


Figure 4-12 Measurement of Sn, Al_2O_3 , Cu, and Al flow angle with the function of (a) hopper feed rate (b) volume flow rate (hopper) (c) mass flow rate (d) volume flow rate (cold spray)

4.5 Conclusion

Powder flowability, particle velocity, and mass flow rate are measured in the cold spray system. This research has measured the particle velocity of four different powders: Al, Sn, Cu, and Al_2O_3 . The particle velocity increases with increasing accelerating pressure and temperature—the cold spray mass flow rate increases with cold spray inlet pressure and the hopper feed rate. A mapped diagram from four different powders provided a range of output mass flow rates with inlet pressure and hopper feed rate inputs. The mass flow rate depends more on the hopper feed rate

than the inlet pressure. In addition, particle morphology and powder distribution affect the powder flowability, which indirectly influences the mass flow rate from the vibration of the hopper to the cold spray nozzle. Powders with a lower flow angle have a higher mass flow rate, relatively lower particle velocity, and a lower volume flow rate than powders with higher flow angles. This correlation provides valuable information for the future user to effectively determine the spray conditions.

5. ESTABLISHING A COLD SPRAY PARTICLE DEPOSITION WINDOW ON POLYMER SUBSTRATE

The content of this chapter was published in the Journal of Thermal Spray Technology (Tsai et al., J Therm Spray Tech **30**, 1069-10800 (2021)). DOI: <https://doi.org/10.1007/s11666-021-01179-x>

A set of processing conditions for cold spray deposition of an embedded particle layer on a polymer substrate has been established using a dynamic impact model and verified experimentally. This research utilizes a three-network polymer model based on high strain-rate impact tests to capture polymer deformation's non-linear and time-dependent response with rigid and deformable particles during the cold spray impact. The particle's material properties, velocity, and size were systematically studied to obtain the polymer deformation's various responses from finite element analysis. Particle impact velocity was experimentally measured with a double disk rotary system. The numerical results were mapped into diagrams and validated with the experimental results of cold spraying Cu and Al₂O₃ powders. This research contributes to quantifying the deposition window, which embeds but still exposes metallic/ceramic powders on a polymer substrate.

5.1 Introduction

Cold spraying metal or ceramic particles on polymer substrates may increase the anti-abrasive, anti-bacterial, and anti-corrosion of the polymer substrate. Cold sprayed particles do not require pre-heating, and thus, benefits from any powder coating without the involvement of oxidation. The cold spray technique provides easy maneuverability of the sprayed pattern, a large coating area of surface, and no high spraying temperature requirement. These advantages benefit industrial efficiency and provide an affordable, robust, and rapid method for coating applications[17, 19].

Prior studies [1] have reported that the primary method of providing adhesion of a cold-sprayed coating onto a polymer substrate uses mechanical interlocks of the metal/ceramic particles onto the substrate. Particles within the substrate generally preserved their original shape. Cold spraying of copper (Cu) particles onto substrates such as polyurethane, high-density polyethylene, polypropylene, polyamide 6, polytetrafluoroethylene, and polycarbonate showed a general trend that increasing spray pressure allowed deeper penetration, which could be enacted by increasing

the propelling gas pressure. However, the polymer jetting around the embedded Cu particle was influenced by particle penetration and subsequent layer deposition. Jetting caused the material to cover the Cu particle and further continue on the polymer substrate's metallization. The plastic deformation of the polymer has a significant impact on the penetration depth. In a previous study Chen, et al. [32] has modeled the metal particle impacting a polymer substrate in cold spray coating using the Johnson-Cook plasticity model in the finite element analysis (FEA). The complexities of the deformation behavior of metals and polymer high strain rates predict particle embedding and substrate deformation challenges. They often develop a process parameter window for cold spraying onto the polymer substrate via a trial error process.

The mechanical response of many polymers at high strain rates is available in the literature [2, 41, 42, 72, 73, 102-104]. Typically testing equipment such as Hopkinson bar, Taylor Impact, and Transverse Impact is used to conduct polymer deformation strain rates to validate the polymer model. Some studies Kendall and Siviour [47] also incorporate polymer impact testing at a low strain rate with temperature consideration. Models for describing large strain polymer network deformation include the eight-chain model, the full network, and the crosslink-sliplink model [105]. A thorough derivation, verification, and validation have been done by Bergström and Boyce [106] [107-109]. The polymer network model can be arranged in series or parallels to describe polymer deformation's large strain deformation and strain rate dependence. The three network polymer model was used in this study as it sufficiently describes a semi-crystalline polyamide 6,6 under large plastic deformation [42].

Cold spray deposition still faces difficulties in coating metals on polymer substrates. Typically, a single particle can impinge on the polymer substrate and either embed or recoil from the substrate. Continuous particle coating on a polymer substrate remains challenging and recoil. Generally not only wastes the powders but destroys the already coated surface. Prior studies have addressed a qualitative process window for spraying [17, 20]. Still, the lack of understanding between the coating process's connection and the material structure (as-sprayed substrate) remains. Many simulations to predict process parameters consider metal (particles) impacting metal (substrates) [18, 20, 21, 30]. These simulation results demonstrated that particle/substrate morphology changed with increasing velocity and addressed the kinetic energy to bond the interface. However, quantitative simulation for metal/ceramic to polymer coating remains relatively unexplored.

To address the above issue, the current study uses a polymer model implemented in an FEA code to capture the response of metal and ceramic particles impacting a polyamide substrate and to define conditions where the particle (both those which may deform, Cu, and those unlikely to plastically deform, here chosen as ceramics for a stiff model particle) will embed and provide a basis for subsequent will adhered coatings. The polymer model used was based on experimental high strain-rate impact results. A range of parameters such as particle velocity, particle size, and the material property was studied to understand the influence of mechanical attachment of the particle onto the polymer substrate. The FEA's numerical results were compared and validated with experimental measurements of embedded/adhered metal and ceramic particles.

5.2 Experimental procedures

5.2.1 Material selection and process

Two types of commercial powders were used in this study: Aluminum oxide (Al_2O_3) and Cu. Both suppliers specified a minimum purity of 99.99%. The average particle size was measured by a Malvern Morphologi G3-ID Particle shape analyzer (Malvern Instruments Ltd, UK), and the results are listed in Table 11. Figure 5-1 shows the spherical morphology of Al_2O_3 and Cu taken from the Scanning Electronic Microscopy (SEM, FEI Corp., Quanta 650 FEG, USA). It does show the presence of some satellite particles on the alumina, which charge during imaging conditions.

Table 11 Feedstock powders properties

Powders	Morphology	Supplier	Density (g/cm^3)	Particle size range (μm) (Vendor)	D_{50} (μm) (Measured)
Al_2O_3	Spherical	Inframat Advanced Materials Inc.	3.95	5-45	10
Cu	Spherical	Chemical Store Inc.	8.96	5-44	36

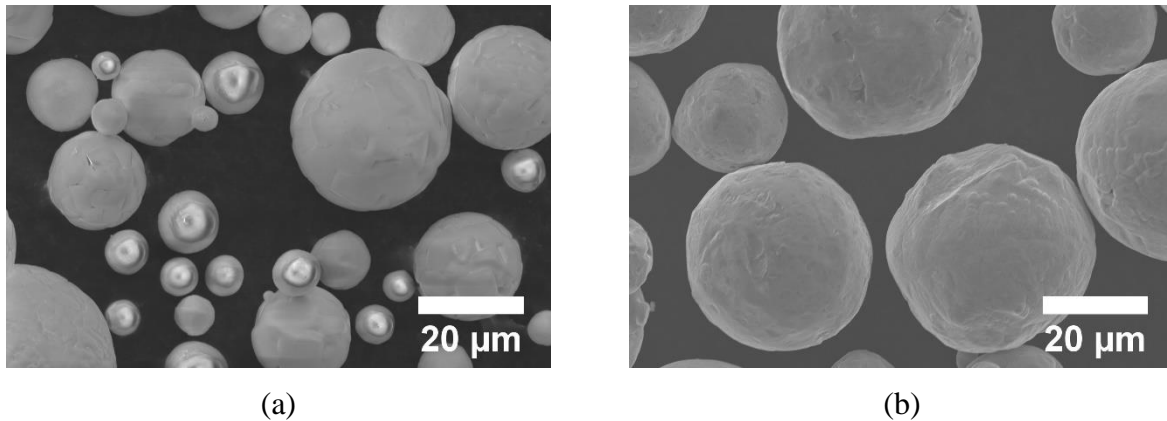


Figure 5-1 SEM images of (a) Al_2O_3 (b) Cu

The substrate chosen for this study was a polyamide 6,6 sheet with a thickness of 3.175 mm (ePlastic Co., USA). The polyamide 6,6 was cut into strip coupons according to the ASTM D638-14 [110]. Cold spray deposition was carried out using a low-pressure Cold Spray K205/407R model made by Rus Sonic Technology, Inc. The air pressure was connected through the converging-diverging (CD) nozzle. The input pressure into the cold spray nozzle was adjusted following the target particle velocity. The distance between the spray nozzle to the polymer substrate is set as 30 mm, gun traverse speed 10 mm/sec. The spray gun was fixed to the z-axis while allowing the nozzle to move freely only on the x and y-axis. The microstructure of the as-sprayed specimens was investigated using the Scanning Electronic Microscopy (SEM, FEI Corp., Quanta 650 FEG, USA).

5.2.2 Two-disk (plate) rotary system

The particle velocity is a crucial model input in defining the process window for creating a well-adhered coating on a polymer substrate where the particles are embedded in the substrate. So, rather than assuming linearity with applied gas pressure, this research used a simple device to measure the particle velocity. Figure 5-2 shows the setup of the two-disk rotary system for particle velocity measurement. The two-disk rotating system consists of a shaft with two plates of a fixed separation distance on the metal rod, based on prior instruments used to measure shot velocity in peening operations [24] research. To capture the particle velocity expected for cold spray (higher than in shot peening processes), a minimum speed of 10000 RPM was used to capture the particle

impact velocity. An example of the cold spray Cu particle onto the second plate is shown in Figure 5-3.

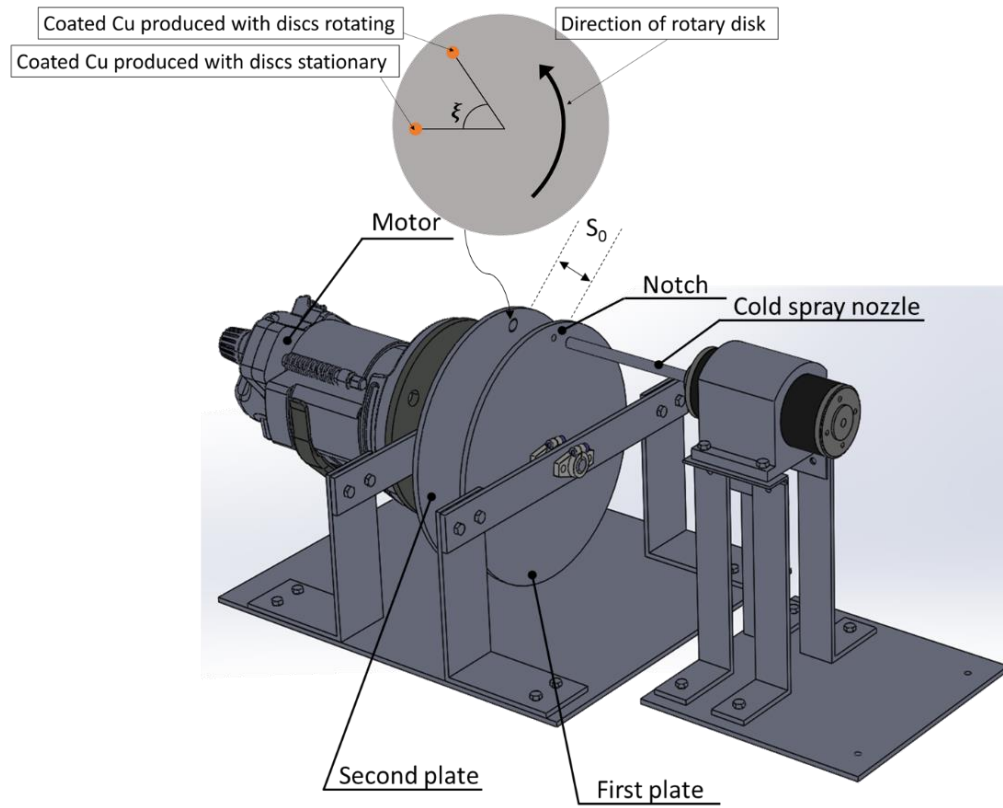


Figure 5-2 The setup of the two disk rotary system

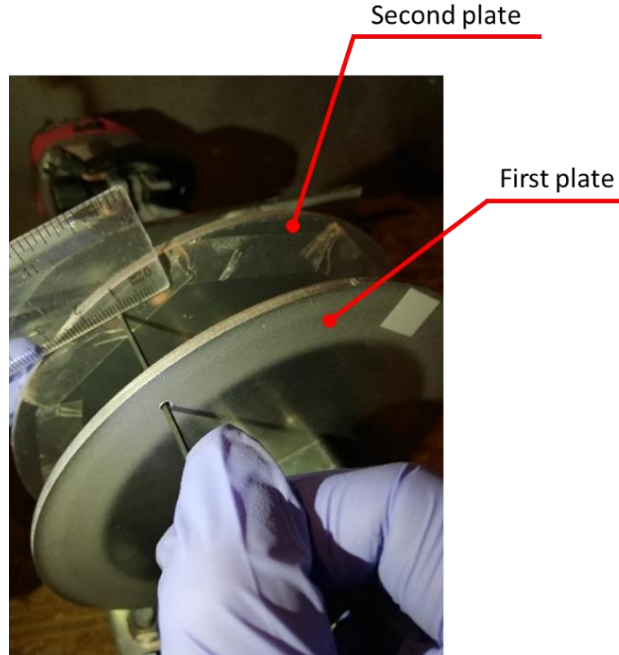


Figure 5-3 The experiment result shows the coating marked on the second plate

This cold spray system's input air pressure (i.e. pre-nozzle) was between 0.4-0.65 MPa. The two plates rotate at 10,000 RPM, and a tachometer (Extech RPM 33) was used to measure the rotational speed. The distance between the cold spray nozzle to the second plate is 33 mm. While the two-disk plate system was rotating, the particles were sprayed through a notch on the first plate, leading to deposition onto the second plate. The angle differences were to be measured compared to the first and the second plate. The particle impact velocity, V , is in (6):

$$V = \frac{\pi \cdot n \cdot S_0}{\xi} \quad (6)$$

where n is the rotational velocity of the disk (rad/min), S_0 path of a particle between the first and the second plate, and ξ the angle differences from the initial position

Cu particles were used to quantify the input pressure correlation with particle impact velocity, as shown in Figure 5-4. Five different input pressures values within 0.4 to 0.65 MPa were tested for particle velocity. Each set was done five times, and the standard deviation was plotted along with the average. In the experiment, a range of particles is cold sprayed through the plate. It

is noteworthy to mention that the average particle impact velocity likely on many factors such as particle size, nozzle stand-off distance, driving gas condition, and is non-linear in our current system, demonstrating the need to measure velocity if that is to be one of the parameters in the model. The observed 10 % standard deviation is typical for this type of measurement compared to other published research results [90, 91].

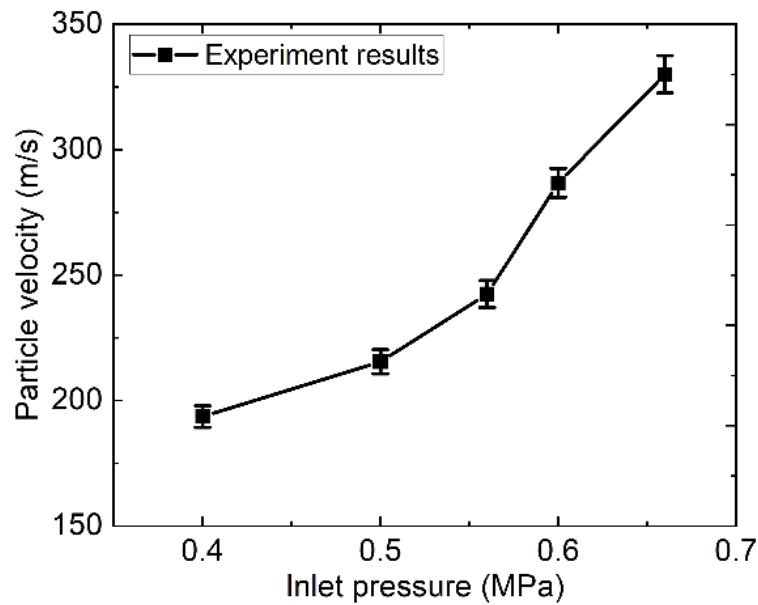


Figure 5-4 The measured output of particle velocity as a function of input air pressure for this cold spray system

5.3 Numerical method

5.3.1 Material model

Cold spray deposition of Cu particles on polyamide 6,6 substrate was simulated using a three network polymer model from references [103, 106-109]; this model consists of three parts (molecular networks) connected in parallel [111]. A schematic representation of the model is shown in Figure 5-5. The three networks are stated as A, B, and C. The first two parallel networks A and B, described the semicrystalline's initial deformation and the amorphous domains. It is

assumed that the temperature is constant at room temperature 273 K. In contrast, network C represents a substantial strain after the initial response from the first two parallel networks A and B. The rigorous calibration and the validation of the three-network polymer model have already been done by others [42, 103, 106-109, 112]. Therefore, the available results were produced from the high strain rate of polyamide 6,6 to calibrate the three-network polymer model for the cold sprayed polymer substrate. The following constitutive equation is shown in (7), (8), and (9):

$$\sigma_A = \frac{\mu_A}{J_A^e \bar{\lambda}_A^{e*}} * \frac{\mathcal{L}^{-1}(\frac{\bar{\lambda}_A^{e*}}{\lambda_L})}{\mathcal{L}^{-1}(\frac{1}{\lambda_L})} * dev[b_A^{e*}] + \kappa(J_A^e - 1)I \quad (7)$$

$$\sigma_B = \frac{\mu_B}{J_B^e \bar{\lambda}_B^{e*}} * \frac{\mathcal{L}^{-1}(\frac{\bar{\lambda}_B^{e*}}{\lambda_L})}{\mathcal{L}^{-1}(\frac{1}{\lambda_L})} * dev[b_B^{e*}] + \kappa(J_B^e - 1)I \quad (8)$$

$$\sigma_C = \frac{\mu_C}{J \lambda_{chain}} * \frac{\mathcal{L}^{-1}(\frac{\lambda_{chain}}{\lambda_L})}{\mathcal{L}^{-1}(\frac{1}{\lambda_L})} * dev[b^{e*}] + \kappa(J - 1)I \quad (9)$$

where $J_A^e = det[F_A^e]$, $b_A^{e*} = J_A^{e-2/3} F_A^e (F_A^e)^T$, $\bar{\lambda}_A^{e*} = (tr[b_A^{e*}/3]^{1/2})$, $\mathcal{L}(x) = coth(x) - \frac{1}{x}$, μ_A and μ_C is the shear modulus of network A and network C, λ_L is the locking stretch, μ_{Bi} and μ_{Bf} are the initial and final shear modulus of network B, and κ is the bulk modulus.

As shown in Figure 5-5 (a), the total effects of the Cauchy stress in the polymer system is given by the sum of the stresses in the three-network polymer model. The material constants were formulated from the experimental results of a Split Hopkinson pressure bar test applied to the polymer substrate. The material constants were optimized, and the material constants showed an R^2 fitting of 0.974 compared with the experimental results plotted in Figure 5-5 (b). The material constants used in the current study are given in Table 12. Engineering stress with time is plotted in Figure 5-5 (c). The input of the experiment results has a strain rate of 3000 s^{-1} . A range of polymer strain rates $1000\text{-}3000 \text{ s}^{-1}$ was used as an input to ensure the material constants agree well

with the experimental results. While still having a good fitting with the experiment results, the material constants might vary. Although specific input ranges are adjusted for each material constant, the various output would still show a potentially good fit with the experimental results. Multiple trials were conducted to narrow down the parameter ranges. In this study, Drucker stability was tested to evaluate the consistency of the material constant for the three-network polymer model. The material constants with the highest uniaxial compression strain range were chosen, ranging from 0 to -0.7. The true strain versus true stress was plotted for various strain rates from 1 s^{-1} to 10^5 s^{-1} in Figure 5-5 (d).

Table 12 Material constants used in the three-network model (Polyamide 6,6 substrate)

Material property	Material constants
μ_A (MPa)	94.124
λ_L	3.59
Kappa (MPa)	5000
μ_{Bi} (MPa)	367.67
μ_{Bf} (MPa)	116.68
β	9.16
μc	$5.53 \cdot 10^{-5}$

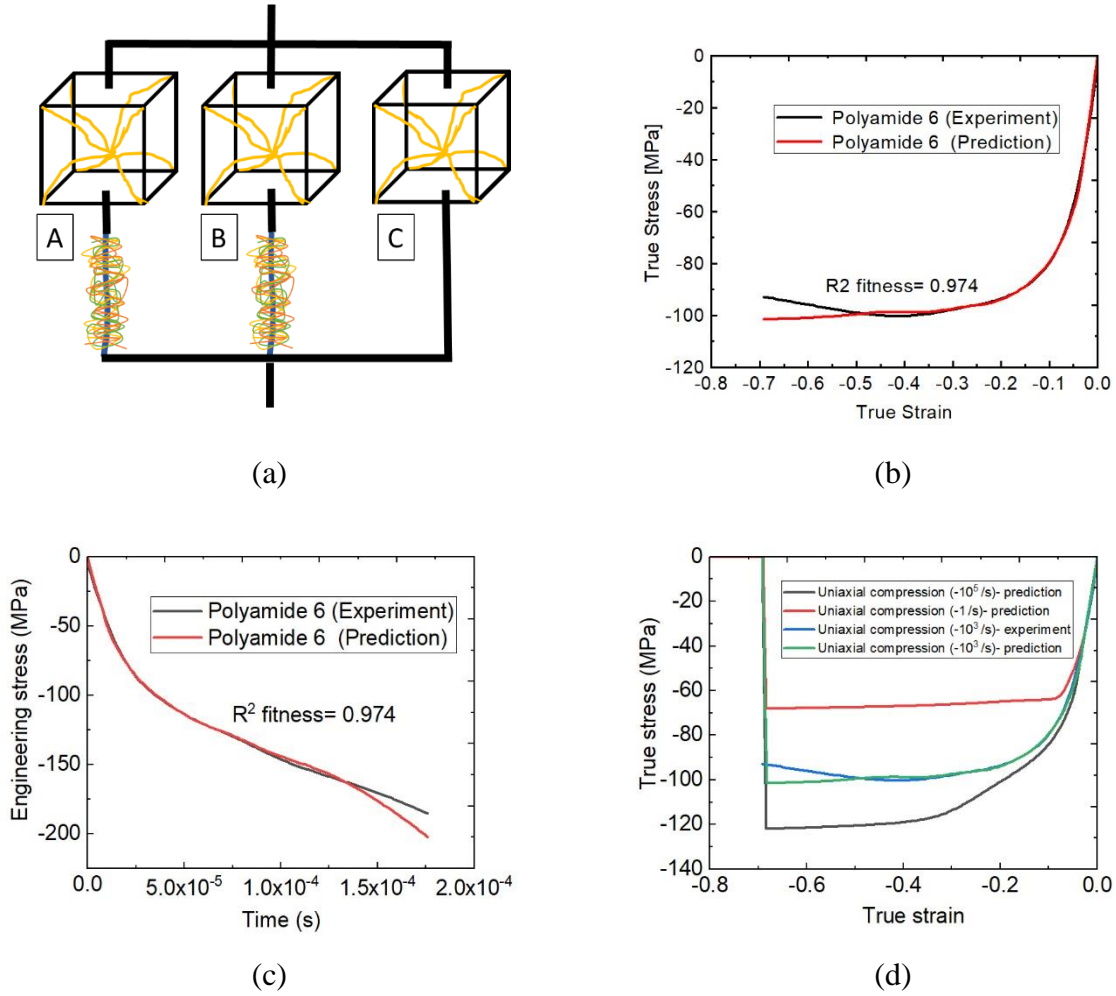


Figure 5-5 (a) Schematic of the constitutive models for polyamide (b) Stress vs. strain (c) Stress vs. time (d) Stress vs. strain at a strain rate range from -10^0 to -10^7

The simulation of a single Cu particle impacting the metal substrate has been widely studied [30, 33]. Results show that the Preston-Tonks-Wallace (PTK) model does well results capturing the metal deformation geometry after cold spray impact [71], Rahmati and Jodoin [113]. Other alternatives, such as modifying the Johnson-Cook (J-K) model at a specific range of strain rates, accommodate the stress softening during high-speed impact [59, 61, 62].

The J-K plasticity model has been assigned to describe the Cu particle's deformation when it impacts the polymer substrate. The metal particle plastic deformation is not the focus in this study because of the particle impinging into a soft material; less to no plastic deformation should occur on the metal particles. Thus, using the J-K plasticity model should be sufficient. The material constants for the material model are listed in Table 13. The Cu material deformation used the J-K

plasticity model that considers strain hardening, strain rate hardening, and thermal softening. The formula is described as (10):

$$\sigma = [A + B\varepsilon^n][1 + C \ln \dot{\varepsilon}^*][1 - T^{*m}] \quad (10)$$

where A is yield stress, B is hardening constant, C is strain rate constant, n is hardening exponent, m is thermal softening exponent, and T is temperature variation

Table 13 Cu material constants used in the Johnson-Cook plasticity model

Material property	Material constants
$\rho(\text{kg/m}^3)$	8.9×10^3
G (GPa)	44.7
A (MPa)	90
B (MPa)	292
n	0.31
C (MPa)	0.025
m	1.09
T_m (K)	1356
T_o (K)	298

A calibrated Ducker-Prager plasticity model, with the equation of state and Johnson-Cook rate dependence, was used to describe the Al_2O_3 impacting on the polymer substrate in the FEA simulation (which expected to show little if any plastic deformation). The material constants were taken from the Johnson-Holmquist (JH-2) ceramic material models and rearranged the Ducker-Prager plasticity model's equations to describe the Al_2O_3 particle impacting the polymer substrate [114-117]. As a result, the Drucker-Prager exponent yield criterion is provided as (11):

$$F = aq^b - p - p_t \quad (11)$$

and (12):

$$p_t = a\sigma_c^b - \frac{\sigma_c}{3} \quad (12)$$

where a and b are material parameters, p_t is the hardening parameter, and σ_c uniaxial compression stress.

Rearranging the equation (11) and below shows equation (13):

$$q = \frac{1}{a^{\frac{1}{b}}}(P + P_t)^{\frac{1}{b}} \quad (13)$$

Equation (8) has a similar expression compared with the JH-2 model, and therefore comparing the equation of the JH-2 model, the engineering constants are calculated in Table 14.

Table 14 Al₂O₃ material constants used in the Druker-Prager plasticity model

Material property	Material constants
$\rho(\text{kg/m}^3)$	3.95×10^3
G (GPa)	91
P_t (GPa)	0.2
a	0.0029799
b	1.67
σ_c (GPa)	1.76
C	0.0091
C_0	576000
S	0.5

5.3.2 Simulation properties

A single Cu and Al₂O₃ particle impacting a polyamide substrate were simulated using FEA software (Abaqus/Explicit 2018) with the Lagrangian approach. A ¼ of the symmetric model was conducted due to the nature of the axisymmetric geometry. Figure 5-6 (a)-(b) shows designed geometry and boundary conditions. It was assumed that a perfectly spherical shape particle impacts on the substrate in the vertical direction. The geometry was partitioned to accommodate the mesh element and mesh density. The bottom substrate is encastre, while the surfaces on both sides are symmetrical. The symmetric boundary conditions were applied to both the X-plane and the Z-plane of the substrate geometry. The particle undergoes an adiabatic process, and both the particle and the substrate are selected as C3D8R (average strain an 8-node linear brick with reduced integration).

The particle and the substrate interaction used the available General contact, which is a node-to-surface method. When the failure criteria are met, the elements are deleted. This ensures the particle continues impacting into the polymer substrate with the interior element eroded

smoothly. The hard contact model was used for the pressure-overclosure relationship. A finite sliding formulation was also used to allow the particle to move between the substrate during the impact. The interaction between the particle and the substrate uses the Coulomb friction model for modeling the friction. The friction coefficient is set as 0.002. This assumes the particle travels at a high impact velocity that friction plays less of a role in adhering to a polymer substrate. The particle and substrate ratios research limits the geometry size while maintaining a practical computation calculation. Most articles have pointed out that the particle impact onto the substrate causes the stress to propagate and reflect onto the particle because of the boundary condition set on the substrate [59, 61]. A parametric study effect of the particle and the substrate ratios, mesh size, and hourglass control have been done. This parametric study showed that the particle: substrate ratio can be set as 1:5 without influencing the stress wave reflection.

Furthermore, the mesh size and hourglass control effect were examined to compare mesh dependency while using the hourglass control to mitigate mesh distortion. The results showed that with mesh size set for the particle as $0.15 d_p$ and the substrate as $0.1 d_p$ required less computation time while the particle's rebound velocity remains consistent with increasing mesh size (The d_p stands for particle diameter). While the particle is traveling at a high impact velocity, it is assumed the material reaches a specific strain range and fracture at the polymer substrate's contact region. In this research, it was assumed that the polymer substrate failures as the strain reaches 1.4.

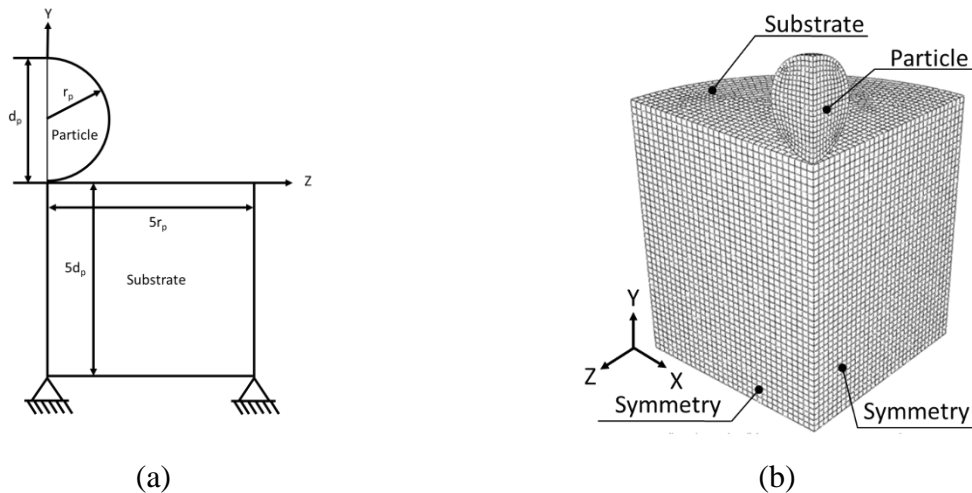


Figure 5-6 (a) Initial conditions used for the impact of the metal particle on the substrate (b) Mesh geometry and the schematic view of the FE model

5.4 Results and discussion

Figure 5-7 (a) shows an example of the polymer substrate interlocking the embedded Cu particle (30 μm) with the particle impact velocity at 300 m/s. The particle generally retains its original shape while penetrating the polymer substrate. Figure 5-7 (b) shows the total energy distribution diagram. The total energy is the total amount of friction dissipation energy, internal energy, and kinetic energy. The total energy is constant with increasing time. In addition, internal energy is the total amount of plastic dissipation energy, strain energy, and artificial energy. Each of the energy quantities shows the total equivalent amount adding towards the internal energy with increasing time. The plastic dissipation energy rises significantly with the decrease of the kinetic energy. The strain energy increases as the particle impact the polymer substrate. As the particle kinetic energy reaches the lowest value, the strain energy and the internal energy are highest. After, the strain energy starts to decrease as the portion of the energy is transferred to the kinetic energy and the plastic dissipation energy, allowing the particle to rebound.

Eventually, the kinetic energy goes to zero, and the particle is interlocked in the polymer substrate. Figure 5-7 (c) shows the substrate strain's evolution, and the particle velocity increases with time. Finally, the strain energy recovers 43%, resulting in the strain energy transferring parts of its energy onto the particle and causing the particle to rebound. Four different times were extrapolated and sub-plotted in Figure 5-7 (c) to show each FEA result. In case (1), the particle penetrates the polymer substrate. In case (2), the particle begins to rebound with the polymer substrate recovery. For cases (3) and (4), the particle separates from the polymer substrate's bottom but remains attached to the polymer substrate.

Figure 5-8 (a) shows the Al_2O_3 particle (30 μm) rebound after impacting the polymer substrate at 300 m/s. The plastic strain is shown in the polymer substrate, while no plastic deformation occurs on the Al_2O_3 particle. Figure 5-8 (b) shows the total energy distribution diagram. The total energy is constant with increasing time, and each portion of energy adds up to the total sum of the total energy. The result shows that the Al_2O_3 particle retains 19.5% kinetic energy after impacting the polymer substrate. The Al_2O_3 particle retains a large portion of kinetic energy with increasing time and allows the particle to rebound. This shows that with the same particle size and impact velocity, Al_2O_3 particles are likely to rebound compared to Cu particles.

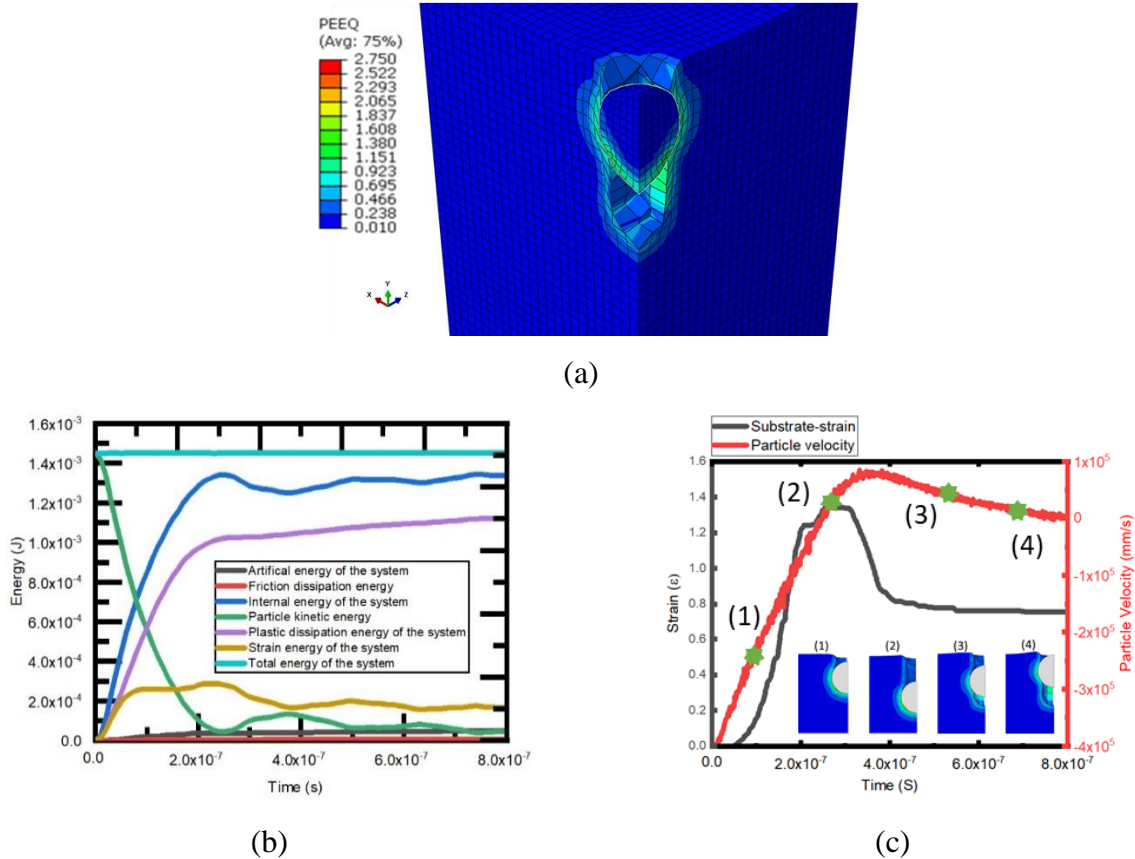


Figure 5-7 (a) Plastic strain distribution of the particle (Cu) and the substrate (Polyamide) (b) Evolution of energy distribution (c) Strain and particle velocity in 30 μm particle and the substrate during the entire process at an impact velocity of 400 m/s

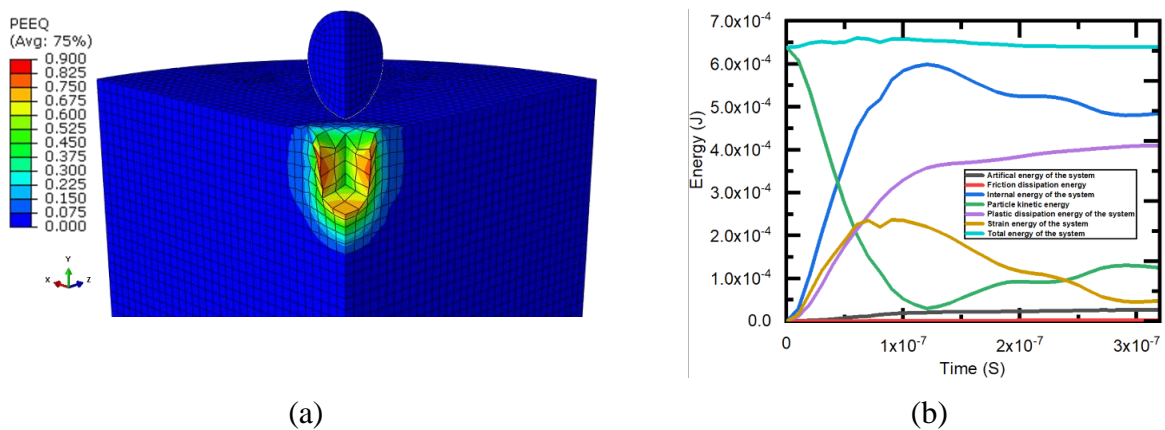


Figure 5-8 (a) Plastic distribution for the particle (Al_2O_3) and the substrate (Polyamide) (b) Evolution of energy distribution

The rebound velocity for all cases between particle velocity from 100- 500 m/s and particle size from 10 μm -50 μm was conducted. The rebound velocity results were then plotted as the kinetic energy lost (η) shown in Figure 5-9. The formula for a fraction of kinetic energy lost (η) (14)

$$\eta = \frac{V_{in}^2 - V_r^2}{V_{in}^2} \quad (14)$$

where V_{in} is the particle impact velocity and V_r is the particle rebound velocity.

When the η is close to 1, the particle is sticking, and closer to 0, it departs from the substrate. The rebound velocity is considered in this research to identify the particle interlocking in the polymer substrate (particle sticking in the substrate). The lower the rebound velocity, the particle is more inclined to adhere to the substrate. This concept assumes that a high-speed particle penetrates the substrate. However, in plotting as the rebound velocity or kinetic energy, the η value was chosen to be plotted. This is because η value gives more precise, normalized, distinct results indicating the particle is more prone to stick onto the polymer substrate with increasing particle size and impact velocity.

Figure 5-9 (a) and (b) show the η with increasing particle size and particle velocity of the Al_2O_3 and Cu. The plotted diagram shows the particle size in the field of 10-50 μm for reflecting with the commercial particles distributed range in Figure 5-1. The η value in the mapped diagram shows that Cu with the same particle size compared with the Al_2O_3 has a better chance of coating on the polymer substrate under the same particle velocity. Al_2O_3 particles need a particle velocity of higher than 400 m/s to have a η higher than 0.9 for the particle to be coated on the polymer substrate. As to Cu, particle velocity reaching 300 m/s already has η value higher than 0.9. The total kinetic energy of the particle dictates the overall polymer substrate deformation. At constant particle velocity, the increased particle size increased the kinetic energy and vice versa. With increasing particle size and particle velocity, particles are inclined to adhere to the polymer substrate. However, with the mapped η value, a quantitative region can be predicted—the mapped diagram provided information for narrowing down the coating parameters' prospect. The simulation results give future users a minimum effort to coat on a polymer substrate without

wasting time and material. Thus, the objective is to understand the particle's minimum η value to attach to the polymer substrate. Vertical lines were drawn upon Figure 10 (a) and (b) at particle velocity 200 m/s and 300 m/s (Al_2O_3 and Cu). Figure 10 (a) shows that Al_2O_3 at 200 m/s and 300 m/s have a η value smaller than 0.8, resulting in no coating. In Figure 10 (b), the η value shows that Cu particles at an impact velocity of 300 m/s with particle size range higher than $20\text{ }\mu\text{m}$ ($\eta > 0.9$) were able to be successfully coated onto the polymer surface. In contrast, Cu at 200 m/s was not successfully ($\eta < 0.75$).

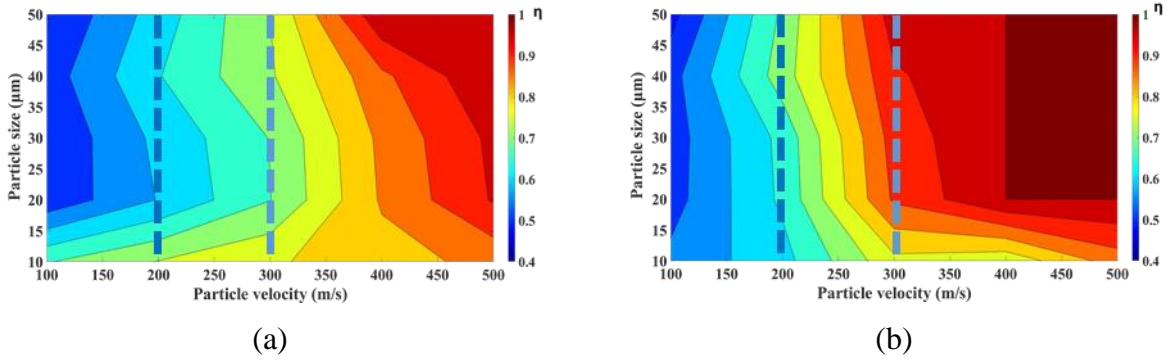


Figure 5-9 Effect of particle size vs. particle velocity (a) Al_2O_3 (b) Cu

Al_2O_3 and Cu particles at 300 m/s and 200 m/s were cold sprayed onto the polymer substrate, as shown in Figure 5-10 (a)-(b) and Figure 5-11 (a)-(b). The particle velocity was controlled by the input pressure with the results provided in Figure 5-4. In Figure 5-10 (a)-(b), the experiment results show that only Cu particles attach to the polymer substrate at 300 m/s. The Cu particles coverage on the polymer substrate was 31 %. Simultaneously, Al_2O_3 rebounded from the polymer surface with particle velocity at 300 m/s (a few Al_2O_3 residual particles were present but not as significant as Cu particles attaching onto the polymer substrate). No large coating of particles is attached to the polymer surface with the particle velocity at 200 m/s, shown in Figure 12 (a) – (b). The surface of the polyamide shows the traces of the particle rebound after cold spray. Thus, the simulation results in Figure 5-9 show that Al_2O_3 and Cu agree well with the experiment results in Figure 5-11 (a)-(b). The experiment results also show that the particle size embedded in the polymer substrate is generally bigger than $10\text{ }\mu\text{m}$. The simulation results of an Al_2O_3 and Cu of $30\text{ }\mu\text{m}$ size impacting the polymer substrate at 300 m/s are shown in Figure 5-12 (a)-(b). Results show that Cu remains in the polymer substrate while Al_2O_3 already rebounds from the polymer

substrate at the same amount of time. Figure 5-13 (a)-(b) shows the Al_2O_3 and Cu particle impact velocities at 300 m/s and 200 m/s of the cumulative particle size distribution and the η with increasing particle size. The η value from Figure 5-9 (a) and (b) is superimposed in Figure 5-13 (a)-(b). Results indicate that particle size increases and result in a decrease of η value. Figure 5-13 (a) shows Al_2O_3 particles distribution low η at 300 m/s and 200 m/s. Figure 5-13 (b) shows that Cu particles have a high η relative 300 m/s over 200 m/s. As Figure 5-10 (b) shows, the Cu has a coverage of the polymer surface of 31%. Thus, Figure 5-13 (b) assumes particle size accumulation is about 69 %. The η value is about 0.92, which η value closer to 1, guarantees a high coverage of the polymer material substrate.

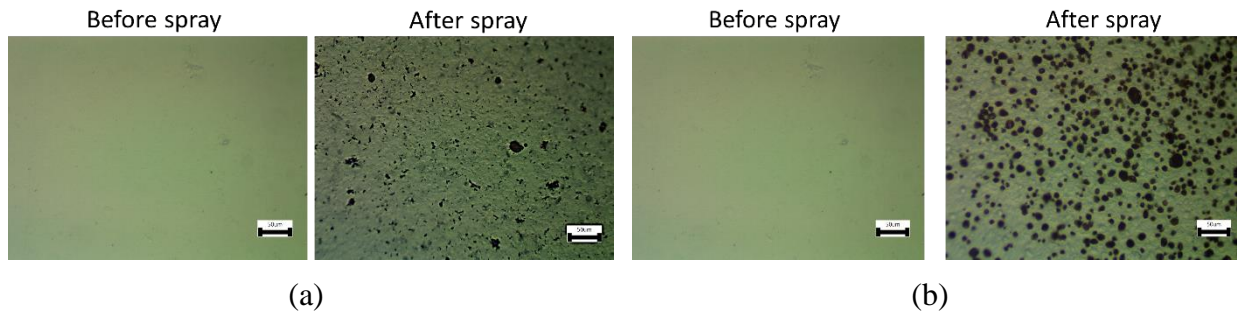


Figure 5-10 Experimental results show the sprayed powders at 300 m/s with (a) Al_2O_3 before and after (b) Cu before and after on the polyamide substrate (Scale bar is 50 μm in all figures)

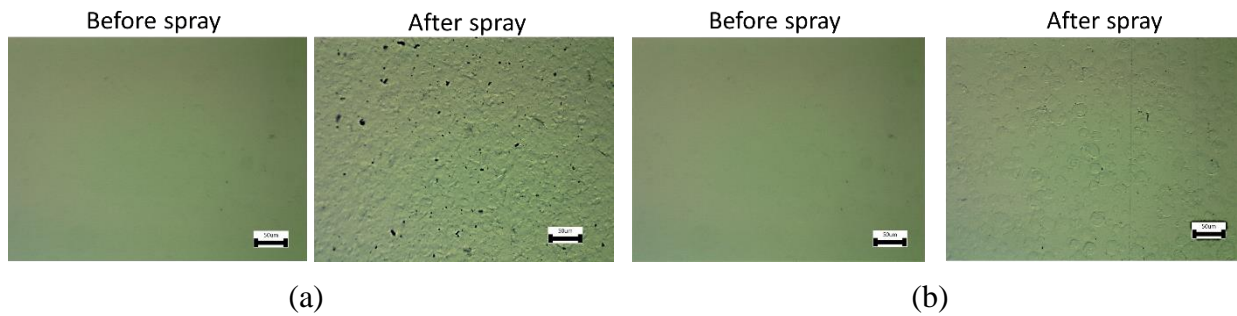


Figure 5-11 Experimental results show the sprayed powders at 200 m/s (a) Al_2O_3 before and after (b) Cu before and after on the polyamide substrate (Scale bar is 50 μm in all figures)

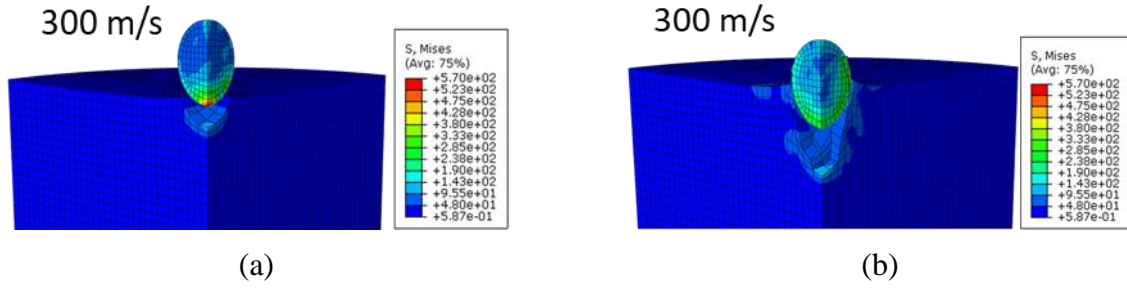


Figure 5-12 Simulation results show the particle at 300 m/s (a) Al_2O_3 (b) Cu

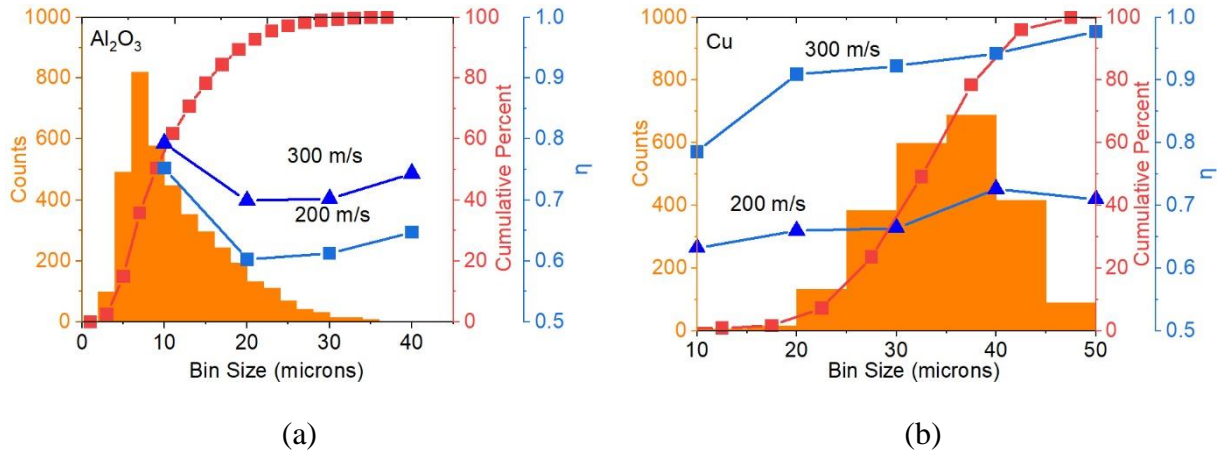


Figure 5-13 Particle at 300 m/s and 200 m/s with the response of the η , particle counts, and the cumulative particle distribution for (a) Al_2O_3 (b) Cu after impacting polyamide substrate

5.5 Conclusion

A three-network polymer model was used in this study to capture the plastic deformation of the substrate from the high-speed impact caused by cold sprayed Cu and Al_2O_3 . This model was calibrated with the already available polymer high-strain rates experiment results. The cold spraying process parameters entail a specific microstructure that influences the sprayed polymer substrate's mechanical properties. A two-disk (plate) rotary system was developed to easily measure the model's particle velocity, a needed parameter. The results show that an increase in particle kinetic energy increases the polymer viscoplastic deformation. As a result, the particles are less likely to rebound due to the decrease in strain energy and the gain of plastic deformation energy. The fraction of kinetic energy lost, η , above 0.9, shows good correspondence to the

experimentally observed adhesion of the particles and allows for the prediction of process windows for a variety of materials. The numerical results have been mapped into diagrams from the particle's kinetic energy responses lost after impacting and further validate the experiment results of cold spraying Al_2O_3 and Cu powders on the polyamide substrate. This study demonstrates a model that provides a way to minimize the trial and error processes for identifying successful cold spray deposition on polymer substrates.

6. THE MECHANICAL STRENGTH OF COLD SPRAYED SN ON A POLYMER SUBSTRATE

The content of this chapter is in preparation for submitting to a peer-review journal.

Coating fragmentation tests were conducted on a metalized polyamide substrate via cold spray to quantify interface and coating strength. An in-situ uniaxial tensile test equipped with four-point probe devices was used to test Sn films, between 23 – 120 μm thick, on a polyamide 6,6 substrate. The coated specimen's overall strength matched the uncoated bulk strength. Decreasing cold spray speed results in thicker layers but eventually erodes and fractures the layer. A modified Weibull model used the info of crack density, fragment length, and the measured specimens strength/strain to calculate the coated strength distribution at a fixed crack density and the mean strength as a function of fragment length. The results give an insight into local strength distribution and the coating strength distribution. The coating strength decreases as the coating thickness increases. The coatings between 74 μm – 120 μm show an interfacial shear strength between 25 – 53 MPa and an energy release rate between 15 – 32 J/m^2 . The interfacial shear strength of thinner coatings between 23 μm -37 μm reaches as high as 250 MPa but eventually saturate, and the energy release rate range between 43 – 45 J/m^2 . Results show that both interfacial shear strength and energy release rate increase as the coating thickness decreases. This suggested that cold spray process parameters needed to be carefully controlled in the future to have a robust coating system on polymeric materials.

6.1 Introduction

Cold spray coating of metals on polymers has wide-ranging applications from anti-biofilm to anti-biofouling, gas barrier coating for food packaging, and electrically conductive patterning for touch panels or consumer appliances. The success of these applications generally requires a well-adhered layer onto the substrate. Measurements of coating robustness can range from the ASTM D3359 adhesion by tape test to more quantitative measurements such as the ASTM D4541/ISO 4624 pull-off strength test. Similarly, the ASTM C633 is specifically designed for thermal or cold spray coating adhesion measurement. This limits the strength that can be assessed to that of the epoxy specified in the test (≈ 70 MPa), and there are other challenges due to the

roughness of the cold spray-coated layer (relative to the thickness of the coating). The pull-out force is applied evenly distributed onto the coated layer. Still, because the local stress depends on the geometry of the coated area, interfacial or coating failure is likely to happen at stress concentrations that make the resulting pull-off loads challenging to interpret if there are significant variations in layer thickness across a sample. In addition, these tests can be biased depending on how the specimens are prepared [16, 18, 23, 25, 118].

Other methods used for thinner films to measure adhesion and film properties rely upon observations of film cracking and subsequent crack delamination or buckles [119-121]. However, in thermal/cold spray coating, the indication of crack initiation, propagation, and crack density evolution for quantifying adhesion is complicated by the magnitude of difference between the film-substrate modulus and the potential non-uniform thickness of the coating. Experimental thermal spray systems have used digital image correlation to measure the coating strain and observed crack development [122]. The fracture strength can also be calculated [123], but further work is needed to explore bonding strength mechanisms.

A bulk metal typically used in a cold spray can be stretched and eventually ruptured by strain localization after a few percent elongations. However, when the metal is deposited onto a polymer substrate, the strain localization may be retarded. As a result, the coating may achieve higher fracture strains. The coated film may exhibit three types of behavior. The first is when the interfacial shear strength is low, and the film delaminates from the substrate after cracking. The second is that when the interfacial shear strength is an intermediate value, the film will form multiple cracks that increase density with additional strain. Finally, no debonding occurs at the interface when the interfacial shear strength is very high [124]. Thus, well-adhered metallic coatings can strain up to 10 % without any cracks and up to 30% with multiple cracks occurring, while poorly bonded coatings quickly form channel cracks at strains of $\approx 2\%$ [125]. This variance mechanism is because of metal film necking, film/substrate debonding, and grain boundary cracking. The significant disparity of low strain to high strain failure is caused by the two competing failure mechanisms: metal film necking and grain boundary cracking [126]. Crack growth starts to be unstable when the crack length is approximately 100-500 times the coating thickness. Also, the crack propagation becomes unstable when the relative electrical resistance increase reaches about 10% of the measurement [127].

Using computational models to describe the film failure process can help analyze the competing mechanisms of fracture and delamination. A two-dimensional analytic model was developed to predict the crack patterns in thin films [128]. A simulation model such as Abaqus uses the traction-separation law for modeling adhesion, which this simulation required to input six parameters. Simulations can capture the evolution of crack patterns and crack density on Cu-coated polyimide [119].

Tensile and fragmentation tests are not restricted to polymer-metal systems; similar tests have measured the crack density of SiO_x [129]. Studies have used the shear-lag analysis to calculate the interfacial shear strength and the adhesion energy for coated substrates [129-132]. Metal substrate-metal coatings also have used this general technique to measure the fracture of the interfacial shear strength, 2.57 GPa [133], of Cr coatings on steel.

A common way to calculate the interfacial shear strength is by using the Kelly-Tyson model [134] with the input of coating strength distribution using a two-parameter Weibull distribution. The fragmentation test provides the results of crack density during the in-situ tensile test. The crack images can be post-processed after the tensile test is done. The crack density can be correlated with the Weibull distribution to extrapolate the model's shape and size factor [134-139].

While conducting the in-situ fragmentation test measurements, the electrical resistance can also be measured using a four-point probe. A detailed explanation of the four-point setup and measurement technique during tensile testing of metal films on polymers can be found in [140]. The fracture strain of the coating can be identified when a deviation of electrical resistance is detected if the initial cracks are too small to observe optically, such as the case of CoFeB on Kapton, where cracking was determined with electrical resistance changes beyond applied strains of 1.6 % [141]. Similar in-situ mechanical and electrical tests have been conducted on ITO thin films, in this case showing the coating thickness dependence on saturated crack density [127]. The relative electrical resistance measurements can be separated into 3 distinctive zones [142].

In this current study, we have adapted the fragmentation methodology with a modified Weibull model to quantify the adhesion and strength of a cold-sprayed metal coating on a polymer substrate. A controlled coating process is set up in conjunction with an in-situ four-point probe tensile test to observe the crack formation. The system measures the specimen strain, records the load and electrical resistance. The variation of coating thickness was examined under tensile

loading conditions to identify the adhesion. The interfacial shear strength was calculated via the Kelly-Tyson approach [134], while the energy release rate was determined via Beuth [143] method.

6.2 Experimental procedures

The raw materials for this study consist of a polyamide 6,6 sheet (acquired from ePlastics[®]) with 305 x 305 x 0.813 mm that was laser cut (Speedy400 Flexx, Trotex Laser machines) into multiple dog bone shape specimens (ASTM D638) for mechanical tensile testing. In addition, Sn powder for cold spray coating (CenterLine LTD), shown in Figure 6-1, was documented using Scanning Electronic Microscopy (SEM, FEI Corp., Quanta 650 FEG, USA) for powder morphology. The particle size distribution was measured and found to be in the range of 5-45 μm (Malvern, Morphologi G3).

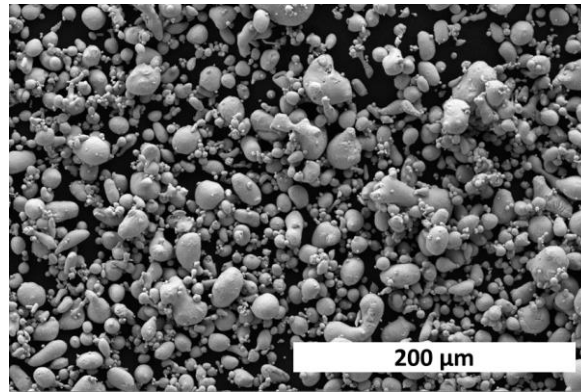


Figure 6-1 SEM image of the starting Sn powder morphology used in this study

A low-pressure cold spray device (K205/407R) by Rus Sonic Technology, Inc was operated in this research. The powder feed rate is approximately 0.3-0.4 g/s with a static inlet pressure of 0.55 MPa. A cold spray nozzle is stationed on a Kuka robot arm (KR 6 R700 Sixx, KUKU Robotics) and programmed to spray with a fixed 10 mm distance to the specimens. Four spray speeds: 0.01 m/s, 0.05 m/s, 0.1 m/s, and 0.15 m/s were sprayed on tensile polyamide 6,6 coupon with a single straight path. The coating region ends before the grip zone. Figure 6-2 (a) shows the specimens after cold spray Sn coating on polyamide 6,6 (used 0.15 m/s as an example). Figure 6-2 (b) shows the speckle pattern applied to the specimens from top to bottom specimen

0.01 m/s to 0.1 m/s (spray techniques and procedures can take references in Correlated Solutions Vic-3D 8 testing guide). Figure 6-2 (c) shows the specimens after the tensile test from top to bottom specimen 0.01 m/s to 0.1 m/s. The polymer specimens tend to recover after release from the testing grip stage. Thus it is important to measure the strain and the coated crack of the specimen before its unloaded.

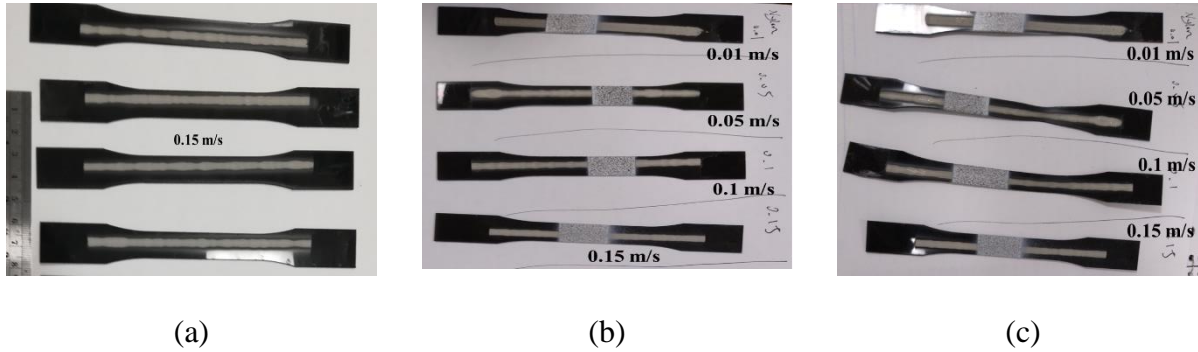


Figure 6-2 Polyamide 6,6 tensile dog-bone specimens (a) after cold spray Sn (b) sprayed speckle pattern (c) after tensile test

Figure 6-3 shows a cartoon drawing of the in-situ electrical-mechanical tensile test device constructed for this work. Two optical microscopes (7-inch digital microscope, Sunlea Tech) were set up in this system. In addition, a digital force gauge (BAOSHISHAN) is installed on one side of the grip. The load cell can reach a maximum of 1000 N. A stepper motor with a gearbox ratio of 47:1 (2.8 A, Stepperonline) was installed on the other end side of the grip. A CNC Digital Stepper Driver (24 V, DM556 2-phase stepper Motor Driver) and a power supply universal regulated switching transformer adapter (5V, 120 W, ALITOVE) were connected to the stepper motor. The device needs to produce a consistent torque while conducting tensile testing. Therefore, a simple Arduino code was written to control the motor for allowing the tensile rate to be fixed at 10 mm/min (displacement control).

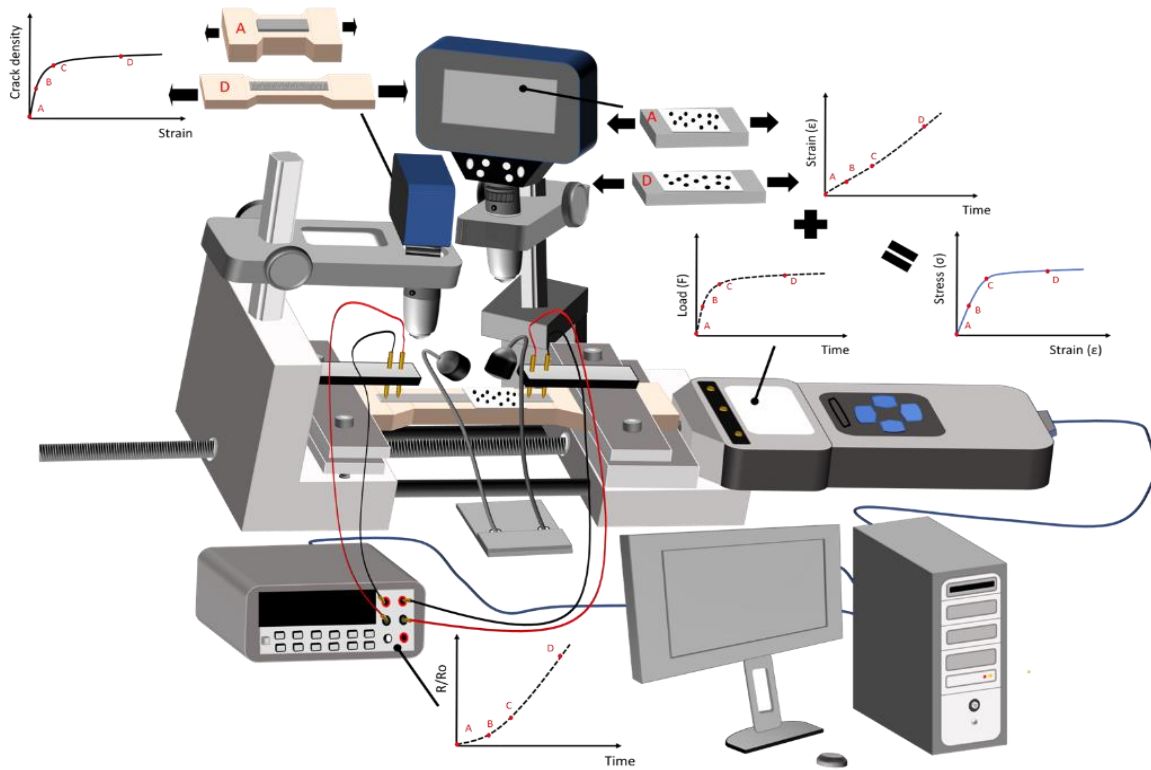


Figure 6-3 A schematic cartoon drawing of an in-situ electrical-mechanical tensile test device

A region of interest on the specimen is marked before spraying speckle patterns. The speckle patterns cover the coated region and the uncoated region. The location should be where the digital microscope camera can track the spray pattern changes. Video of both speckle patterns and the crack patterns are recorded. The saved coating microstructure video documents are later post-processed in Shortcut (image processing software) and output as continuous tiff images (10 images/second). The same is done for the sprayed speckle pattern video, which loads into the Shotcut software and outputs continuous tiff images. The tiff images are later input into the Digital Images Correlation Engineering (open-source software developed by Sandia National Laboratory). An unstrained speckle image is set as a reference, and then the region of interest is chosen to track the remaining speckle images. The analysis model was set to be a subset-based full-field mode. The SSSIG threshold is 68, subset size 43 pixels, step size 56 pixels, and the gauss filter at 9 pixels. The shape functions are chosen to have translation and normal stretch and compute strain results (threshold number many need to be adjusted according to the speckle pattern size-see details in the DICE manual [144]). The analytical solution of the strain results is then loaded into Paraview

5.0 for post-processing. Finally, the average strain results with time increments are output with an excel file.

Figure 6-4 shows the example of the crack density captured in a microstructure image at a strain of 0.24 (specimen spray speed 0.05 m/s). A series of integer frame images of the microstructure were taken from the output Shortcut software; each frame is correlated with the engineering strain. The crack density is obtained from the intersection of a fixed amount of distances that intersects cracks in each microscope image. Five parallel lines were drawn on each microscope image; these lines are parallel to the loading direction. The fragment length measures the crack to crack distances in the parallel line drawn in the microscope images. The measuring results of the crack density and the fragment length from the five parallel lines were averaged, including the standard deviation. The crack density trend should be the inverse of the fragment length.

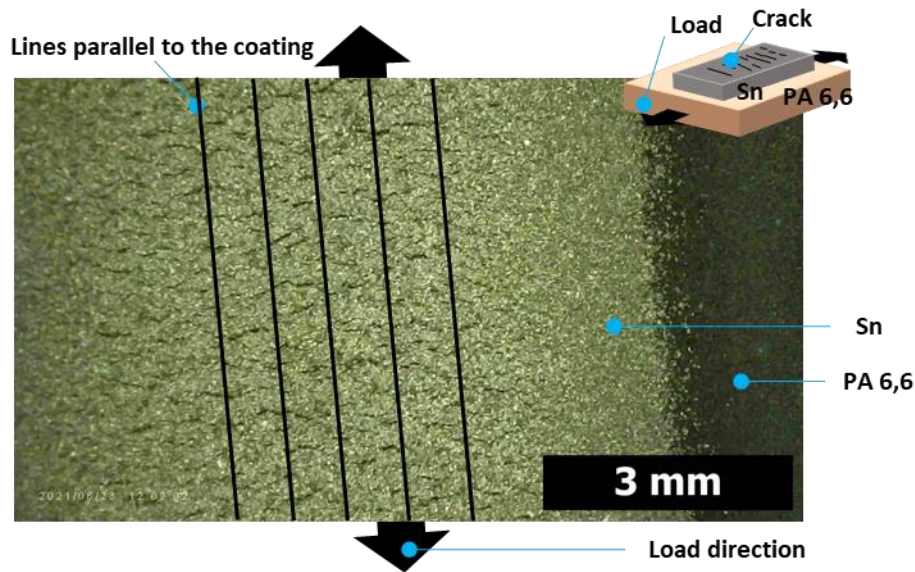


Figure 6-4 The microscopy image of the Sn coated on polyamide 6,6 substrate at strain 0.24

The four-point probe is fixed on the mechanical testing device stage and allows the probe to contact the coated area. The probe is connected to an Agilent 34401a; the probe is fixed at both sides of the grip section of the specimen; this design is to avoid the probe sliding from the coated area while conducting the tensile test. Keysight Connection Expert 2021 was used to detect instruments connected to the PC and configure the interface automatically. Finally, an Agilent

Digital Multimeter Connectivity Utility was used for data acquisition. The measured electrical resistance from the four-point probe is recorded with time.

The 3D optical profilometer (Zygo, NewView 8000) measured the film thickness and topography of the four different sprayed speeds. The surface profilometer was scanned in a 6 mm x 6mm area at a resolution of 5.91 μm . According to ASME (B46.1 2D) standards, an R_t value of 10 line scans across the coated cross-section was considered for determining the coating thickness.

6.3 Results and discussion

Figure 6-5 shows the tensile strength of polyamide 6,6 and the coated specimens at four different spray speeds. The elastic modulus of the three bulk polyamide 6,6 specimens have an average of 2000 MPa, with the yield stress of 21 MPa, and the yield strain 0.02 (applied strain). Spray-coated specimens are mechanically tested to ensure the tested results are reproducible and reliable. Few specimens coating span towards the grip region to observe the coating strength differences between those specimens that are only coated in the neck region (coating region refer to Figure 6-2). The results show that the coating strength shows mostly indifference. The results suggested that because the metal and polymer interface is highly contour, the coating stress is concentrated depending on thickness, voids, compactness, defects, etc. (The interface can be found in Figure 6-7).

The results suggested that the continuous impact of the relatively thin cold spray coating does not influence the overall polymer mechanical performances (the coating did not significantly strengthen the polymer, nor did the damage from the implanting of powder into the polymer degrade the observed strength). Coated and uncoated specimens show yield strain at around 0.02, followed by a plastic strain—the mechanical properties of the coated and the uncoated substrate mechanical strength remains the same. Therefore the structural integrity of the coated structure has not been compromised.

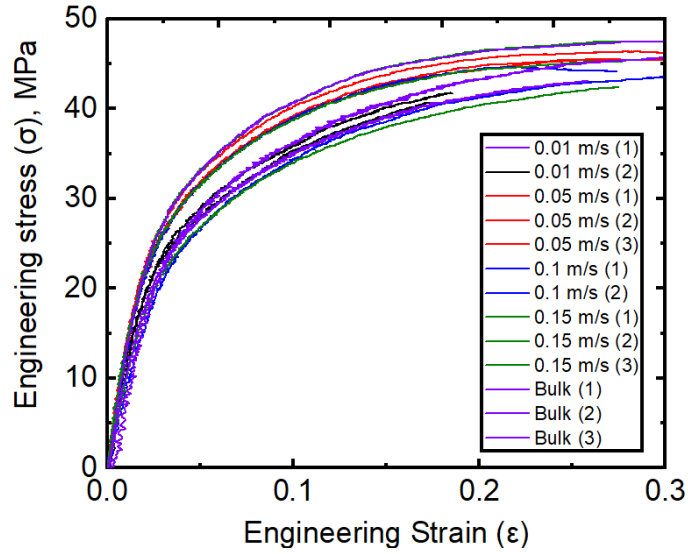
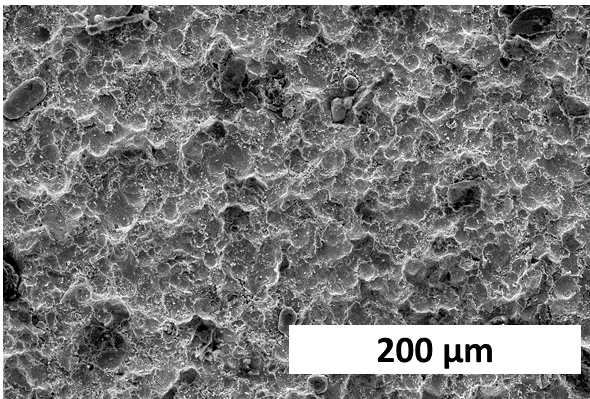
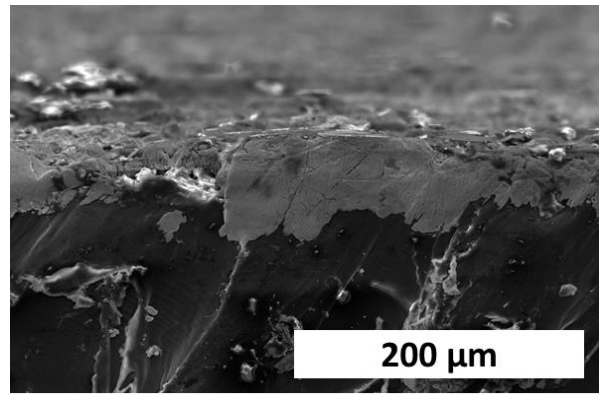


Figure 6-5 Stress-strain results of bulk substrate and the coated substrate with the spray speed at 0.01 m/s, 0.05 m/s, 0.1 m/s, 0.15 m/s (color online)

Figure 6-6 shows the SEM images of Sn coated on the polyamide 6,6 substrate at the (a) surface and (b) cross-section. The coated surfaces show crater morphology; this is a result of particles continuously bombarding. In addition, the interface connection between the coating and the substrate reveals a wavy interface; these results demonstrate that the metal mechanically interlocks into the polymer substrate.



(a)



(b)

Figure 6-6 Sn coating on polyamide 6,6 substrate (a) Surface (b) cross-section of the specimen

Figure 6-7 shows the coated specimens' optical images and the surface profile results from the profilometer with the four different cold spray speeds. A vertical line was drawn on the four specimens of the surface profile to report the surface roughness and thickness. The measurements are organized at the bottom of Figure 6-7. The coating thickness is between 2 to 15% of the total polymer thickness, but both s Figure 6-6 and Figure 6-7 shows significant point-to-point variations in the thickness for each coating. The decrease of spray speed increases the average coating thickness from 23.12 μm to 120.2 μm ; however, the profilometer results show that the coating layer starts to crack or has significant topography with the decreasing speed after reaching 0.01 m/s. In addition, it shows that the coating was partly destroyed or eroded at the surface layer. A high roughness compares with the coating for spray speed 0.05 m/s. At spray speed 0.15 m/s, the coated layer is relatively thin and evenly; at spray speed at 0.1 m/s, the coated layer gets rough; at 0.05 m/s, the coating thickness increases. This suggests that a spraying speed of around 0.05 m/s is best for coating with a single continuous path without causing coating fracture.

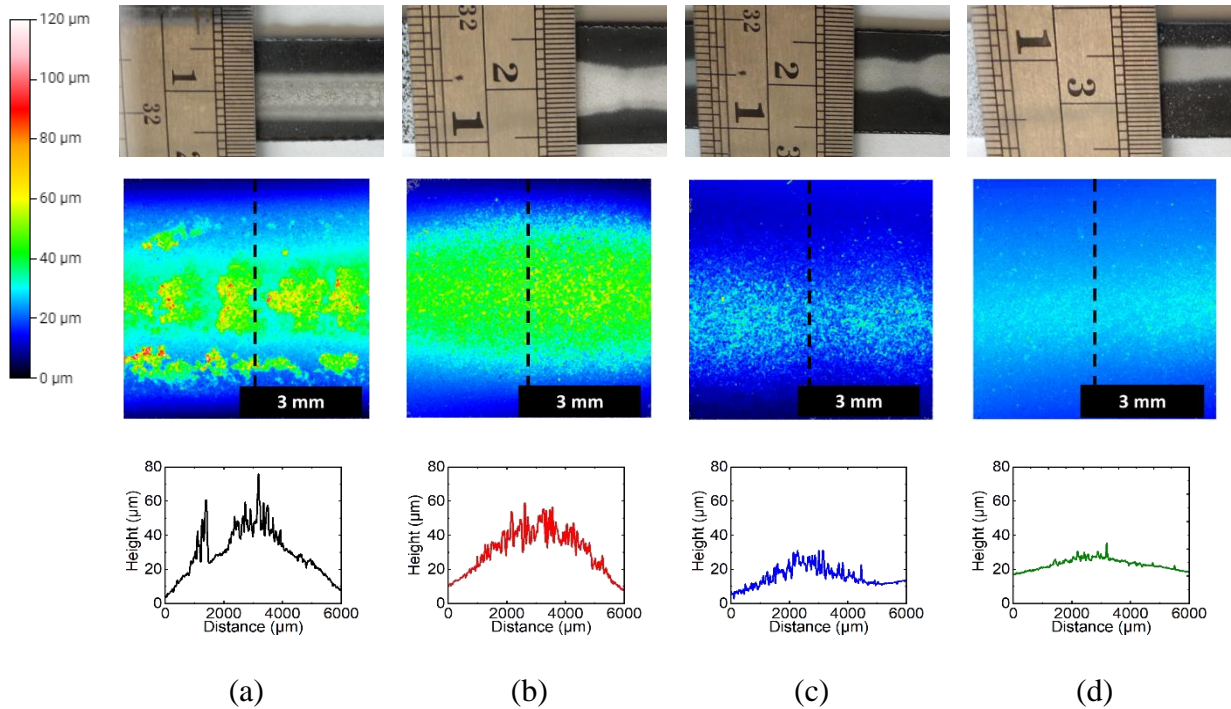


Figure 6-7 Coated specimens optical images, the surface profile, and the surface roughness/thickness (a) 0.01 m/s (b) 0.05 m/s (c) 0.1 m/s (d) 0.15 m/s

Figure 6-8 shows the four coated specimens in terms of crack density, and fragment length plotted as a function of engineering strain. Each of the reported results in Figure 6-8 is chosen from an optical microscope images frame 100, 200, and continues to 1300 (post-processing procedures referred to Figure 6-4). Low crack density means a high fragment length and vice versa. At the beginning of the measurements, a high standard deviation of fragment length is typically accompanied by a minor standard deviation of crack density. Results on the profilometer in Figure 6-7 show that the cross-section of the coating is a dome-shaped structure which results in the ununiform thickness. This would suggest that the crack density and the fragment length would differ depending on where the parallel line is drawn on the microscope image. With the increase of engineering strain, the crack density starts to have a high standard deviation, but for the fragment length, the standard deviation decreases; more cracking occurs, and the fragment length is consistent with increasing strain.

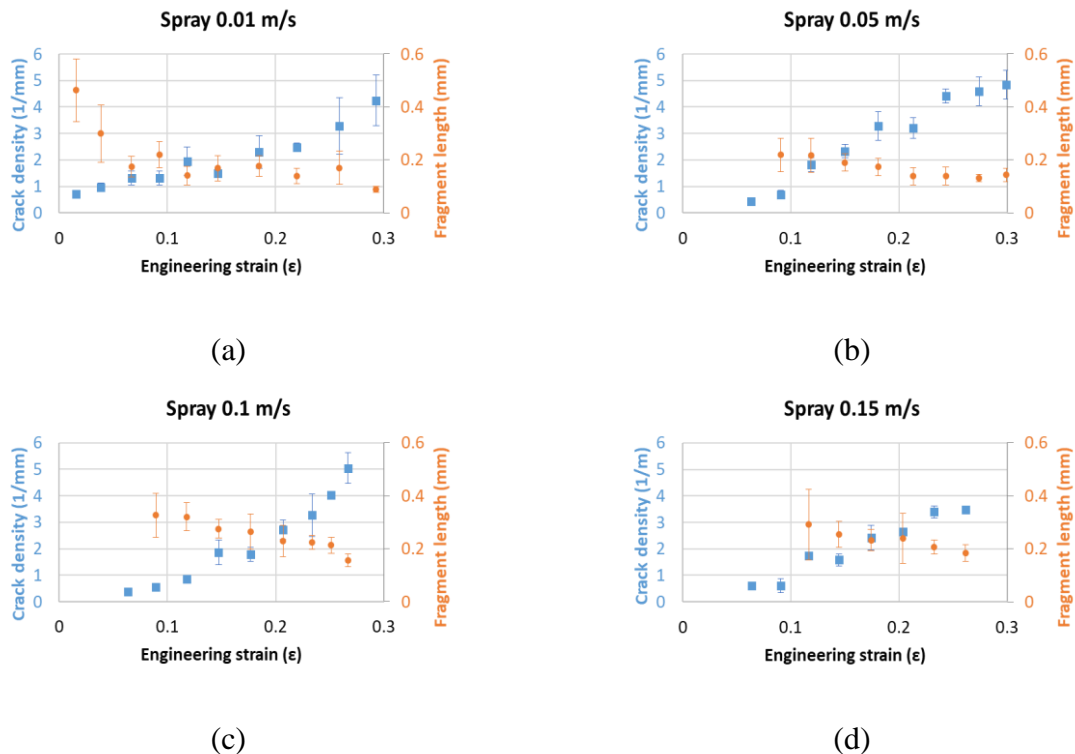


Figure 6-8 Crack density and the fragment length as a function of engineering strain at spray speed (a) 0.01 m/s (b) 0.05 m/s (c) 0.1 m/s (d) 0.15 m/s

A thinner coated layer limits the digital optical microscope to capture the crack locations due to the image resolution and the roughness of the surface coating. In addition, increasing the cold spray coating speed will result in a thinner coating layer on the substrate; as a result, the crack density and fragment length data points will be harder to track during initial measurements. However, eventually, a saturating curve of crack density and the fragment length are observed at any spray speed when increasing engineering strains.

The coating stress is calculated from the mechanical stress equilibrium (shown in equation (15)), which considers the modulus ratio, Poisson ratio, the substrate's thickness, and the coated layer's thickness. We choose to examine stress in the film, rather than the strain, for use in applying the Weibull model described below. In addition, because the coated layer is not evenly distributed on the top surface substrate (a dome shape structure is formed on the substrate rather than a biaxially uniform coating), this model should only be a first order estimate of the stress in the film. Also, it is assumed that limited plastic deformation occurs on the cold spray coating before a fracture occurs. As such, the model will become less accurate as the plastic strain increases. With the above two factors, the model provides an upper bound (likely overestimated) stress in the coating [145].

$$\sigma_c = \frac{\sigma E_c H}{(E_c h_c + \left(\frac{1 - V_c^2}{1 - V_s^2} \right) * (E_s h_s))} \quad (15)$$

σ_c is the coating stress, σ is the applied stress on the specimen, E_c coated elastic modulus, V_c coated Poisson ratio, h_c coated thickness, E_s substrate elastic modulus, V_s substrate poisson ratio, h_s substrate thickness, H is the total thickness.

The measured applied stress on the specimens are in Figure 6-5, and the average thickness of the coating can be found in Figure 6-7. The polyamide 6,6 modulus is 3 Gpa; Sn modulus is 40 Gpa, substrate thickness 0.819 mm. One challenge with these data is that we have variations in the microstructure and expect variations in the material's properties (coated and substrate due to damage in the coating process). Therefore, Curtin modified the Weibull model to address material systems that fail with two different flaw distributions; in [146], Curtin developed the (Weibull of Weibull, or called the WoW model) to analyze a batch of fiber strength distribution shown in

equation (16). The classical Weibull distribution might not be the best candidate for many reasons, such as fibers diameter variation, material properties changes from fiber to fiber, and defects fluctuation from fiber to fiber, thus resulting in Weibull strength distribution with different scales parameters for each. Therefore, Curtin proposed the modified Weibull distribution that considers the strength distribution of a batch of fiber and size distributions. For our current cold sprayed Sn layer system on polyamide 6,6, this research has adapted Curtin's modified Weibull model [32] in equation (16) to determine the cold spray coating strength distribution. The coating layer thickness is analogous to the fiber. The modified Weibull model (WoW model) can be summarized as follows (16):

$$P(\sigma) = \sum_{i=1}^{\infty} P_i(\sigma)P(b_i) \quad (16)$$

where $P_i(\sigma)$ is the strength distribution of a coated specimens at a coating thickness and $P(b_i)$ probability of randomly chosen specimens.

The strength distribution of a chosen coated specimen can be expressed by (17):

$$P(\sigma) = 1 - \exp\left[-\frac{\iota}{\iota_0} \left(\frac{\sigma}{b}\right)^a\right] \quad (17)$$

where a value is the strength distribution of an individual crack density at a fixed coating thickness which the parameter a is the slope (shape parameter), b_i is the scale parameter, ι is the coating fragment length, and ι_0 is the reference coating length.

However, any coated specimens (i) may have a distribution of crack density, which can therefore be expressed as in equation (18):

$$n_i(\sigma) = \frac{1}{\iota_0} \left(\frac{\sigma}{b_i}\right)^a \quad (18)$$

The parameter a should be a constant fixed value regardless of random coating length in each set of coated specimens. Therefore, equation (18) can be organized as $\log n(l_0) = a \log \sigma - a \log b$. Figure 6-9 (a) shows the results of all four cold spray coatings (different cold spray speeds) plotted with the crack density as a function of coated stress to obtain a value from the slope. Equation (19) is the scale parameter distribution among coated specimens in a batch.

$$P(b) = 1 - \exp \left[- \left(\frac{b}{B} \right)^m \right] \quad (19)$$

where b and the m value are from the strength distribution among the crack density at a fixed coating thickness, B is the scale parameter.

Therefore, equation (19) can be redistributed as $\ln(-\ln(1-P)) = m \ln b - m \ln B$. Figure 6-9 (b) shows the results of extrapolating the B and m values for the four coated specimens. The slope for spray speed 0.1 m/s and 0.15 m/s are particularly close. This suggested that the average coating strength would be close. However, the local coated strength's level may vary.

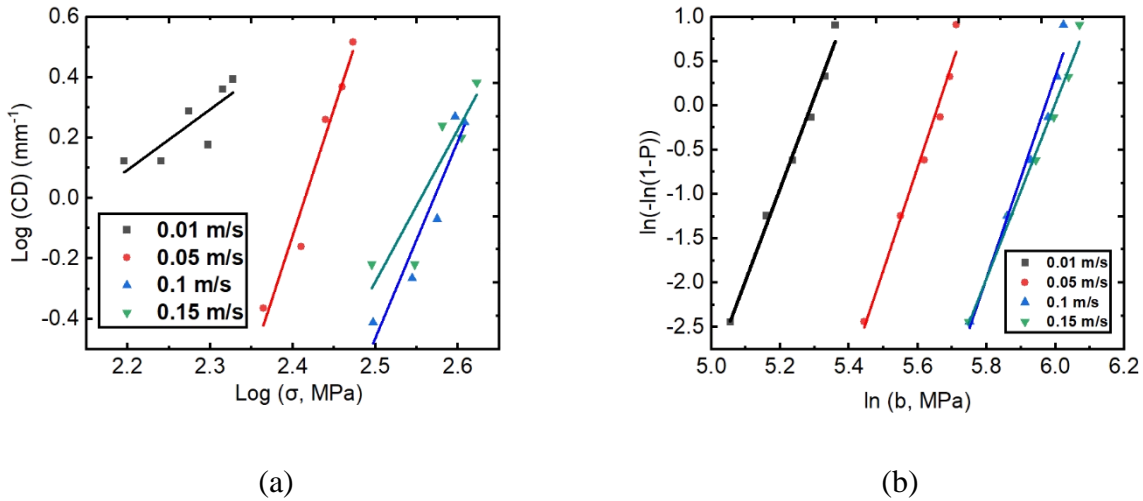


Figure 6-9 The modified Weibull distribution curve

$$\gamma = \frac{m}{\sqrt{m^2 + a^2}} \quad (20)$$

$$\alpha = \frac{ma}{\sqrt{m^2 + a^2}} \quad (21)$$

$$\beta = (1 - (m^2 + a^2)^{-0.75})B \quad (22)$$

here α is the apparent Weibull modulus, γ is the scaling strength factor, and the β is the correction factor.

Once the a , m , B are determined, the adjustment formula in equations (20), (21), and (22) can then be calculated for the strength distribution of the coated specimens. Equations (20), (21), and (22) are derived from an analytic model based on the Global Load sharing approximation; details can be found in [146]. The calculated constants are organized in Table 15. The report values are reasonable compared to Sn strength measurements.

Table 15 The modified Weibull model constants

Spray speed (m/s)	Coating thickness (μm)	a	B (MPa)	m	α	β (MPa)	γ
0.01	120.2	2	198.45	10.35	1.97	192.65	0.92
0.05	74.73	8.4	287.05	11.65	6.81	281.77	0.81
0.1	36.51	6.5	391.84	11.39	5.66	383.6	0.87
0.15	23.12	5	402.47	9.87	4.49	391.57	0.89

The expression in equation (16) can be represented shown in equation (23) which is the cumulative density function (CDF) of strength distribution at a fixed crack density (fragment length).

$$P(\sigma) = 1 - \exp \left[- \left(\frac{l}{l_0} \right)^\gamma \left(\frac{\sigma}{b} \right)^a \right] \quad (23)$$

Equation (24) is now the modified Weibull modulus of the mean strength as a function of the fragment length

$$\sigma_m = \beta \left(\frac{l}{l_0} \right)^{\frac{-\gamma}{\alpha}} \cdot \Gamma \left(1 + \frac{1}{\alpha} \right) \quad (24)$$

where Γ is the gamma function, the l is the coating fragment length, and l_0 is the reference coating length.

Figure 6-10 (a) shows an example of the coated strength distribution with the spray speed at 0.05 m/s. The results show the decrease of fragment length from 2 mm to 0.32 mm—the distributed coated strength reflected upon the nature of the cold spray coating. It is recognizable in Figure 6-6 that the coated layer and the interface are highly contoured. The measured fragment length provided a holistic view of the local coated strength measurements during the tensile test. The cracks occurred as the fragment length decreased and resulted in the increases of the coated strength.

The four coating's mean strength from the modified Weibull is plotted in Figure 6-10 (b) as a function of fragment length. Commonly bulk Sn has an ultimate strength of around 220 MPa. The Weibull plots and the calculated Sn coated strength shows results ranging from 145 MPa to 450 MPa. These results are reasonable since Sn coatings are a continuous impact resulting in the material being strain harden.

The results of mean strength from the modified Weibull model from equation (24) show a good agreement with the calculated coating stress from equation (15). As the fragment length decreases, more cracks occur, and higher coating stress is needed to develop the cracks. The results show that thinner coating requires more forces to fracture at a fixed fragment length. The results agree well with [147]. The fragmentation technique equipped with the modified Weibull model used the crack density to determine the coated strength distribution.

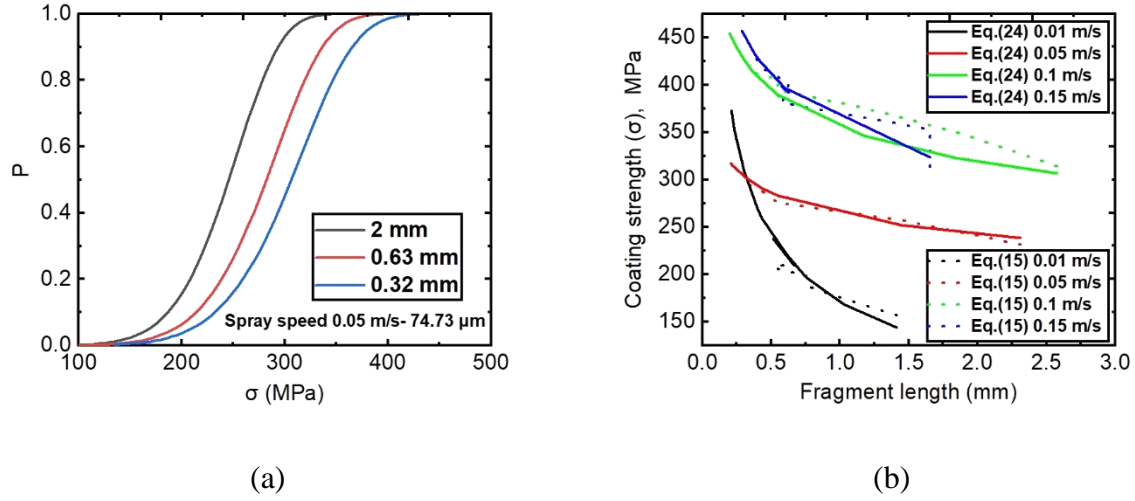


Figure 6-10 (a) Spray speed at 0.05 m/s with the decrease of fragment length plotted with the coated strength distribution (b) All four coated specimens coated mean strength distribution with increasing fragment length

The measured crack density and the fragment length saturate once the coating reaches a maximum load (shown in Figure 6-8). Figure 6-11 (a) shows the coating strength plotted with the function of the coating thickness. The average coating strength is taken from the modified Weibull strength distribution when the crack density/fragment length is saturated in Figure 6-10 (b). The coating strength depends on the thickness (size effect phenomenon, assuming defects usually are distributed in the coated layer and the increase of layer thickness will obtain more defects and voids); as the coating thickness increases, the coating strength decreases.

Equation (25) was used for determining fiber and matrix interface strength in composite materials [134]. However, researchers have demonstrated that it can also be used in calculating the interfacial shear strength of the coating [147, 148]. Therefore, the interfacial shear stress from the Kelly-Tyson model is calculated with all four different coating thicknesses.

$$\tau = 1.34h \frac{\sigma_m(l_c)}{\bar{l}_{sat}} \quad (25)$$

h is the coating thickness, \bar{l}_{sat} average fragment length at saturation (the values are obtained from Figure 6-8), $\sigma_m(l_c)$ is the mean coating strength at fragment saturate (the mean coating strength values can be obtained from equation (24) and cross-correlate with Figure 6-8).

Figure 6-11(b) shows the interfacial shear stress plotted as a function of applied engineering strain. The interfacial shear stress increases with decreasing coating thickness. At spray speed 0.01 m/s and 0.05 m/s, the interfacial shear stress value is relatively lower than 0.1 and 0.15 m/s. The interfacial shear strength value should be constant according to equation (25) when the crack saturates (engineering strain reaches 0.1 is when crack saturates shown in Figure 6-8, thus the interfacial shear strength between 25 – 53 MPa for the two spray speed 0.01 m/s and 0.05 m/s). The substrate shear stress is 23 MPa (from Von Mises relationships, $\tau = \frac{\sigma}{\sqrt{3}}$); this calculation gives an idea of a reasonable range of interfacial shear stress. The results show that the interfacial shear stress agrees well with the substrate shear stress when the spray speed is at 0.01 m/s and 0.05 m/s. The spray speed for 0.1 m/s and 0.15 m/s shows a significantly higher interfacial shear stress at a given applied strain (the interfacial shear strength reaches as high as 250 MPa for the two spray speeds 0.1 m/s and 0.15 m/s); this needs to account for the thinner coating thickness. The fragment length affects the output of the interfacial shear strength. The formula considers when the substrate is infinite while the coating is thin—a thinner coating resulting in higher interfacial shear stress for propagating cracks.

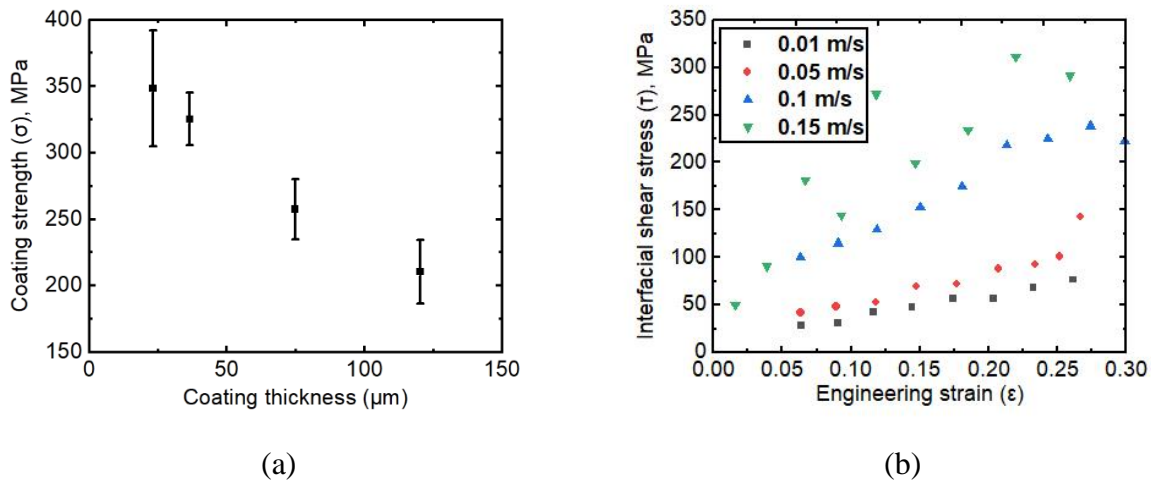


Figure 6-11 Four different thickness specimens (a) Coating strength vs. the coating thickness
(b) The interfacial shear strength value with the engineering strain

The electrical resistance was measured via the four-point probe setup integrated with the in-situ mechanical testing system—the relative resistance obtained from electrical resistance

measurement was normalized from the beginning. The relative electrical resistance is plotted with the function of engineering strain shown in Figure 6-12— from the specimen with a spraying speed of 0.01-0.15 m/s. Results show that the relative electrical resistance exponentially increases when the strain increases. It was suggested that a 10% relative electrical resistance could set a criterial for the first crack threshold [127, 149]. Thus, in the results, the corresponding first crack strain is organized in Table 16. The strain results are correlated with the coated bulk stress in Figure 6-5 and equation (15) to calculate the coating stress. The strain results do not show any dependence as the thickness increases. However, the coating stress does increase as the coating thickness increases. These results agree well with [147]. This suggests that the thinner coating requires more stress to initial crack failure at the same strain level compared to thicker coating.

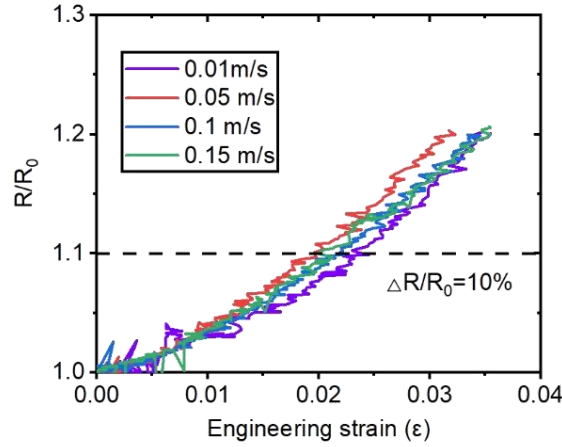


Figure 6-12 Relative electrical resistance as a function of engineering strain

For the four different thicknesses of coating specimens, the first crack strain results detected by the four-point probe are organized in Table 16. The results of the relative electrical resistance show that with thicker coating, higher strain is required to initiate the first crack. The critical energy release rate (G_c) in (26) was derived from a mode I steady-state analysis through-thickness channeling crack onset in a high-modulus coating on a low-modulus substrate [143, 150].

$$G_c = \frac{\sigma_c^2 \pi h_c}{2E_c} \cdot g(\alpha, \beta) \quad (26)$$

where σ_c is the coating stress when the first crack occurs, h_c is the coating thickness, E_c is the Sn elastic modulus, and $g(\alpha, \beta)$ is a dimensionless function-dependent only on Dundurs parameters. The four specimens of Dundur constants are in [150]. The coating stress (σ_c) value is obtained from equation (15).

Table 16 shows the calculated energy release rate for the four different coatings thickness. The results show that as the coating thickness decreases, the energy release rate increases proportionally. The cold spray coating is formulated with particles continuously bombarded; the decrease of spray speed means more particle impact. Therefore, it would achieve a thicker coated layer, and thus less applied stress is needed to fracture the coated specimen. Figure 6-12 shows that spray speed 0.15 m/s has the lowest relative electrical resistance at a fixed strain. The results agree well with the trend in Figure 6-11 (b), which shows that decreasing coating thickness increases the interfacial shear strength, and similar results can be found in [141, 147, 151, 152]. Thus, this research shows that metalized polymer substrate under different cold spray speeds does impact the mechanical coating strength.

Table 16 The adhesion energy from the four different coating thickness

Spray speed (m/s)	Coating thickness (μm)	First crack strain (ϵ)	Coating stress at the first crack $\sigma_c(\text{MPa})$	$g(\alpha, \beta)$	Energy release rate (J/m^2)
0.01	120.2	0.0236	107.83	0.3	14.6
0.05	74.73	0.0196	142.32	0.6	31.7
0.1	36.51	0.0219	204.14	0.8	42.5
0.15	23.12	0.0199	207.13	1.3	45

6.4 Conclusion

Metalized cold sprayed polymer substrates are becoming an alternative solution for food storage application, barrier coating, and stretchable, wearable, and flexible electronic devices. The adhesion performances between the metal-coated layer and the polymer substrate influence the coated surface's crack propagation. The coated layer is mechanically interlocked into the polymer substrate, which is the primary factor of the bonding mechanism. This research has used fragmentation techniques with a modified Weibull model for determining the coating strength distribution. The input of crack evolution provided the coating strength distribution. The increased

coating thickness shows the decrease of coating strength proportionally. Kelly-Tyson model was used to determine the interfacial shear strength with the input of the coated strength distribution. The interfacial shear stress value is around 25-53 MPa for thicker coating (74-120 μm), and the measured value increase as the coating layer decreases. The energy release rate for coating between 74-120 μm shows 15-32 J/m^2 and increases as the coating layer decreases. This suggests that a controlled cold spray process is vital for enhancing the coating's mechanical strength robustness on a polymeric substrate. The results and the build-up device demonstrate cost-effective, time-efficient, and accurate measurements for understanding the mechanical behavior of the cold spray metal-coated polymer substrate.

7. ELECTRICALLY CONDUCTIVE METALIZED POLYMERS BY COLD SPRAY AND CO-ELECTROLESS DEPOSITION

The content of this chapter was published in the ASME 2020 15th International Manufacturing Science and Engineering Conference and resubmitted to the ASME Open Journal of Engineering (under review).

Conducting polymers are of particular interest in sustainable electronics. Despite great promises, current approaches have significant limitations to producing conductive polymers in a sustainable, large-scale, and high-throughput manner. This study hybridized cold spray particle deposition technology with a co-electroless deposition process to achieve electrically conductive metallization on polymer surfaces. The resulting conducting polymer retains its intrinsic mechanical strength while providing multifunctional engineering performances. Numerical modeling and a series of characterizations are conducted to investigate both the cold spraying process and the performance of resultant conducting polymers. Numerical simulations on high-velocity particle impact provide information for optimum cold spraying process parameters. The microstructure of as-sprayed and co-plated samples are thoroughly examined by scanning electronic microscopy. Cyclic voltammetry results reveal that the metalized polymers are stable after multiple cycles. The results are high-electrically conductive and stable electrodes. The resultant conducting polymers have the potential for sustainable polymer electronics.

7.1 Introduction

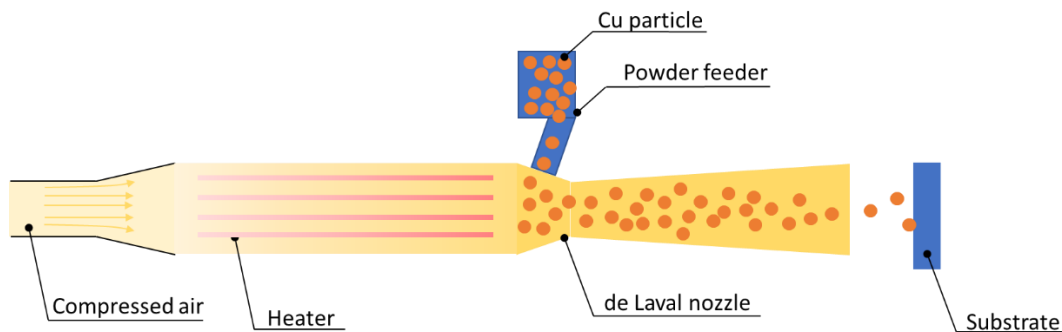
Conducting polymers attract widespread interest in sustainable electronics applications owing to intrinsic advantages of polymers, including high-impact resistance, light-weight, dimensional stability, and low cost. Current approaches to producing conducting polymers involve chemical vapor deposition, physical vapor deposition, screen-printing, ink-jet printing, and electroless deposition [52, 53, 153-155]. Despite great promises, these methods have significant limitations in the fabrication of conducting polymers in a large-scale, high-throughput, flexible, eco-friendly, and facile manner.

Cold spray particle deposition has been successfully used in the metallization of various polymers within the last decade, and promising results have been obtained [20, 27, 53]. In the cold spray deposition process, as shown in Figure 7-1 (a), microscale (10-60 μm) metal particles are

accelerated to supersonic velocities using a converging-diverging nozzle and impact a target surface. During the impact/impingement of the particles, the kinetic energy of particles dissipates over the substrate surface, which results in a high-bond strength metal coating due to the adiabatic shear instabilities. However, although cold spray particle deposition is a promising technology to achieve high-bond strength metallic coatings on polymer surfaces, the resulting coatings generally suffer from poor electrical conductivity. Herein, erosion of the polymer surface due to the continuous high-speed particles impact is mainly responsible for the low-electrical conductivity [1]. Although some researchers have attempted to solve this issue by adjusting spray parameters for each spray pass, it remains challenging due to the possible damage to polymers' structural integrity [18, 20, 31].

This research recently showed a proof-of-the-concept for electrically conductive metallization on ABS polymers by integrating the cold spraying with a subsequent electroless deposition [156]. This concept used the as-cold sprayed layer on the polymer surface as the catalyst (i.e., seed material) for the co-electroless deposition (co-ED) process. The proposed approach achieved high-electrically conductive patterns on the insulator polymer surface by replacing traditional chemical processes [154] [157, 158]. In our previous study, however, the cold spray deposition mechanism and the effect of cold spray operational parameters on polymer metallization were not elucidated. Nevertheless, these are integral to expanding conducting polymers in a wide range of sustainable electronics applications.

In the present study, we attempt to fill this gap by systematically studying; (1) high-velocity cold spray particle impact by numerical modeling, (2) microstructure, (3) adhesion performance, (4) electrical conductivity, and (4) mechanical strength of the resultant metallic coatings. In addition, this study aims to uncover the process-structure properties of the described hybrid manufacturing approach (i.e., cold spray coupled with co-electroless deposition) for rapid and scalable production of conducting polymers.



(a)



(b)

Figure 7-1 (a) Schematic of a typical cold spray process, (b) experimental setup

7.2 Materials and methods

7.2.1 Materials

Microscale copper (Cu) particles were used as the cold spraying feedstock material. The particles have quasi-spherical morphology having a size range of 1-10 μm (see Figure 7-2). Polyamide (i.e., Nylon 6) was employed as the polymer substrate. The co-electroless deposition (co-ED) process chemicals were purchased from Sigma-Aldrich and used without further purification.

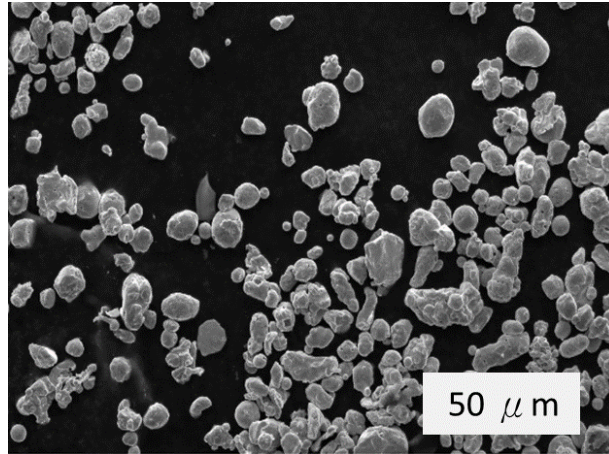


Figure 7-2 Morphology of copper (Cu) particles

7.2.2 Cold spray particle deposition

A low-pressure cold spray machine (Rusonic Inc.) was used in the particle deposition experiments. The cold spray nozzle was mounted on a 6-axis robot arm to control the coating process (See Figure 7-1 (b)). Microscale Cu particles were sprayed onto the polymer surface (i.e., polyamide) using the cold spray parameters listed in Table 17. The effect of cold spray parameters on particle deposition phenomenon was further investigated by numerical modeling.

Table 17 Cold spray operating parameters

Operating parameter	Operating constants
Gas inlet pressure	0.5 MPa
Gas inlet temperature	298 K
Nozzle transverse speed	0.1 m/s
Nozzle stand-off distance	10 mm

7.2.3 Numerical modeling

The numerical modeling is simulated to capture the high-velocity impact of cold-sprayed particles. Simulation properties and material modeling details setup can be found in chapter 3 and chapter 5.

7.2.4 Co-electroless deposition

Following the cold spray particle deposition, a co-ED process was applied to obtain high-electrical conductivity on the polymer surface. Here, the as-cold sprayed layer was utilized as the catalyst side for the subsequent co-ED process. As such, the polymer surface was functionalized as conducting polymer. Then, the electroless over-coating process was applied by following a published recipe [153]. The ingredient of the co-ED over-coating process is presented in Table 18. In the co-ED process, Cu sulfate is used as a Cu^+ source, ethylenediaminetetraacetic (EDTA) and hydrochloric acid (HCl) are complex agents, sodium hydroxide (NaOH) is pH stabilizing agent, potassium ferricyanide ($\text{K}_3[\text{Fe}(\text{CN})_6]$) is a stabilizing agent. Lastly, formaldehyde (CH_2O) is the reducing agent that initiates the metal ion chemical deposition process. A set of co-ED times (i.e., 2, 4, 8, 16, and 24 hours) was applied to characterize the over-plating process better.

Table 18 Chemical ingredients of the co-ED process

Content	Volume
Cu sulfate	18 (g/L)
EDTA	48 (g/L)
Sodium hydroxide	48 (g/L)
Hydrochloric acid	18 (mL/L)
Potassium ferricyanide	0.05 (g/L)
DI water	1 (L/L)

7.3 Results and discussion

7.3.1 Cold spray particle impact

The simulation results of high-velocity cold spray particle impact on polymer surface are shown in Figure 7-3 (a-c). Herein, the initial particle velocity was set to 50 m/s, 150 m/s, and 300 m/s, and the particle size diameter was 40 μm for all testing conditions. The initial particle velocity was applied between 50 m/s – 300 m/s, considering that the cold spray system's input air pressure applies between 0.5 MPa to 0.7 MPa. Our previous study has validated the correlation between the pressure and the initial velocity [159]. The compression ratio was taken from the original Cu shape and after impact. The maximum rebounding velocity value was calculated right before the particle separation from the polymer surface. The rebound kinetic energy value was obtained from the rebound velocity and a set of mass values (see Figure 7-3 (d-e)). The simulation results reveal that

Cu particles impinge on the polymer substrate without deformation, unlike the cold spraying of metal particles on a metal substrate (e.g., Cu particle deposition on a stainless-steel substrate). This is likely attributed to the mechanical interlocking phenomenon between the Cu particles and the polymer substrate.

The results reveal that as the initial velocity increases, the Cu particle substantially impinges into the polymer substrate. In Figure 7-3 (d), the impact velocities are plotted against the Cu particle's compression ratio after the particle's rebounding at 50 m/s shown in Figure 7-3 (e). After impact, the particle retained its original shape, and a lower rebound velocity was observed compared to the impact velocities of 150 m/s and 300 m/s. The compression ratio of the Cu particle increased while the polymer substrate was heavily deformed as the impact velocity increased (see Figure 7-3 (d)). Figure 7-3 (e) presents the rebound velocity and the rebound kinetic energy against particle impact velocity. The results show that the rebound velocity and the rebound kinetic energy increase proportionally with increasing impact velocity. The analytical deformation data obtained from the simulation results can be used further to analyze the cold spray deposition of Cu particles.

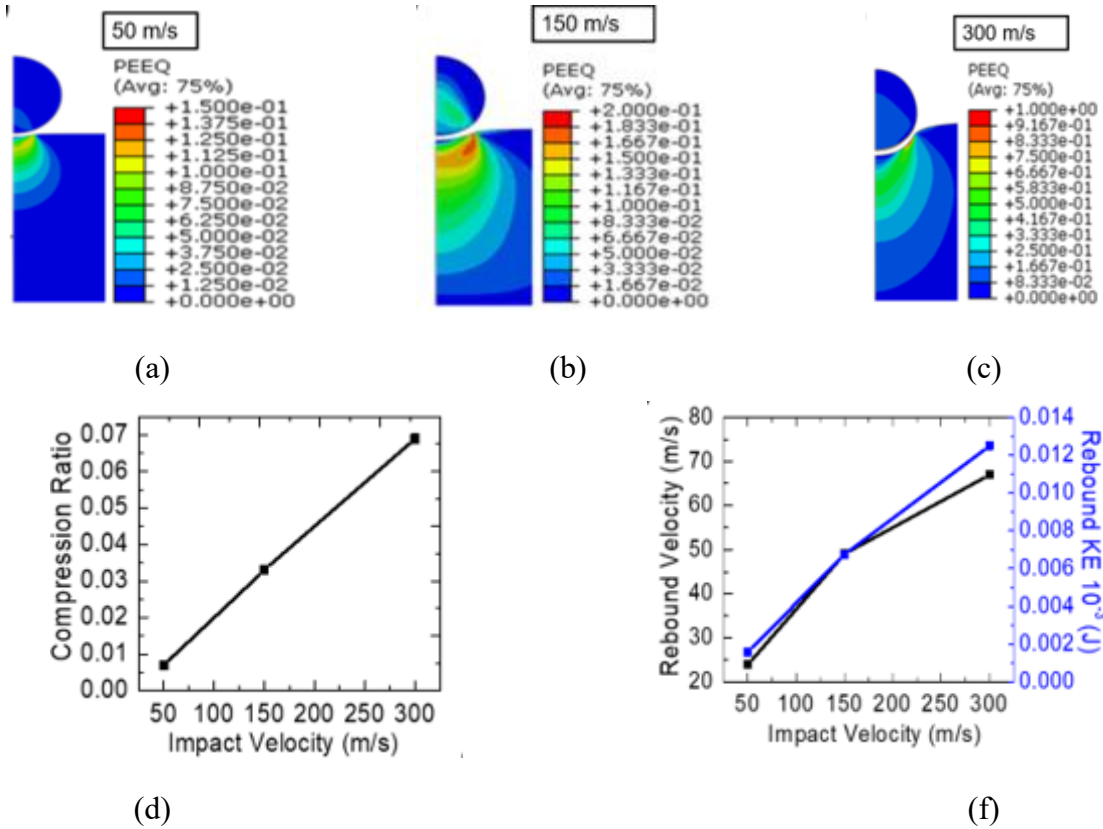


Figure 7-3 Simulation results of single Cu particle (40 μm) impacting on the polymer surface at an impact velocity of (a) 50 m/s, (b) 150 m/s, (c) 300 m/s particle velocities; (d) Cu particle compression ratio after a rebound for different impact velocities, (e) rebound velocity and kinetic energy variation against particle impact velocity

Figure 7-4 (a-c) shows the different size particle (i.e., 5, 10, and 40 μm) impact on the polymer surface at a constant velocity of 300 m/s. Considering that the hardness of polymers is minor than metal, simulation results suggested that Cu particles can impinge into a polymer substrate at an impact velocity of 300 m/s. Furthermore, as shown in Figure 7-4 (d), the Cu particle compression ratio increases as the particle size decrease. This explains that a smaller particle is more likely to be deformed than a bigger particle at constant impact velocity. Moreover, the rebound kinetic energy increases while the rebound velocity decreases with increasing particle size (see Figure 7-4 (e)). Thus, a smaller particle has less rebound kinetic energy and is likely to stick onto the polymer substrate. On the other hand, a larger particle is likely to have higher kinetic energy due to its higher mass and is less inclined to attach to the polymer substrate. The simulation results contributed helpful information for the experimental cold-spraying and subsequent co-ED process.

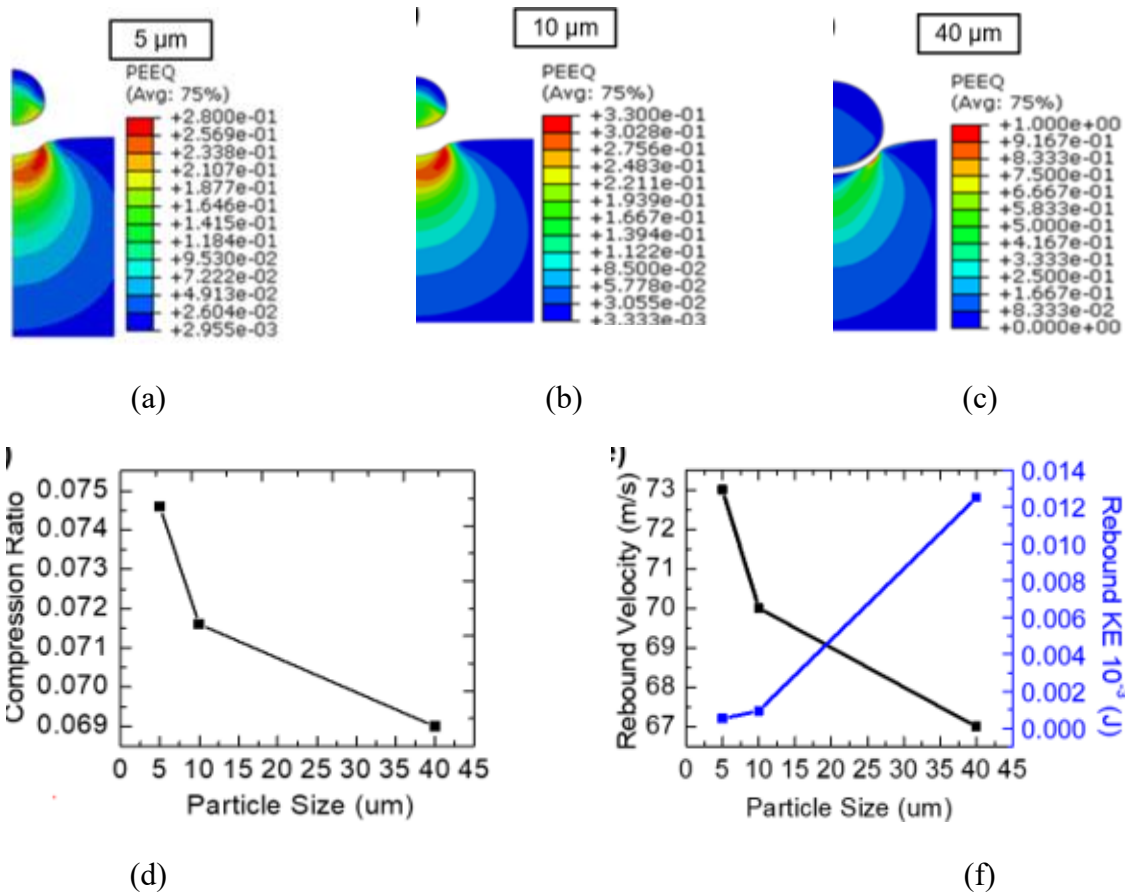


Figure 7-4 Simulation results of different-size single Cu particle impacting on the polymer surface at a constant impact velocity of 300 m/s; (a) 5 μm , (b) 10 μm , (c) 40 μm particle velocities; (d) Cu particle compression ratio after a rebound for different particle sizes, (e) rebound velocity and kinetic energy variation against particle size

7.3.2 Microstructure investigation

Figure 7-5 shows the top surface scanning electron microscopy (SEM) analysis of the as-sprayed polymer surface after 2 hrs, 4 hrs, 8 hrs, 16 hrs, and 24 hrs of co-ED, respectively. The as-sprayed specimen shows the single-particle attached firmly onto the polymer substrate, including micro-porosity and severe void formation (see Figure 7-5 (a)). When the co-ED process is introduced, the voids between the polymer base material and the Cu particles are filled. At 24 hrs co-ED, the surface was utterly over-plated with Cu particles, and no porosity was observed (see Figure 7-5 (f)). This result suggests that a subsequent over-plating process could overcome the severe erosion on the polymer surface by gaining electrical conductivity.

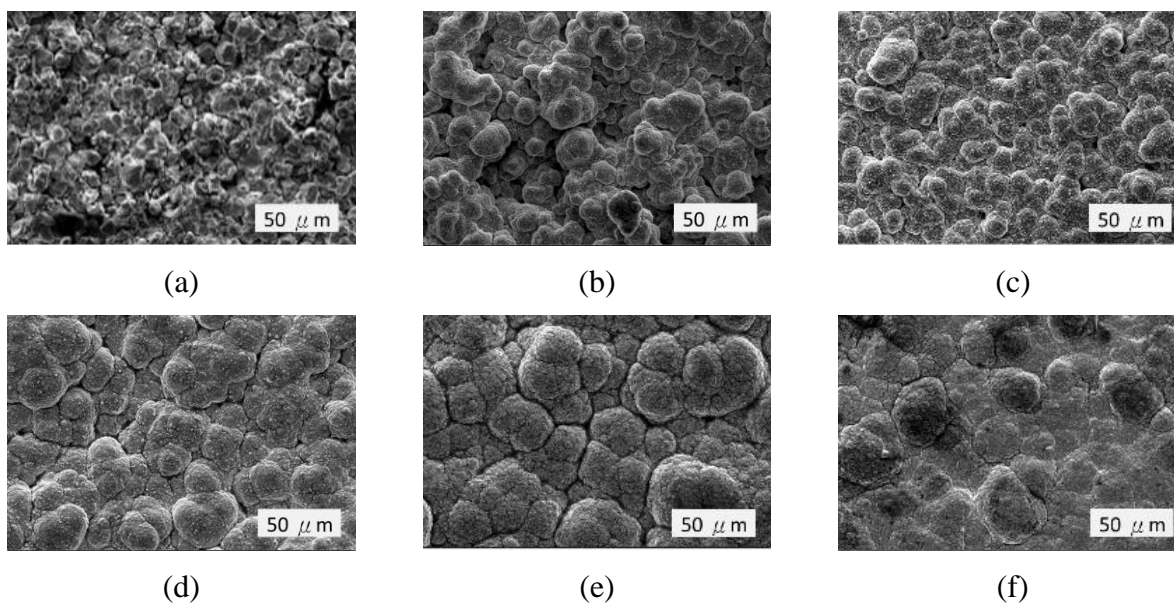


Figure 7-5 Surface morphology of (a) as-sprayed and eletroless-plating (b) 2 (c) 4 (d) 8 (e) 16 (f) 24 hrs

Figure 7-6 presents the cross-section SEM images of the samples described above. The cross-section of as-sprayed specimens shows the splat morphology, voids, defects, and interface boundaries between the particle-particle and particle-substrate junctions (see Figure 7-6 (a)). As the co-ED time increases, the deposition thickness increases as well. At 24 hrs of deposition, the average thickness reaches up to 100 μm , forming a bulk conductive layer. The electroless deposition was found beneficial to functionalize/modify the polymer surfaces in an electrically-conductive manner for the as-cold sprayed polymer substrates.

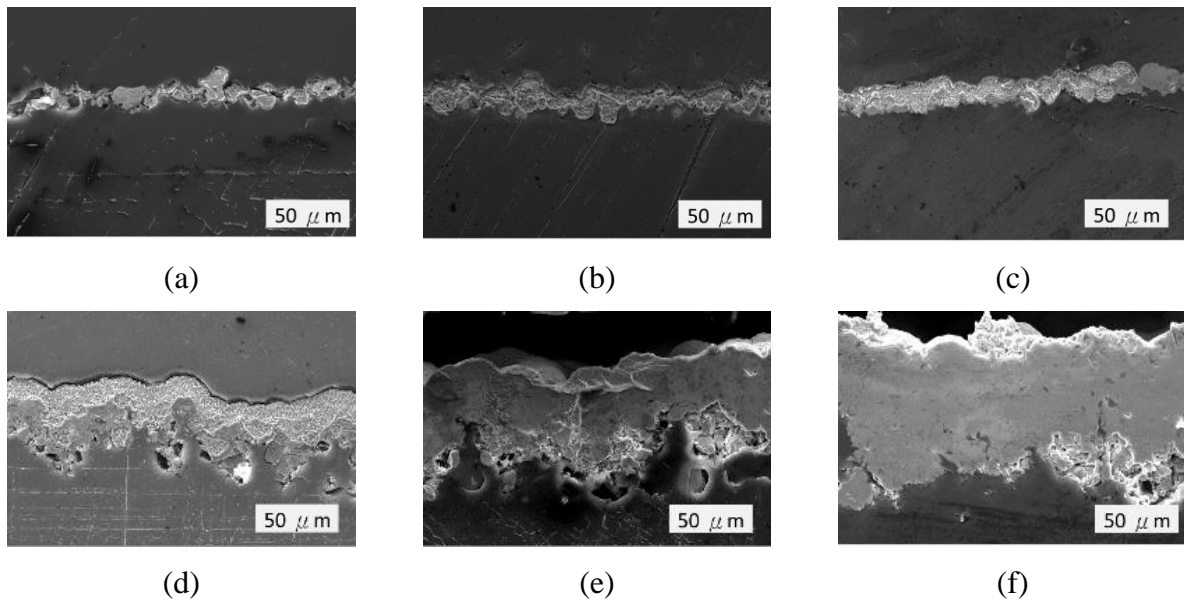
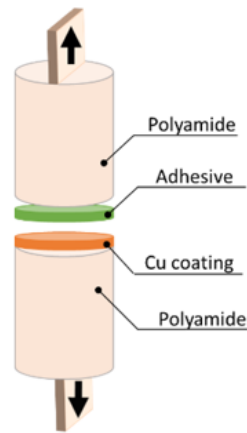


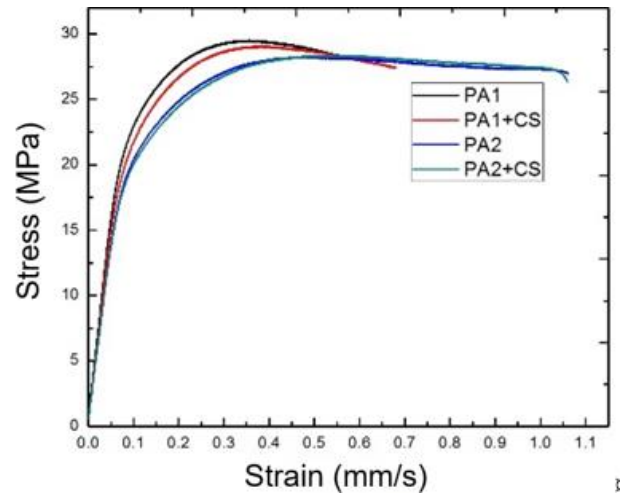
Figure 7-6 Cross-section of (a) as-sprayed and eletroless-plating (b) 2 (c) 4 (d) 8 (e) 16 (f) 24 hrs

7.3.3 Adhesion testing

The adhesion testing of the samples was characterized based on the ASTM C633 [14] standard (i.e., pull-off adhesion test). A 22 KIP hydraulic MTS 810 load frame was used in this experiment for both the adhesion test and the tensile test. The crosshead displacement rate was set to 1 mm/min according to the ASTM D3039 [160]. The substrate/coating interface's adhesive strength was measured by attaching the substrate/coating specimen to the caps (fixtures) and then applying a tensile force to the fixtures to cause the substrate/coating dis-bonding (see Figure 7-7 (a)). The substrate/coating can display a cohesive fracture with crack propagating through the coating layer or an adhesive fracture at the substrate-coating interface. The test results are disregarded if the substrate/coating disbands from the caps. The adhesion strength of the coating on polymer substrate (<20 MPa) is typically much lower than the adhesive strength of the specimen/fixture bond (250 MPa) [18].



(a)



(b)

Figure 7-7 (a) Schematic of the pull-off adhesion test, (b) stress-strain results of bulk and as-cold sprayed polyamide 6 polymers

Adhesion testing was conducted on as-sprayed specimens, electroless deposition of 4 hrs specimens, and 16 hrs specimens. Each of the testings was performed for three specimens. After testing, each set of test results were averaged, as shown in Table 19. The adhesion strength of as-sprayed specimens has the highest adhesion strength. The adhesion strength decreases as the co-ED time increases. While the adhesion test suggested that the specimens should have a flat surface between the connections of the coated surface, it is difficult to achieve in this test fully. It can be observed that the as-sprayed specimens and the electroless-deposited specimens have high roughness and surface contour (See Figure 7-5 and Figure 7-6). This may overall influence the results of the adhesion strength. For all the as-sprayed specimens, the failure occurs between the epoxy and the polyamide 6 sides. The same failing occurs in the 4 hrs specimens. However, for the 16 hrs specimens, an adhesion failure occurs between the metal and the epoxy (i.e., half of the coated Cu metal attached to the epoxy while the other half is on the polyamide side). The results indicate that the adhesion performance of the as-cold sprayed samples is stronger than the co-ED samples, which is likely attributed to the mechanical interlocking of the Cu particles with the polymer material after cold-spraying. On the other hand, co-ED is such a chemical deposition process, which offers less adhesion performance than cold spray deposition, which lies on the mechanical bonding phenomenon.

Table 19 Adhesion test results of as-sprayed and electroless deposition specimens

Electroless (hrs)	Adhesion strength (MPa)
0 (as-sprayed)	10.2 ± 0.35
4	7.5 ± 0.81
16	4.8 ± 1.15

7.3.4 Mechanical strength

The tensile test was conducted on cold spray coated specimens to verify the strength of the resultant coating. The polyamide 6 dog bone specimens were manufactured having a thickness of 0.2 mm [160]. The polyamide 6 dog-bone specimens labeled PA1 and PA2 are the unsprayed specimens, while the PA1+CS and PA2+CS present the as-cold sprayed specimens. The tensile strength was compared with the sprayed and the unsprayed specimens. One-pass for cold spraying was conducted for the sprayed specimens, keeping some regions not coated with Cu particles. This was intentionally done to observe if the un-coated area may influence the tensile strength. The results show that the coated specimens retained their tensile strength compared with the uncoated coupons (see Figure 7-7 (b)). No significant increase or deterioration of tensile strength was observed within the sprayed specimens. As such, the erosion on the polymer surface after the cold spray process is not severe in terms of mechanical strength. It should be noted that these results are valid under the cold spray parameters used in the present study.

7.3.5 Electrical conductivity

A four-point probes apparatus measured the volume resistivity (i.e., electrical resistivity) (see Figure 7-8 (a-b)). As shown in Figure 7-8 (b), the four-point probes were designed in which the outer two probes measure current, and the inner two probes measure voltage. Several coated distances were measured using the following equation to determine the volume resistivity per-cross-sectional area (27).

$$R = \rho \frac{\ell}{A} \quad (27)$$

R is the electrical resistance of the coating layer on the substrate calculated from the measured current and voltage, ρ is the electrical volume resistivity, ℓ is the length of the specimen, and A is the cross-section area of the coating.

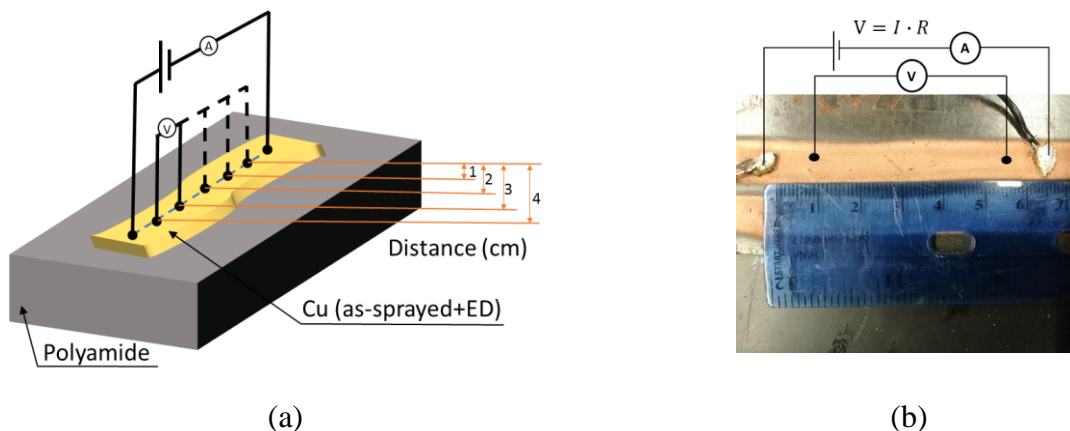


Figure 7-8 Four-point probe measurement; (a) a schematic of setup (b) experimental setup

The four-point probe method was measured on all the coated specimens. The concept is to prove that the Cu-coated layer is high-electrically conductive. The measured value of electrical resistivity ranges from $5.3 \times 10^{-6} \text{ } (\Omega \cdot \text{m})$ to $2.16 \times 10^{-7} \text{ } (\Omega \cdot \text{m})$ for the co-ED specimens of 4 hrs- 24 hrs. The measured value was one magnitude lower than the bulk copper resistivity, approximately $2.65 \times 10^{-8} \text{ } (\Omega \cdot \text{m})$. This is likely attributed to surface roughness, voids, and defects caused by cold spray coating [17]. Overall, the resultant coating has high-electrical conductivity between the measurement range of graphite to Cu electrical resistivity.

Lastly, the electrochemical measurement was performed by cyclic voltammetry (CV) experiments using an apparatus of SP-300 Biologics equipped with the Elab software. All the as-sprayed and electroless deposition specimens were cleaned with DI water to avoid the chemical residual. The voltammetry cycle for E was set from 3.5 to -4 (V) at a constant scanning rate of 80 mV/s. The behavior of Cu and CuO in 0.4 M KOH was then examined. The 24 hrs of electroless deposition specimen were used to conduct a cyclic voltammetry test. The over-coated specimen is the working electrode in this experiment. Figure 7-9 shows that the x-axis is the applied potential E, while the y-axis is the current response. The reduction and oxidation curves were cycled five times to see the stability. The CV results demonstrate a potential tool to probe reactions between electron transfers of the resulting electrode (i.e., 24 hrs co-ED sample).

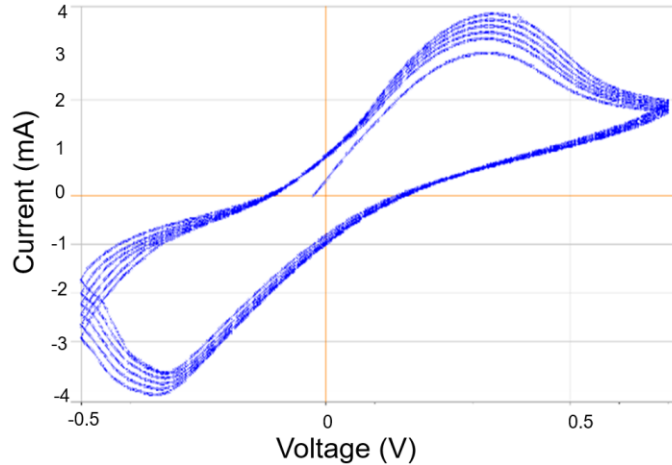


Figure 7-9 Cyclic voltammetry results of 24 hrs electroless plating specimen

7.4 Conclusion

Polyimide (Nylon 6) substrate was deposited with cold sprayed Cu particles and further over-plated by a subsequent electroless plating process. Finite element analysis was conducted to simulate the morphology changes of Cu particles upon impact on the polymer substrate. A viscoelastic model was implemented to the substrate to capture the Cu impact on/into the polymer. It was observed that Cu particles were mechanically interlocked into the polymer substrate under described cold spraying parameters. Moreover, particle's plastic deformation, rebound velocity, and kinetic energy increase with an increasing impact velocity.

Conversely, the particle's kinetic energy decreases when the rebound velocity increases. The as-sprayed specimens retained their intrinsic tensile strength even after high-velocity impact during cold spraying. The surface and the cross-section morphology analyses provided useful information for both cold spraying and the co-ED process. The adhesion test revealed that adhesion strength decrease as the coating layer increases with co-ED over-plating. High-electrically conductive electrodes were achieved hybridizing the cold spraying process with a subsequent electroless deposition, and cyclic voltammetry results proved the electrochemical stability of the resultant electrodes. The present study results uncover the process-structure properties of cold spraying and co-electroless deposition process, which can pave the way for sustainable electronics applications.

8. COLD SPRAY MULTILAYER METAL BUILD-UP ON A POLYMERIC SUBSTRATE

The content of this chapter is submitted to the ASME 2022 17th International Manufacturing Science and Engineering Conference.

Cu and Sn were low-pressure cold sprayed onto polyamide 6 (PA 6) and polypropylene (PP) substrates. The first layer of Sn and Cu was built onto the polymer substrate and continued as an alternative layer of Cu and Sn build-up under controlled process parameters. The chronological order of either first spraying Cu or Sn does not hinder building a coated layer on the PA 6 and PP substrate. The coating thickness can reach as thick as 100 μm of the PA 6 (Cu/Sn/Cu) layer. Results show the potential ability for additive manufacturing using polymeric templates. The cold spray kinetic bonding of the metals avoids any intermediate phase formation. The mechanical performance of the coated material remains the same as the deposition process does not degrade bulk substrates. The contour of the interface and the surface roughness resulting from the cold spray coating process lead to a deformed surface layer of the polymer on the particle size of the powder used for cold spraying. While the metallic coating deforms via plastic deformation and cracking, the through-thickness cracks, which primarily are perpendicular to the loading direction, do not span the width of the coating due to the tortuous nature of the microstructure. The advantage provides electrical conductivity to strains of up to 10 % and maintains a low electrical resistance.

8.1 Introduction

The ability to metalize polymeric materials with robust and reliable coatings enables a wide range of additional functionality in electrical, thermal, or mechanical applications [19]. One coating technique that provides flexibility in material systems and part geometry (i.e., coating non-planar substrates) is cold spray coating. The pros are that no temperature requirement or vacuum system is needed and spray with the desired patterns without alternating current manufacturing methods on a wide range of substrate geometries. The cons are that cold spray may mechanically damage the substrate while continuous particle impact before forming a coated layer [1, 16]. Che, et al. [28] used a mixed ratio of powder Sn and Cu. It shows a better coating adhesion towards the substrate. This is because Sn has a low melting temperature. During the high impact velocity, Sn

was melted and mechanically interlocked onto the rough surface of the polymer. The Sn on the surface has an irregular shape that increases the adhesion strength. The continuously mixed ratio of Cu and Sn was sprayed onto the Sn coating. This method succeeded in building a relatively thick layer of coating. Nevertheless, no substantial improvement in the electrical performance was achieved by adjusting the Cu/Sn metal ratio. It was concluded that the Cu/Sn interfaces might be a barrier to low conductivity.

Previous studies have focused on controlling the process parameter to achieve the first coating layer on polymer substrate [159]. To create robust coatings of multiple conductive layers of metals onto polymers, there must be strong adhesion between the metal and polymer [161]. Furthermore, cold sprayed metal films on the polymer substrate should sustain considerable strain without rupture or delaminating. Substrate damage tends to scale with the impact pressure of the metallization process, so there is a drive to utilize low-pressure cold spray for thinner polymeric systems [18]. Using a low-pressure cold spray device to form a conductive coated layer on soft polymer substrates would enable localization and patterning with fewer process steps than masking with electroless plating [153, 156].

This work aims to conduct a low-pressure cold spray Sn/Cu (soft/hard particles) coating for building multiple layers while at the same time without destroying the polymer substrate. Room temperature is applied while spraying; this is to avoid softening the polymer substrate. The microstructure of the cold spray coated specimens is investigated of the cold sprayed dual layer of Cu-Sn polymer substrate. A parametric study of spray is deployed to understand the possibility of building layer by layer coating. The mechanical performances and the electrical resistance of the coated layer are measured as well.

8.2 Materials preparation and experimental process

Figure 8-1 (a) shows the setup of the cold spray coating used for coating polymers. We have organized into three main points, the first is the safety setup, the second is the robotic control, and finally, the safety protection gear. A KUKA KR 6 R700 Sixx was operating in this cold spray research. The 6 axes robotic arm is equipped with a 6 kg payload at its maximum stretch distance of 706.7 mm. The steel base pedestal was anchored into a concrete floor and sealed with cement. The position is fixed on the left of the wet downdraft to allow more space for the operator to access from the right side downdraft. The distance also considers the robotic arm work distance shown in

Figure 8-1 (b) for making sure the robotic arm can reach the spray path. The robot arm is mounted on a steel base pedestal (36''x14''x14'); note: the robotic arm goes with metric. A fixture holder was designed for connecting the cold spray and the robotic arm. A wet downdraft for combustible dust (DualDraw, LLC) was set up in the lab for the cold spray coating. The equipment meets the standard of NFPA 484 for combustible metals and OSHA Standard 1910.1000. The process parameters for the coating are organized in Table 20.

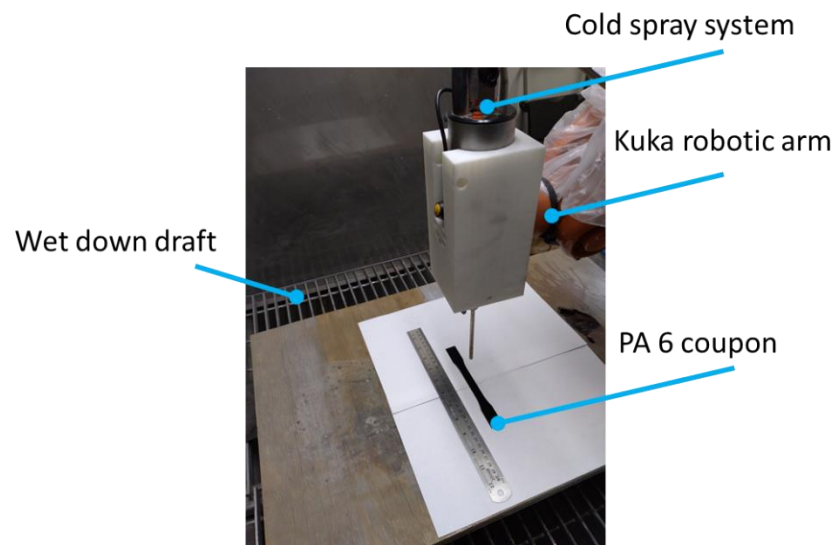


Figure 8-1 Cold spray system setup

Table 20 Cold spray operating process parameters

Operating parameters	Operating constants
Gas inlet pressure	0.5 MPa
Gas inlet temperature	Room temperature
Nozzle transverse speed	0.1 m/s
Nozzle stand-off distance	10 mm

PA 6 (Polyamide 6) and PP (Polypropylene) (both substrate thicknesses 3.175 mm) were acquired from ePlastics®. For this work, we used planar substrates, but the technique can easily be extended to three-dimensional parts. The polymer substrate was cut using a waterjet into the form of tensile test specimens according to ASTM D638. Figure 8-2 shows the DSC results of the PA 6 and PP used in this study. A scan rate of 10 °C /min from room temperature to peak 300 °C for PA 6 and 180 °C for PP. A 1.5 thermal cycle was conducted on the specimens to ensure that any residual crystallization was melted. The PA 6 melting temperature is between 230-280 °C, and the crystallization temperature is around 230 °C. For PP, the melting temperature is between 130-170 °C, and the crystallization temperature is around 120 °C.

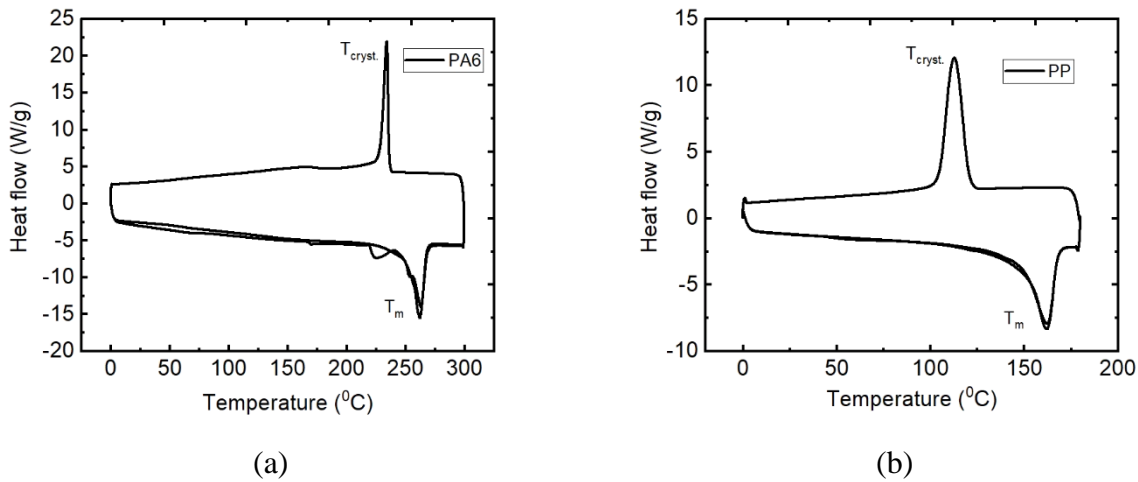
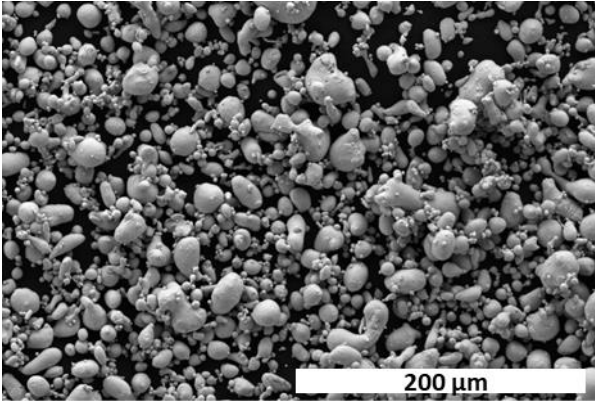
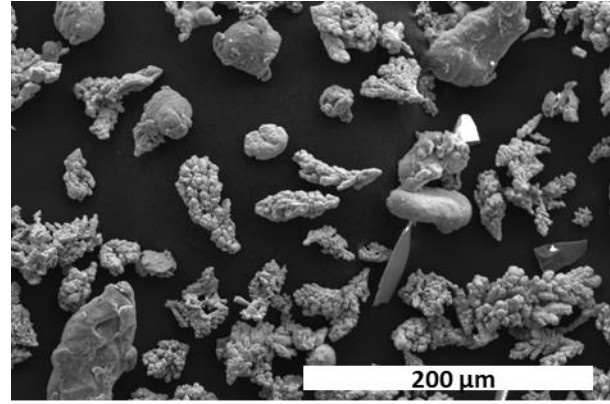


Figure 8-2 DSC results of (a) PA 6 and (b) PP

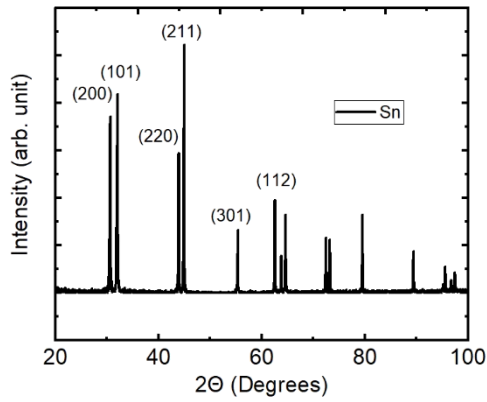
Figure 8-3 (a) and (b) show the SEM images of the commercially available Sn and the Cu powder provided by CenterLine (both powder particle sizes range between 5 -45 μm , info provided by the vendor). The Cu powder for cold spray typically adds a small portion mixed with Al and powder. The XRD result shows the Sn Figure 8-3 (c) and the Cu powder structure in Figures (d).



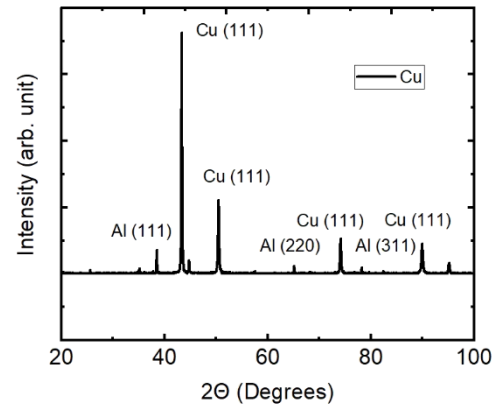
(a)



(b)



(c)



(d)

Figure 8-3 SEM powder morphology of (a) Sn (b) Cu and XRD results of (c) Sn and (d) Cu before cold spray

Figure 8-4 shows Cu coated on the PA 6 and PP substrate and spray Sn as the dual-layer on the Cu layer. The same is conducted but spray Sn first and Cu as the second layer on the PA 6 and PP substrate. A total of 8 different coating parameters. The cold spray inlet air pressure is fixed at 0.5 MPa with a spray distance of 10 mm. A one-pass spray was conducted for each specimen.

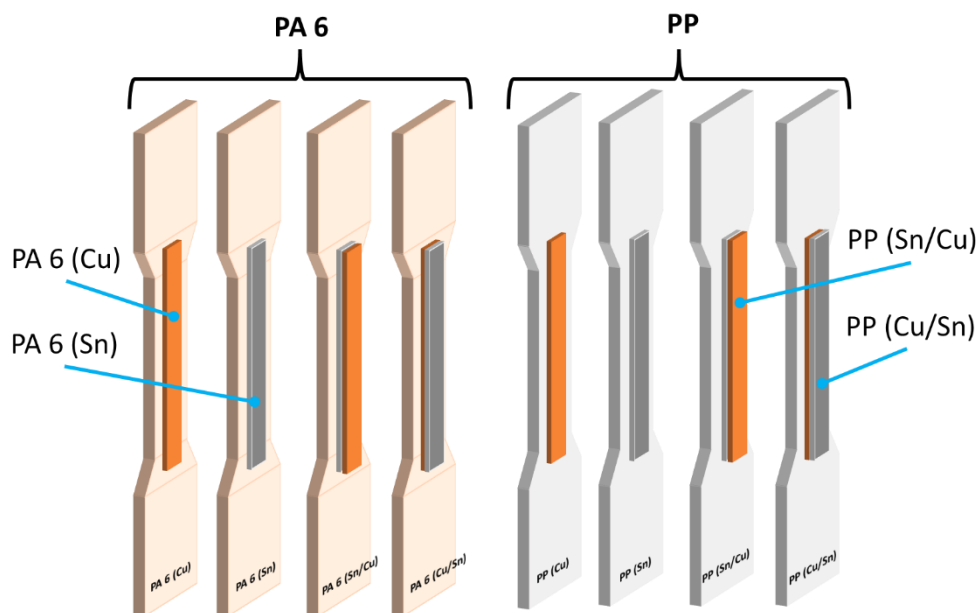


Figure 8-4 Specimens of cold spray Cu and Sn on PA 6, PP and continue to spray Sn or Cu to build the dual-layer

Figure 8-5 shows the XRD result after Cu coated on the PA 6 substrates compared with Cu powders (mixed with Al powders). The Cu did not oxidize after being coated onto the polymer substrate. Also, the XRD results did not show any Al powders detection. Therefore, it is suggested that Al did not form any coated layer, and only the Cu was embedded into the polymer substrate.

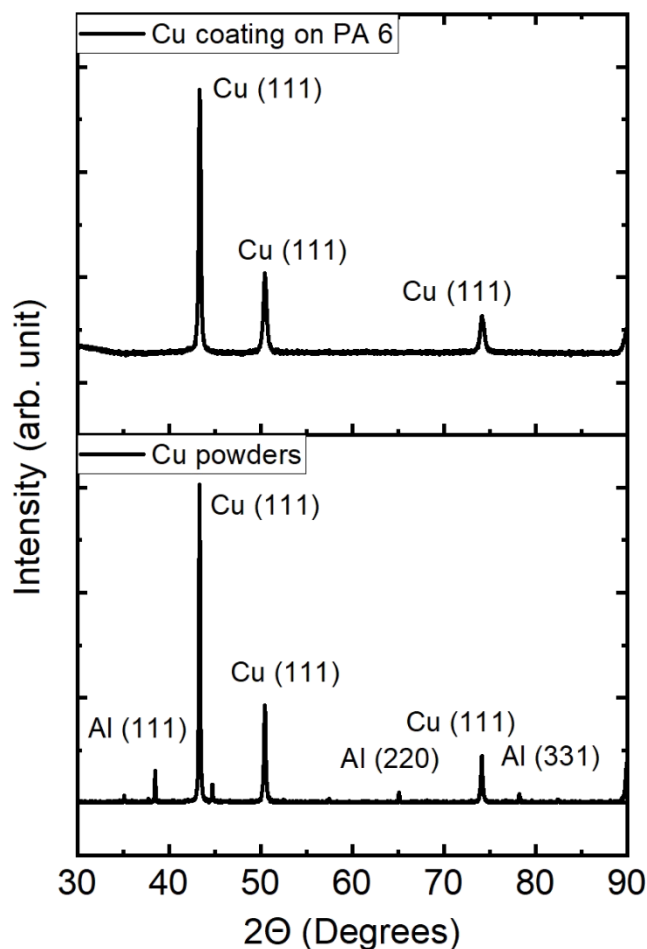


Figure 8-5 XRD results of cold sprayed Cu on PA 6 comparing with only Cu powders

8.3 Results and discussion

8.3.1 Microstructure characterization

Figure 8-6 (a) Cu on PP, (b) Cu on PA 6, (c) Sn on PP, and (d) Sn on PA 6 shows the SEM surface images. Figure 8-6 (a) is a partial coating; portions of the polymeric substrate are visible between the Cu-coated regions. Figure 8-6 (b) show similar results, but individual Cu particles are more identical and exposed. Figure 8-6 (c and d) shows Sn coated onto PP and PA 6. All Sn coated onto the polymer substrate and able to form a coated layer. Figure 8-6 shows that there are residual particles attached to the as-coated layer in the coated surfaces.

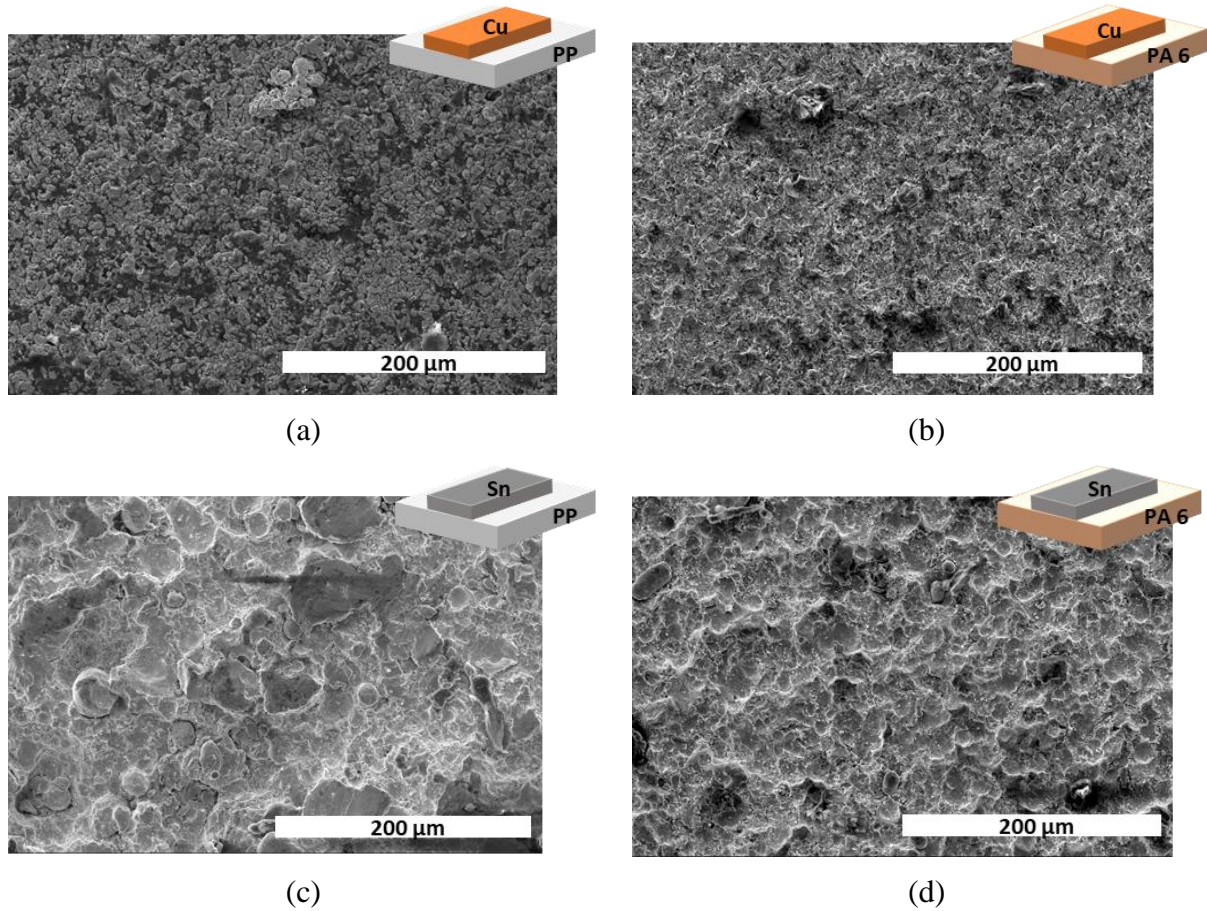


Figure 8-6 SEM images of surface morphology (a) PP (Cu) (b) PA 6 (Cu) (c) PP (Sn) (d) PA 6 (Sn)

Figure 8-7 shows the SEM image of cross-section polished single Cu particle impinges into PA 6 (the specimen is from Figure 8-6 (b)). Cu particles do not form a contiguous layer; individual particles were separately mechanically interlocked into the polymer substrate.

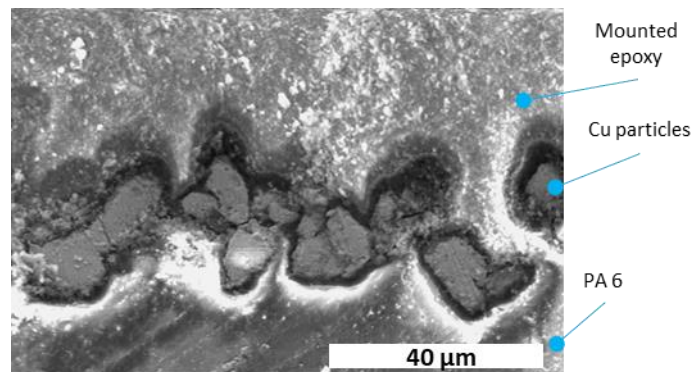


Figure 8-7 Cu particle impinges into the PA 6 substrate

Figure 8-8 (a) PP (Cu/Sn) (b) PA 6 (Cu/Sn) (c) PP (Sn/Cu) (d) PA 6 (Sn/Cu) shows the SEM surface images of dual-layer coating. The specimens are first coated with either Cu or Sn, shown in Figure 8-7; a second layer coating is applied again with either Cu or Sn. Figure 8-8 (a and b) shows that the crack occurs after Sn is coated onto the second layer. This suggested that the Sn coated is reaching its coating thickness limit using the same process parameters, and further proceeding will induce surface cracks. Figure 8-8 (c and d) shows the surface layer of Cu coated on the first layer of Sn, but with no crack occurring.

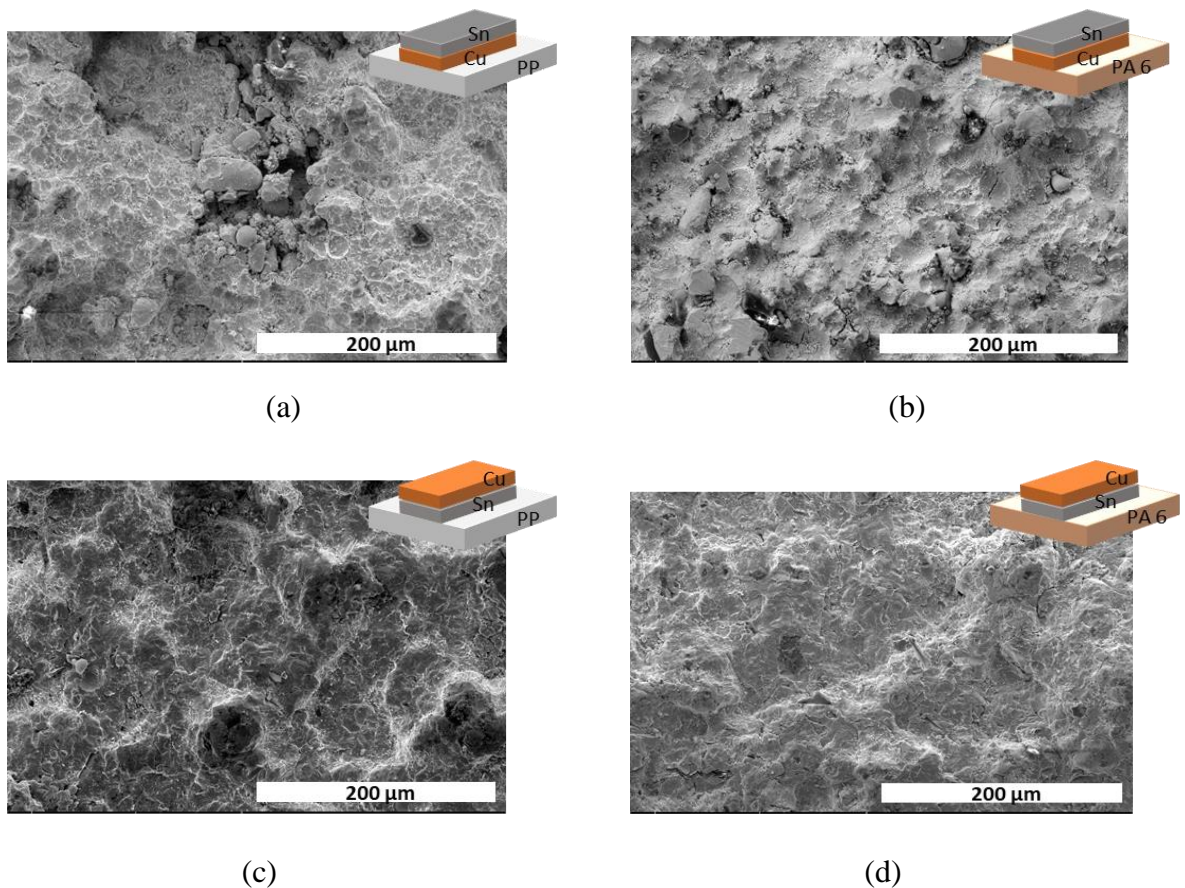


Figure 8-8 SEM images of surface morphology (a) PP (Cu/Sn) (b) PA 6 (Cu/Sn) (c) PP (Sn/Cu) (d) PA 6 (Sn/Cu)

To continue the effort of coating layers on the coated substrate. This research has taken Cu/Sn coated PA 6 specimen (Figure 8-8 (b)) and coated an additional layer of Cu on it. Figure 8-9 (a) shows the SEM image of the Cu/Sn/Cu layer deposited onto the PA 6 substrate. The interface between the Cu and the polymer substrate is very contoured. In addition, EDS images were mapped for the cross-section of the SEM image. Results show that some Cu particles were on the substrate, followed by an Sn-coated layer and a Cu layer. The process parameters are fixed while spraying Cu and Sn powders. While this method can achieve a coating layer, the coating thickness is not consistent. Some local locations did not form a coating thickness, while some areas formed a layer. The main reason is that continuous particle impact results of highly rough contour coated area onto the polymer substrate. Thus, process parameters play a significant role in cold spray coating.

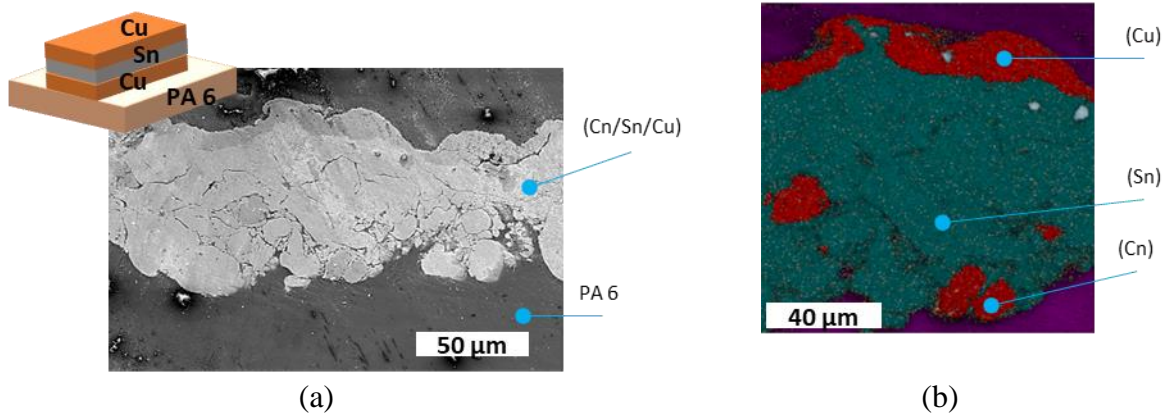


Figure 8-9 on PA 6 (Cu/Sn/Cu) (a) SEM of the polished cross-section (b) EDS map results

8.3.2 Mechanical performance

The mechanical strength of the coated (Cu and Cu/Sn) and uncoated polymer substrates are shown in Figure 8-10 (a and b). The coated specimens retained their original bulk strength, demonstrating that low-pressure cold spray metals can be applied to these two polymer systems with no significant mechanical degradation of the overall structure.

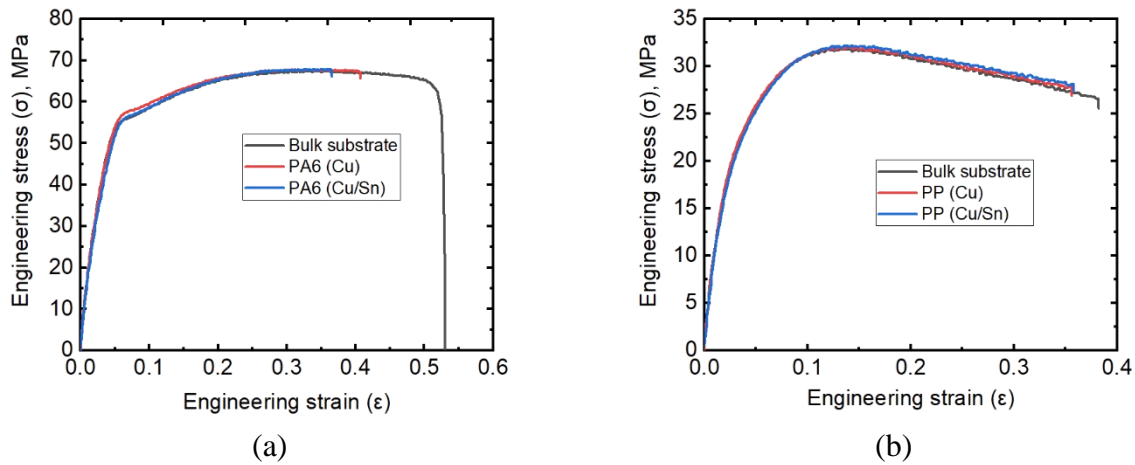
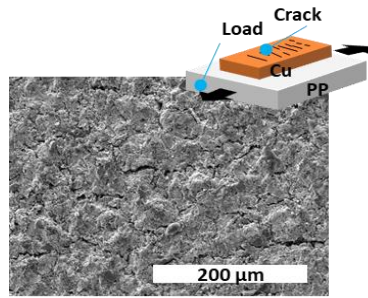
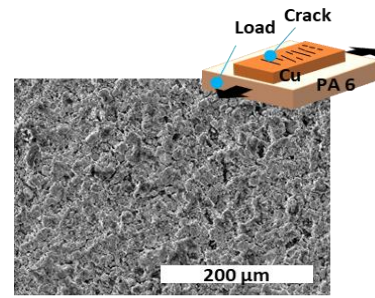


Figure 8-10 Stress and strain results of bulk and coated (a) PA 6 specimens (b) PP specimens

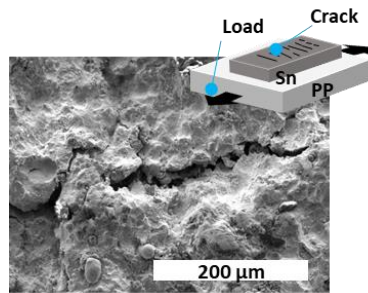
Metals usually do not easily crack to strains of 10 %, which the polymeric substrate can sustain [125]. As such, we expect to see either plastic deformation or fracture occurring in the metal coating. Figure 8-11 shows plan view images of the metalized surface after the mechanical tensile test of the eight different coated specimens. Figure 8-11 (a-b) shows that the particle gap increases after the specimen's mechanical failure. Figure 8-11 (c-h) results show cracks are mostly vertical to the tensile test direction. However, there are minor cracks that also have occurred but are not perpendicular to the load direction. The SEM images show cracks from splitting, shearing, crushing, and microcrack at different angles of failure. Different cracks are because of unevenly coating morphology to the substrate, found in Figure 8-7.



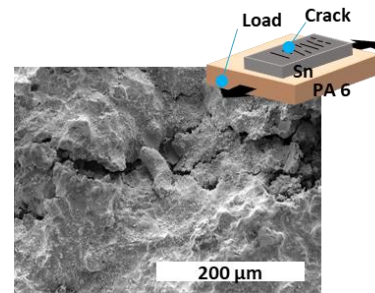
(a)



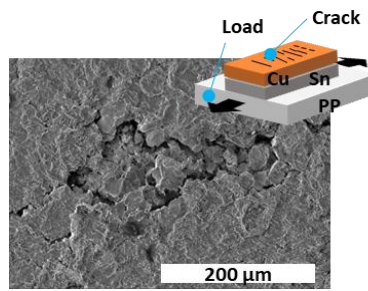
(b)



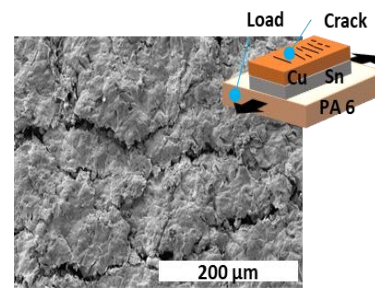
(c)



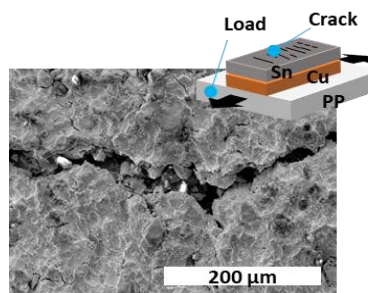
(d)



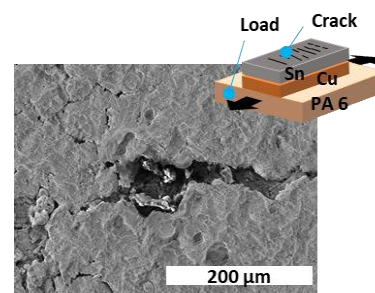
(e)



(f)



(g)



(h)

Figure 8-11 Crack behavior observation on specimens surface of (a) PP (Cu) (b) PA 6 (Cu) (c) PP (Sn) (d) PA 6 (Sn) (e) PP (Sn/Cu) (f) PA 6 (Sn/Cu) (g) PP (Cu/Sn) (h) PA 6 (Cu/Sn)

8.3.3 Electrical performance

After coating, the electrical resistivity of the eight different coated spray specimens was measured. Only the specimens that are coated with Cu on the PP and PA 6 were not electrically conductive. The Cross-section SEM results in Figure 8-7 show that the Cu particle is embedded into the polymer substrate from the low-pressure cold spray. Other sprayed specimens have an electrical resistivity between 14.4×10^{-6} ($\Omega \cdot m$) to 7.8×10^{-7} ($\Omega \cdot m$) shown in Table 21. The Cu electrical resistivity is 1.68×10^{-8} ($\Omega \cdot m$), and Sn is 1.09×10^{-7} ($\Omega \cdot m$). However, the continuous cold spray bombarding results in the coating having voids and defects between the layer and layer stacking. Thus, the measured results are one to two magnitude lower than the Cu electrical property. Nevertheless, the results agree well with others [18, 31].

Table 21 The coating materials electrical resistivity

Coated material	Electrical resistivity ($\Omega \cdot m$)	Coated material	Electrical resistivity ($\Omega \cdot m$)
PP (Cu)	NA	PA 6 (Cu)	NA
PP (Sn)	0.78×10^{-6}	PA 6 (Sn)	10.5×10^{-6}
PP (Cu/Sn)	0.84×10^{-6}	PA 6 (Cu/Sn)	14.4×10^{-6}
PP (Sn/Cu)	0.78×10^{-6}	PA 6 (Sn/Cu)	0.72×10^{-6}

8.4 Conclusion

The results demonstrate the feasibility of cold spray soft and hard particles (Sn/Cu) to form a continuous coating layer on PA 6 and PP substrate. The coated substrates still retained their mechanical strength after cold spray coating. The coated material's microstructure shows that Cu was mainly embedded into the substrate, and Sn was able to form a coated layer onto it. The electrical performance shows that the dual-layer are electrical conductive while the cold sprayed with only Cu specimens are not.

9. SUMMARY AND FUTURE WORK

This chapter concludes the overall contribution and findings in the cold spray metalized polymer materials from simulation to experimental, building devices suitable for measuring the properties and performance of the coatings and possible applications of said coatings.

This research has developed an approach to defining a process window using conventional, commercially available simulation tools to relate process parameters to the resulting metal-polymer adhesion and reliability to improve the efficiency of developing cold spray process parameters. The simulation used a three-network polymer model to describe the polymer's large mechanical strain under high-speed particle impact. The metal particle uses the Johnson-Cook plasticity model during impact, and the ceramic particle uses the Drucker-Prager plasticity model. The computation performances were optimized, and process and material parameters such as particle velocity and particle size were studied to generate a mapped diagram for predicting the adhesion and embedding of the particles into the polymer substrate; this map was compared to experimental results to quantify the conditions that can be used to predict well-adhered coatings.

New experimental techniques for relating powder flowability to deposition efficacy in the cold spray process were constructed and utilized to ensure reliable predictive models. Powder flowability, particle velocity, and mass flow rate were separately measured. A quantitative relationship between the three measurements was investigated. The mass flow rate depends more on the hopper feed rate than the inlet pressure. The result showed that a low power flow angle (spherical powders) produced a higher mass flow rate from the cold spray nozzle; this decreased as the particle velocity increased. Particle size and particle distribution affect the hopper feed rate and indirectly influence the final mass flow rate outcome.

Tradition bonding between heterogeneous materials often involves chemical bonding, and a viable cold spray method would minimize chemical processing. The well-adhered metals and the polymer substrate mechanically interlock the metal coating, excluding chemical solution involvement and ensuring heterogeneous materials' mechanical bonding. However, to quantify the coatings, one must address the wide range of morphologies present in the heterogeneous coating. This work has adapted the fragmentation test with a combination of modified Weibull statistics for qualifying the coating strength of the cold spray coated material. The coating strength results allow us to calculate the interfacial shear strength and the through-thickness toughness of cold sprayed

materials. The measured results provided quantitative measurements compared with conventional standards.

Low-pressure cold spray coating of polymers increases engineering performance without altering original manufacturing processes and mechanical design. These can be achieved by having multiple engineering functions on a system without sacrificing its original engineering performance. For example, the metalized polymer can be electrically conductive while also stretchable and flexible under a specific load. This research has provided two solutions for building electrical conductive coatings onto polymer materials using a low-pressure cold spray system. One is by coating softer and harder metal layers onto the polymer substrate for metalizing polymer. The second is by spraying a single layer of Cu particles into the polymer substrate and conducting the subsequent electroless deposition. The mechanical strength of both coated materials was not compromised after cold spray coating. Microstructural evolution of the cross-sections shows the coating layer can reach as thick as 100 μm . Finally, a design pattern can be easily made by cold spray coating for potential functional sensor applications.

Current work has focused on the cold spray metalized polymer material, from process control to microstructure investigation and increasing engineering performance of the cold sprayed materials. However, the simulation tools setup and measuring devices can further explore other aspects of cold spray coatings. Five main objectives for future works are noted below. These objectives range from software/hardware upgrades to more engineering problems and science questions.

Firstly, simulation tools should include comprehensive process parameters and adapt to actual cold spray manufacturing. Currently, the predicted mapped diagram considers a single spherical particle impact with particle size and particle velocity range. The prediction does not consider multiple particle impacts (mass flow rate), spray nozzle speed, and the model does not include the damage model. Eventually, the particles will damage or erode the substrate at maximum process parameters. In addition, powder morphology, size distribution, and impact angle influence the adhering onto the polymer substrate. Thus, future research plans to explore the cold spray nozzle coating range on different polymer substrates. Understanding the coating process parameters influencing different polymer substrates will be needed.

Another essential objective is to establish the quantitative relationships between powder flowability, particle velocity, and mass flow rate. This research has investigated the powder

flowability, particle velocity, and mass flow rates relationships. Measurement devices address each of the processes. However, the established relationships provide a qualitative connection rather than quantitative relationships. Therefore, the aim should be to measure the powder flow quantitatively and understand the process parameters that affect the final deposition rate to maximize its process efficiency.

The following suggested step is to conduct and plan comprehensive testing for adhesion mechanical-electrical testing and extend the test method to other material systems. Optical microscope resolution has a range, and thus the crack density measurements are limited. The device setup can also be improved, such as the clamp redesign for user-friendly and multiple specimens testing. The four-point probe device should install an auto four-point probe for contacting the coating—software integration and algorithm development for minimizing labor intensity for post-processing images and data collection. Developing a GUI that accommodates all the measurements from the setup device measurements would be beneficial. The output data should include strain, stress, crack density, and electrical resistance measurements. Furthermore, an investigation should be conducted into the adhesion strength differences between coating on a polymer substrate and how the coating process parameters affect the adhesion bonding mechanism—lastly, quantified on different polymer substrates.

In this work, a single soft/hard metal system (Sn/Cu) was explored. Developing more soft and hard metals on polymeric templates for additive manufacturing purposes would be beneficial. In the past, cold spray coating mainly focuses on material repair operation (MRO) of metal to metal. The objective was to be quick and effective in repairing a large area of the damaged surface. This technology has now adapted into additive manufacturing via low-pressure cold spray. Building layers on a polymer template can be either electroless deposition or soft and hard particle deposition. The prediction for using cold spray deposition layer to layer build-up is another logical next step in process control. While building layer by layer, the process parameters should be adjusted accordingly to prevent the coated layer from being destroyed. Current results show the ability to build a Cu/Sn/Cu layer of 100 μm thickness. It is interesting to investigate the possibility of using this method to conduct additive manufacturing.

Finally, after the cold spray process parameters can be measured and controlled, a wide range of applications in cold spray coating on polymer materials can be investigated. For example, metalized polymer (details can be found in chapter 2.3) can be used in laminate armor, alternative

solutions for shot peening or future application for enhancing polymer engineering performances, EMI/RFI shielding and lightning strike application, structural health monitoring, and bioapplications. The potential for combining materials from polymer to metal or ceramic to polymer materials is a great strength of using cold spray tools to achieve the goal.

REFERENCES

- [1] P. C. King, A. J. Poole, S. Horne, R. de Nys, S. Gulizia, and M. Z. Jahedi, "Embedment of copper particles into polymers by cold spray," *Surface and Coatings Technology*, vol. 216, pp. 60-67, 2013/02/15/ 2013.
- [2] D. R. Drodge, B. Mortimer, C. Holland, and C. R. Siviour, "Ballistic impact to access the high-rate behaviour of individual silk fibres," *Journal of the Mechanics and Physics of Solids*, vol. 60, pp. 1710-1721, 2012/10/01/ 2012.
- [3] P. Feng, M. R. Rokni, and S. R. Nutt, "Depositing Aluminum onto PEKK Composites by Cold Spray," *Journal of Thermal Spray Technology*, vol. 30, pp. 385-393, 2021/01/01 2021.
- [4] A. C. Liberati, H. Che, P. Vo, and S. Yue, "Influence of Secondary Component Hardness When Cold Spraying Mixed Metal Powders on Carbon Fiber Reinforced Polymers," *Journal of Thermal Spray Technology*, vol. 30, pp. 1239-1253, 2021/06/01 2021.
- [5] J. Sun, S. Zhou, K. Yamanaka, Y. Ichikawa, H. Saito, K. Ogawa, *et al.*, "Thermal Effects in Sn Coating on a Carbon Fiber Reinforced Plastic by Cold Spraying," *Journal of Thermal Spray Technology*, vol. 30, pp. 1254-1261, 2021/06/01 2021.
- [6] A. Heydari Astaraee, C. Colombo, and S. Bagherifard, "Numerical Modeling of Bond Formation in Polymer Surface Metallization Using Cold Spray," *Journal of Thermal Spray Technology*, 2021/07/19 2021.
- [7] W. Tang, J. Zhang, Y. Li, B. Yu, and J. Zhao, "Numerical Simulation of the Cold Spray Deposition of Copper Particles on Polyether Ether Ketone (PEEK) Substrate," *Journal of Thermal Spray Technology*, 2021/08/27 2021.
- [8] B. AlMangour, "Fundamentals of Cold Spray Processing: Evolution and Future Perspectives," in *Cold-Spray Coatings: Recent Trends and Future perspectives*, P. Cavaliere, Ed., ed Cham: Springer International Publishing, 2018, pp. 3-24.
- [9] H. Assadi, F. Gärtner, T. Stoltenhoff, and H. Kreye, "Bonding mechanism in cold gas spraying," *Acta Materialia*, vol. 51, pp. 4379-4394, 2003/09/03/ 2003.
- [10] M. Grujicic, C. L. Zhao, W. S. DeRosset, and D. Helfrich, "Adiabatic shear instability based mechanism for particles/substrate bonding in the cold-gas dynamic-spray process," *Materials & Design*, vol. 25, pp. 681-688, 2004/12/01/ 2004.
- [11] M. Grujicic, C. L. Zhao, C. Tong, W. S. DeRosset, and D. Helfrich, "Analysis of the impact velocity of powder particles in the cold-gas dynamic-spray process," *Materials Science and Engineering: A*, vol. 368, pp. 222-230, 2004/03/15/ 2004.

- [12] T. Schmidt, F. Gärtner, H. Assadi, and H. Kreye, "Development of a generalized parameter window for cold spray deposition," *Acta Materialia*, vol. 54, pp. 729-742, 2006/02/01/ 2006.
- [13] G. Bae, Y. Xiong, S. Kumar, K. Kang, and C. Lee, "General aspects of interface bonding in kinetic sprayed coatings," *Acta Materialia*, vol. 56, pp. 4858-4868, 2008/10/01/ 2008.
- [14] F. Delloro, M. Jeandin, D. Jeulin, H. Proudhon, M. Faessel, L. Bianchi, *et al.*, "A Morphological Approach to the Modeling of the Cold Spray Process," *Journal of Thermal Spray Technology*, vol. 26, pp. 1838-1850, December 01 2017.
- [15] M. Hassani-Gangaraj, D. Veysset, V. K. Champagne, K. A. Nelson, and C. A. Schuh, "Adiabatic shear instability is not necessary for adhesion in cold spray," *Acta Materialia*, vol. 158, pp. 430-439, 2018/10/01/ 2018.
- [16] A. Moridi, S. M. Hassani-Gangaraj, M. Guagliano, and M. Dao, "Cold spray coating: review of material systems and future perspectives," *Surface Engineering*, vol. 30, pp. 369-395, 2014/06/01 2014.
- [17] R. Gonzalez, H. Ashrafizadeh, A. Lopera, P. Mertiny, and A. McDonald, "A Review of Thermal Spray Metallization of Polymer-Based Structures," *Journal of Thermal Spray Technology*, vol. 25, pp. 897-919, June 01 2016.
- [18] A. Małachowska, M. Winnicki, Ł. Konat, T. Piwowarczyk, L. Pawłowski, A. Ambroziak, *et al.*, "Possibility of spraying of copper coatings on polyamide 6 with low pressure cold spray method," *Surface and Coatings Technology*, vol. 318, pp. 82-89, 2017/05/25/ 2017.
- [19] P. Cavaliere, "Cold-Spray Coatings - Recent Trends and Future perspectives," ed: Springer International Publishing, 2018.
- [20] H. Che, X. Chu, P. Vo, and S. Yue, "Metallization of Various Polymers by Cold Spray," *Journal of Thermal Spray Technology*, vol. 27, pp. 169-178, January 01 2018.
- [21] Z. Khalkhali, W. Xie, V. K. Champagne, J.-H. Lee, and J. P. Rothstein, "A comparison of cold spray technique to single particle micro-ballistic impacts for the deposition of polymer particles on polymer substrates," *Surface and Coatings Technology*, vol. 351, pp. 99-107, 2018/10/15/ 2018.
- [22] H. Ye and J. Wang, "Preparation of aluminum coating on Lexan by cold spray," *Materials Letters*, vol. 137, pp. 21-24, 2014/12/15/ 2014.
- [23] M. Gardon, A. Latorre, M. Torrell, S. Dosta, J. Fernández, and J. M. Guilemany, "Cold gas spray titanium coatings onto a biocompatible polymer," *Materials Letters*, vol. 106, pp. 97-99, 2013/09/01/ 2013.
- [24] A. Ganesan, M. Yamada, and M. Fukumoto, "Cold Spray Coating Deposition Mechanism on the Thermoplastic and Thermosetting Polymer Substrates," *Journal of Thermal Spray Technology*, vol. 22, pp. 1275-1282, December 01 2013.

- [25] M. J. Vucko, P. C. King, A. J. Poole, C. Carl, M. Z. Jahedi, and R. de Nys, "Cold spray metal embedment: an innovative antifouling technology," *Biofouling*, vol. 28, pp. 239-48, 2012.
- [26] X. L. Zhou, A. F. Chen, J. C. Liu, X. K. Wu, and J. S. Zhang, "Preparation of metallic coatings on polymer matrix composites by cold spray," *Surface and Coatings Technology*, vol. 206, pp. 132-136, 2011/10/15/ 2011.
- [27] R. Lupoi and W. O'Neill, "Deposition of metallic coatings on polymer surfaces using cold spray," *Surface and Coatings Technology*, vol. 205, pp. 2167-2173, 2010/12/25/ 2010.
- [28] H. Che, X. Chu, P. Vo, and S. Yue, "Cold spray of mixed metal powders on carbon fibre reinforced polymers," *Surface and Coatings Technology*, vol. 329, pp. 232-243, 2017/11/25/ 2017.
- [29] V. Bortolussi, F. Borit, A. Chesnaud, M. Jeandin, M. Faessel, B. Figliuzzi, *et al.*, "Cold spray of metal-polymer composite coatings onto carbon fiber-reinforced polymer (CFRP)," in *International Thermal Spray Conference 2016 (ITSC 2016)*, Shanghai, China, 2016, p. 7 p.
- [30] S. Shah, J. Lee, and J. P. Rothstein, "Numerical Simulations of the High-Velocity Impact of a Single Polymer Particle During Cold-Spray Deposition," *Journal of Thermal Spray Technology*, vol. 26, pp. 970-984, June 01 2017.
- [31] A. Ganesan, J. Affi, M. Yamada, and M. Fukumoto, "Bonding behavior studies of cold sprayed copper coating on the PVC polymer substrate," *Surface and Coatings Technology*, vol. 207, pp. 262-269, 2012/08/25/ 2012.
- [32] C. Chen, X. Xie, Y. Xie, X. Yan, C. Huang, S. Deng, *et al.*, "Metallization of polyether ether ketone (PEEK) by copper coating via cold spray," *Surface and Coatings Technology*, vol. 342, pp. 209-219, 2018/05/25/ 2018.
- [33] J. Xie, D. Nélias, H. Walter-Le Berre, K. Ogawa, and Y. Ichikawa, "Simulation of the Cold Spray Particle Deposition Process," *Journal of Tribology*, vol. 137, pp. 041101-041101-15, 2015.
- [34] S. Yin, X. Wang, X. Suo, H. Liao, Z. Guo, W. Li, *et al.*, "Deposition behavior of thermally softened copper particles in cold spraying," *Acta Materialia*, vol. 61, pp. 5105-5118, 2013/08/01/ 2013.
- [35] T. Schmidt, H. Assadi, F. Gärtner, H. Richter, T. Stoltenhoff, H. Kreye, *et al.*, "From Particle Acceleration to Impact and Bonding in Cold Spraying," *Journal of Thermal Spray Technology*, vol. 18, p. 794, August 06 2009.
- [36] H. Che, P. Vo, and S. Yue, "Metallization of carbon fibre reinforced polymers by cold spray," *Surface and Coatings Technology*, vol. 313, pp. 236-247, 2017/03/15/ 2017.

- [37] "Standard Test Method for Adhesion or Cohesion Strength of Thermal Spray Coatings," ed, 2017.
- [38] A. Rezzoug, S. Abdi, A. Kaci, and M. Yandouzi, "Thermal spray metallisation of carbon fibre reinforced polymer composites: Effect of top surface modification on coating adhesion and mechanical properties," *Surface and Coatings Technology*, vol. 333, pp. 13-23, 2018/01/15/ 2018.
- [39] J. Affi, H. Okazaki, M. Yamada, and M. Fukumoto, "Fabrication of Aluminum Coating onto CFRP Substrate by Cold Spray," *MATERIALS TRANSACTIONS*, vol. 52, pp. 1759-1763, 2011.
- [40] F. Robitaille, M. Yandouzi, S. Hind, and B. Jodoin, "Metallic coating of aerospace carbon/epoxy composites by the pulsed gas dynamic spraying process," *Surface and Coatings Technology*, vol. 203, pp. 2954-2960, 2009/06/25/ 2009.
- [41] H.-S. SHIN, S.-T. PARK, S.-J. KIM, J.-H. CHOI, and J.-T. KIM, "DEFORMATION BEHAVIOR OF POLYMERIC MATERIALS BY TAYLOR IMPACT," *International Journal of Modern Physics B*, vol. 22, pp. 1235-1242, 2008.
- [42] S. Sarva, A. D. Mulliken, and M. C. Boyce, "Mechanics of Taylor impact testing of polycarbonate," *International Journal of Solids and Structures*, vol. 44, pp. 2381-2400, 2007/04/01/ 2007.
- [43] C. Roland, D. Fragiadakis, and R. Gamache, "Elastomer–steel laminate armor," *Composite Structures*, vol. 92, pp. 1059-1064, 04/01 2010.
- [44] A. Paman, G. Sukumar, B. Ramakrishna, and V. Madhu, "An optimization scheme for a multilayer armour module against 7.62 mm armour piercing projectile," *International Journal of Protective Structures*, vol. 11, pp. 185 - 208, 2019.
- [45] X.-T. Luo, G. M. Smith, Y. Wang, E. Gildersleeve, S. Sampath, and C.-J. Li, "Cracking induced tribological behavior changes for the HVOF WC-12Co cermet coatings," *Ceramics International*, vol. 45, pp. 4718-4728, 2019/03/01/ 2019.
- [46] C. R. Siviour, W. S.M., F. J.E., P. P.H., and S. N.A., "High strain rate characterization of polymers," *AIP Conference Proceedings*, vol. 1793, p. 060029, 2017.
- [47] M. J. Kendall and C. R. Siviour, "Experimentally simulating high-rate behaviour: rate and temperature effects in polycarbonate and PMMA," *Philosophical transactions. Series A, Mathematical, physical, and engineering sciences*, vol. 372, pp. 20130202-20130202, 2014.
- [48] E. C. Dogliotti and W. E. C. Yelland, "Effect of strain rate on the viscoelastic properties of high polymeric fibrous materials," *Journal of Applied Polymer Science*, vol. 8, pp. 211-235, 1964.

- [49] C. R. Siviour and J. L. Jordan, "High Strain Rate Mechanics of Polymers: A Review," *Journal of Dynamic Behavior of Materials*, vol. 2, pp. 15-32, March 01 2016.
- [50] M. Gagné and D. Therriault, "Lightning strike protection of composites," *Progress in Aerospace Sciences*, vol. 64, pp. 1-16, 2014/01/01/ 2014.
- [51] F. S. da Silva, N. Cinca, S. Dosta, I. G. Cano, J. M. Guilemany, C. S. A. Caires, *et al.*, "Corrosion resistance and antibacterial properties of copper coating deposited by cold gas spray," *Surface and Coatings Technology*, vol. 361, pp. 292-301, 2019/03/15/ 2019.
- [52] L.-K. Lin, J.-T. Tsai, S. Díaz-Amaya, M. R. Oduncu, Y. Zhang, P.-Y. Huang, *et al.*, "Antidelaminating, Thermally Stable, and Cost-Effective Flexible Kapton Platforms for Nitrate Sensors, Mercury Aptasensors, Protein Sensors, and p-Type Organic Thin-Film Transistors," *ACS Applied Materials & Interfaces*, vol. 13, pp. 11369-11384, 2021/03/10 2021.
- [53] J.-T. Tsai, L.-K. Lin, S.-T. Lin, L. Stanciu, and M. B.-G. Jun, "The influence of Bi₂O₃ glass powder in the silver paste and the impact on silicon solar cell substrates," *Materials & Design*, vol. 200, p. 109453, 2021/02/15/ 2021.
- [54] C. A. Gervasi, P. E. Alvarez, M. V. Fiori Bimbi, and M. E. Folquer, "Comparative cyclic voltammetry and SEM analysis of tin electrodes in citrate buffer solutions," *Journal of Electroanalytical Chemistry*, vol. 601, pp. 194-204, 2007/03/15/ 2007.
- [55] R. Riyanto, "Preparation and Application of Nickel Plating on Copper Electrode (NPCE) for Uric Acid Analysis in Human Urine Using Cyclic Voltammetry," *International Journal of Electrochemical Science*, vol. 14, pp. 2290-2304, 03/01 2019.
- [56] R. Renuka, L. Srinivasan, S. Ramamurthy, A. Veluchamy, and N. Venkatakrishnan, "Cyclic voltammetric study of zinc and zinc oxide electrodes in 5.3 M KOH," *Journal of Applied Electrochemistry*, vol. 31, pp. 655-661, 2001/06/01 2001.
- [57] B. Yildirim, H. Fukanuma, T. Ando, A. Gouldstone, and S. Müftü, "A Numerical Investigation Into Cold Spray Bonding Processes," *Journal of Tribology*, vol. 137, pp. 011102-011102-13, 2014.
- [58] A. Manap, T. Okabe, and K. Ogawa, "Computer simulation of cold sprayed deposition using smoothed particle hydrodynamics," *Procedia Engineering*, vol. 10, pp. 1145-1150, 2011/01/01/ 2011.
- [59] M. Murugesan and D. W. Jung, "Johnson Cook Material and Failure Model Parameters Estimation of AISI-1045 Medium Carbon Steel for Metal Forming Applications," *Materials*, vol. 12, p. 609, 02/18 2019.
- [60] D. Hu, M. Chen, L. Wang, and L. Yin, "Dynamic Constitutive Model of Physical Simulation in High-Speed Blanking for C5191 Phosphor Bronze," *Transactions of Nanjing University of Aeronautics and Astronautics*, vol. 35, pp. 1010-1017, 12/01 2018.

- [61] X. Wang and J. Shi, "Validation of Johnson-Cook plasticity and damage model using impact experiment," *International Journal of Impact Engineering*, vol. 60, pp. 67-75, 2013/10/01/ 2013.
- [62] F. Qin, T. An, and N. Chen, "Strain Rate Effects and Rate-Dependent Constitutive Models of Lead-Based and Lead-Free Solders," *Journal of Applied Mechanics*, vol. 77, 2009.
- [63] F. Qin, T. An, and N. Chen, "Strain rate effect and Johnson-Cook models of lead-free solder alloys," in *2008 International Conference on Electronic Packaging Technology & High Density Packaging*, 2008, pp. 1-7.
- [64] Z. Xu, Y. Liu, H. Hu, X. He, and F. Huang, "Thermo-viscoplastic behavior and constitutive modeling of pure copper under high-strain-rate shear condition," *Mechanics of Materials*, vol. 129, pp. 306-319, 2019/01/01/ 2019.
- [65] S. Yan, H. Yang, H. Li, and X. Yao, "A unified model for coupling constitutive behavior and micro-defects evolution of aluminum alloys under high-strain-rate deformation," *International Journal of Plasticity*, vol. 85, pp. 203-229, 2016/10/01/ 2016.
- [66] J. Xu, J. Li, D. Shan, and B. Guo, "Strain softening mechanism at meso scale during micro-compression in an ultrafine-grained pure copper," *AIP Advances*, vol. 5, p. 097147, 2015.
- [67] M. Borodachenkova, J. J. Gracio, R. Picu, and F. Barlat, "A microstructure-based model for describing strain softening during compression of Al-30%wt Zn alloy," *The International Journal of Multiphysics*, vol. 7, pp. 77-86, 03/01 2013.
- [68] M. Guo, K. Shen, and M. Wang, "Strain softening behavior in a particle-containing copper alloy," *Materials Science and Engineering: A*, vol. 527, pp. 2478-2485, 2010/04/25/ 2010.
- [69] W. Wei, K. X. Wei, and G. J. Fan, "A new constitutive equation for strain hardening and softening of fcc metals during severe plastic deformation," *Acta Materialia*, vol. 56, pp. 4771-4779, 2008/10/01/ 2008.
- [70] D. Rittel, G. Ravichandran, and S. Lee, "Large strain constitutive behavior of OFHC copper over a wide range of strain rates using the shear compression specimen," *Mechanics of Materials*, vol. 34, pp. 627-642, 2002/10/01/ 2002.
- [71] S. Rahmati and A. Ghaei, "The Use of Particle/Substrate Material Models in Simulation of Cold-Gas Dynamic-Spray Process," *Journal of Thermal Spray Technology*, vol. 23, 11/30 2013.
- [72] C. R. Siviour, S. M. Walley, W. G. Proud, and J. E. Field, "The high strain rate compressive behaviour of polycarbonate and polyvinylidene difluoride," *Polymer*, vol. 46, pp. 12546-12555, 2005/12/12/ 2005.
- [73] M. I. Okereke, C. P. Buckley, and C. R. Siviour, "Compression of polypropylene across a wide range of strain rates," *Mechanics of Time-Dependent Materials*, vol. 16, pp. 361-379, 2012/11/01 2012.

- [74] P. Church, R. Cornish, I. Cullis, P. Gould, and I. Lewtas, "Using the split Hopkinson pressure bar to validate material models," *Philosophical transactions. Series A, Mathematical, physical, and engineering sciences*, vol. 372, pp. 20130294-20130294, 2014.
- [75] S. Yin, X. Wang, W. Li, H. Liao, and H. Jie, "Deformation behavior of the oxide film on the surface of cold sprayed powder particle," *Applied Surface Science*, vol. 259, pp. 294-300, 2012/10/15/ 2012.
- [76] G. Bae, J.-i. Jang, and C. Lee, "Correlation of particle impact conditions with bonding, nanocrystal formation and mechanical properties in kinetic sprayed nickel," *Acta Materialia*, vol. 60, pp. 3524-3535, 2012/05/01/ 2012.
- [77] X. L. Zhou, S. J. Mou, X. K. Wu, and J. S. Zhang, "Deposition behavior of mixed binary metallic powders in cold spraying process," *Applied Surface Science*, vol. 257, pp. 10628-10633, 2011/10/01/ 2011.
- [78] S. Yin, X.-f. Wang, W. Y. Li, and H.-e. Jie, "Effect of substrate hardness on the deformation behavior of subsequently incident particles in cold spraying," *Applied Surface Science*, vol. 257, pp. 7560-7565, 2011/06/15/ 2011.
- [79] E. Wang, T. Nelson, and R. Rauch, "Back to Elements - Tetrahedra vs. Hexahedra," 01/01 2004.
- [80] A. Ramos and J. A. Simões, "Tetrahedral versus hexahedral finite elements in numerical modelling of the proximal femur," *Medical Engineering & Physics*, vol. 28, pp. 916-924, 2006/11/01/ 2006.
- [81] T. Schneider, Y. Hu, X. Gao, J. Dumas, D. Zorin, and D. Panozzo, *A Large Scale Comparison of Tetrahedral and Hexahedral Elements for Finite Element Analysis*, 2019.
- [82] C. A. Widener, M. J. Carter, O. C. Ozdemir, R. H. Hrabe, B. Hoiland, T. E. Stamey, *et al.*, "Application of High-Pressure Cold Spray for an Internal Bore Repair of a Navy Valve Actuator," *Journal of Thermal Spray Technology*, vol. 25, pp. 193-201, 2016/01/01 2016.
- [83] R. Nikbakht, S. H. Seyedein, S. Kheirandish, H. Assadi, and B. Jodoin, "Asymmetrical bonding in cold spraying of dissimilar materials," *Applied Surface Science*, vol. 444, pp. 621-632, 2018/06/30/ 2018.
- [84] W. Wong, P. Vo, E. Irissou, A. N. Ryabinin, J. G. Legoux, and S. Yue, "Effect of Particle Morphology and Size Distribution on Cold-Sprayed Pure Titanium Coatings," *Journal of Thermal Spray Technology*, vol. 22, pp. 1140-1153, 2013/10/01 2013.
- [85] B. Samareh and A. Dolatabadi, "A Three-Dimensional Analysis of the Cold Spray Process: The Effects of Substrate Location and Shape," *Journal of Thermal Spray Technology*, vol. 16, pp. 634-642, December 01 2007.

- [86] F. Boschini, V. Delaval, K. Traina, N. Vandewalle, and G. Lumay, "Linking flowability and granulometry of lactose powders," *International Journal of Pharmaceutics*, vol. 494, pp. 312-320, 2015/10/15/ 2015.
- [87] E. R. L. Espiritu, A. Kumar, A. Nommeots-Nomm, J. A. M. Lerma, and M. Brochu, "Investigation of the rotating drum technique to characterise powder flow in controlled and low pressure environments," *Powder Technology*, vol. 366, pp. 925-937, 2020/04/15/ 2020.
- [88] G. Lumay, F. Boschini, K. Traina, S. Bontempi, J. C. Remy, R. Cloots, *et al.*, "Measuring the flowing properties of powders and grains," *Powder Technology*, vol. 224, pp. 19-27, 2012/07/01/ 2012.
- [89] A. B. Spierings, M. Voegtlin, T. Bauer, and K. Wegener, "Powder flowability characterisation methodology for powder-bed-based metal additive manufacturing," *Progress in Additive Manufacturing*, vol. 1, pp. 9-20, 2016/06/01 2016.
- [90] N. Hagbin, A. Khakpour, J. Schwartzentruber, and M. Papini, "Measurement of abrasive particle velocity and size distribution in high pressure abrasive slurry and water micro-jets using a modified dual disc anemometer," *Journal of Materials Processing Technology*, vol. 263, pp. 164-175, 2019/01/01/ 2019.
- [91] A. Fry, M. Gee, S. Clausen, U. Neuschaefer-Rube, M. Bartscher, D. Spaltmann, *et al.*, "Metrology to enable high temperature erosion testing - A new european initiative," *Advances in Materials Technology for Fossil Power Plants - Proceedings from the 7th International Conference*, pp. 400-411, 01/01 2014.
- [92] B. Karpuschewski, A. M. Hoogstrate, and M. Achtsnick, "Simulation and Improvement of the Micro Abrasive Blasting Process," *CIRP Annals*, vol. 53, pp. 251-254, 2004/01/01/ 2004.
- [93] A. M. Hoogstrate, B. Karpuschewski, C. A. van Luttervelt, and H. J. J. Kals, "Modelling of high velocity, loose abrasive machining processes," *CIRP Annals*, vol. 51, pp. 263-266, 2002/01/01/ 2002.
- [94] S. K. Hovis, K. Anand, H. Conrad, and R. O. Scattergood, "A new method of velocity calibration for erosion testing," *Wear*, vol. 101, pp. 69-76, 1985/01/01/ 1985.
- [95] V. Shikalov, S. Klinkov, and V. Kosarev, *Low pressure cold spraying on materials with low erosion resistance* vol. 1893, 2017.
- [96] M. Fukumoto, H. Terada, M. Mashiko, K. Sato, M. Yamada, and E. Yamaguchi, "Deposition of Copper Fine Particle by Cold Spray Process," *MATERIALS TRANSACTIONS*, vol. 50, pp. 1482-1488, 2009.
- [97] A.-N. Huang, K. Ito, T. Fukasawa, K. Fukui, and H.-P. Kuo, "Effects of particle mass loading on the hydrodynamics and separation efficiency of a cyclone separator," *Journal of the Taiwan Institute of Chemical Engineers*, vol. 90, pp. 61-67, 2018/09/01/ 2018.

- [98] N. Kharoua, L. Khezzar, and Z. Nemouchi, "Study of the Pressure Drop and Flow Field in Standard Gas Cyclone Models Using the Granular Model," *International Journal of Chemical Engineering*, vol. 2011, p. 791218, 2011/07/07 2011.
- [99] M. Nakhaei, B. Lu, Y. Tian, W. Wang, K. Dam-Johansen, and H. Wu, "CFD Modeling of Gas–Solid Cyclone Separators at Ambient and Elevated Temperatures," *Processes*, vol. 8, p. 228, 2020.
- [100] K. Elsayed and C. Lacor, "The effect of cyclone inlet dimensions on the flow pattern and performance," *Applied Mathematical Modelling*, vol. 35, pp. 1952-1968, 2011/04/01/ 2011.
- [101] D. McGlinchey, "Bulk Solids Handling: Equipment Selection and Operation," 2008.
- [102] C. Buckley, P. Dooling, J. Harding, and C. Ruiz, "Deformation of thermosetting resins at impact rates of strain. Part 2: Constitutive model with rejuvenation," *Journal of the Mechanics and Physics of Solids*, vol. 52, pp. 2355-2377, 10/01 2004.
- [103] A. D. Mulliken and M. C. Boyce, "Mechanics of the rate-dependent elastic–plastic deformation of glassy polymers from low to high strain rates," *International Journal of Solids and Structures*, vol. 43, pp. 1331-1356, 2006/03/01/ 2006.
- [104] P. Yu, X. Yao, Q. Han, S. Zang, and Y. Gu, "A visco-elastoplastic constitutive model for large deformation response of polycarbonate over a wide range of strain rates and temperatures," *Polymer*, vol. 55, pp. 6577-6593, 2014/12/01/ 2014.
- [105] J. Sweeney, "A comparison of three polymer network models in current use," *Computational and Theoretical Polymer Science*, vol. 9, pp. 27-33, 1999/03/01/ 1999.
- [106] J. S. Bergström and M. C. Boyce, "Deformation of Elastomeric Networks: Relation between Molecular Level Deformation and Classical Statistical Mechanics Models of Rubber Elasticity," *Macromolecules*, vol. 34, pp. 614-626, 2001/01/01 2001.
- [107] M. C. Boyce, G. G. Weber, and D. M. Parks, "On the kinematics of finite strain plasticity," *Journal of the Mechanics and Physics of Solids*, vol. 37, pp. 647-665, 1989/01/01/ 1989.
- [108] E. M. Arruda and M. C. Boyce, "A three-dimensional constitutive model for the large stretch behavior of rubber elastic materials," *Journal of the Mechanics and Physics of Solids*, vol. 41, pp. 389-412, 1993/02/01/ 1993.
- [109] E. M. Arruda and M. C. Boyce, "Evolution of plastic anisotropy in amorphous polymers during finite straining," *International Journal of Plasticity*, vol. 9, pp. 697-720, 1993/01/01/ 1993.
- [110] "ASTM International. D638-14 Standard Test Method for Tensile Properties of Plastics. West Conshohocken, PA, 2014., " ed.
- [111] J. Bergström, A. Bowden, C. Rimnac, and S. Kurtz, "Development and Implementation of an Advanced User Material Model for UHMWPE," 11/02 2019.

- [112] H. Cho, S. Bartyczak, W. Mock, and M. C. Boyce, "Dissipation and resilience of elastomeric segmented copolymers under extreme strain rates," *Polymer*, vol. 54, pp. 5952-5964, 2013/10/04/ 2013.
- [113] S. Rahmati and B. Jodoin, "Physically Based Finite Element Modeling Method to Predict Metallic Bonding in Cold Spray," *Journal of Thermal Spray Technology*, vol. 29, pp. 611-629, 2020/04/01 2020.
- [114] I. C. Sinka, J. C. Cunningham, and A. Zavaliangos, "The effect of wall friction in the compaction of pharmaceutical tablets with curved faces: a validation study of the Drucker–Prager Cap model," *Powder Technology*, vol. 133, pp. 33-43, 2003/07/30/ 2003.
- [115] D. Cronin, K. Bui, C. Kaufmann, G. J. McIntosh, and T. Berstad, "Implementation and Validation of the Johnson-Holmquist Ceramic Material Model in LS-Dyna," 2003.
- [116] G. R. Johnson and T. J. Holmquist, "An improved computational constitutive model for brittle materials," *AIP Conference Proceedings*, vol. 309, pp. 981-984, 1994.
- [117] T. J. Holmquist and G. R. Johnson, "Characterization and evaluation of silicon carbide for high-velocity impact," *Journal of Applied Physics*, vol. 97, p. 093502, 2005.
- [118] S. Deng, L. Djukic, R. Paton, and L. Ye, "Thermoplastic–epoxy interactions and their potential applications in joining composite structures – A review," *Composites Part A: Applied Science and Manufacturing*, vol. 68, pp. 121-132, 2015/01/01/ 2015.
- [119] V. M. Marx, F. Toth, A. Wiesinger, J. Berger, C. Kirchlechner, M. J. Cordill, *et al.*, "The influence of a brittle Cr interlayer on the deformation behavior of thin Cu films on flexible substrates: Experiment and model," *Acta Materialia*, vol. 89, pp. 278-289, 2015/05/01/ 2015.
- [120] T. Jörg, M. J. Cordill, R. Franz, C. Kirchlechner, D. M. Többens, J. Winkler, *et al.*, "Thickness dependence of the electro-mechanical response of sputter-deposited Mo thin films on polyimide: Insights from in situ synchrotron diffraction tensile tests," *Materials Science and Engineering: A*, vol. 697, pp. 17-23, 2017/06/14/ 2017.
- [121] M. J. Cordill, A. Kleinbichler, B. Völker, P. Kraker, D. R. Economy, D. Többens, *et al.*, "In-situ observations of the fracture and adhesion of Cu/Nb multilayers on polyimide substrates," *Materials Science and Engineering: A*, vol. 735, pp. 456-462, 2018/09/26/ 2018.
- [122] G. M. Smith, O. Higgins, and S. Sampath, "In-situ observation of strain and cracking in coated laminates by digital image correlation," *Surface and Coatings Technology*, vol. 328, pp. 211-218, 2017/11/15/ 2017.
- [123] D. J. Wu, W. G. Mao, Y. C. Zhou, and C. Lu, "Digital image correlation approach to cracking and decohesion in a brittle coating/ductile substrate system," *Applied Surface Science*, vol. 257, pp. 6040-6043, 2011/05/01/ 2011.

- [124] T. Li and Z. Suo, "Ductility of thin metal films on polymer substrates modulated by interfacial adhesion," *International Journal of Solids and Structures*, vol. 44, pp. 1696-1705, 2007/03/15/ 2007.
- [125] Y. Xiang, T. Li, Z. Suo, and J. J. Vlassak, "High ductility of a metal film adherent on a polymer substrate," *Applied Physics Letters*, vol. 87, p. 161910, 2005.
- [126] T. Li, Z. Zhang, and B. Michaux, "Competing failure mechanisms of thin metal films on polymer substrates under tension," *Theoretical and Applied Mechanics Letters*, vol. 1, 07/10 2011.
- [127] Y. Leterrier, L. Médico, F. Demarco, J. A. E. Månson, U. Betz, M. F. Escolà, *et al.*, "Mechanical integrity of transparent conductive oxide films for flexible polymer-based displays," *Thin Solid Films*, vol. 460, pp. 156-166, 2004/07/22/ 2004.
- [128] Z. C. Xia and J. W. Hutchinson, "Crack patterns in thin films," *Journal of the Mechanics and Physics of Solids*, vol. 48, pp. 1107-1131, 2000/06/01/ 2000.
- [129] M. Yanaka, T. Miyamoto, Y. Tsukahara, and N. Takeda, "In situ observation and analysis of multiple cracking phenomena in thin glass layers deposited on polymer films," *Composite Interfaces*, vol. 6, pp. 409-424, 1998/01/01 1998.
- [130] S. Frank, U. A. Handge, S. Olliges, and R. Spolenak, "The relationship between thin film fragmentation and buckle formation: Synchrotron-based in situ studies and two-dimensional stress analysis," *Acta Materialia*, vol. 57, pp. 1442-1453, 2009/03/01/ 2009.
- [131] M. Cordill, A. Taylor, J. Schalko, and G. Dehm, "Fracture and Delamination of Chromium Thin Films on Polymer Substrates," *Metallurgical and Materials Transactions A*, vol. 41, pp. 870-875, 04/01 2009.
- [132] B. Lauke, W. Beckert, and J. Singletary, "Energy release rate and stress field calculation for debonding crack extension at the fibre-matrix interface during single-fibre pull-out," *Composite Interfaces*, vol. 3, pp. 263-273, 1995/01/01 1995.
- [133] X.-l. Li, Y. Zang, Y. Lian, M.-y. Ma, L. Mu, and Q. Qin, "An interface shear damage model of chromium coating/steel substrate under thermal erosion load," *Defence Technology*, vol. 17, pp. 405-415, 2021/04/01/ 2021.
- [134] R. Joffe, J. Andersons, and L. Wallström, "Interfacial shear strength of flax fiber/thermoset polymers estimated by fiber fragmentation tests," *Journal of Materials Science*, vol. 40, pp. 2721-2722, 2005/05/01 2005.
- [135] S. Feih, K. Wonsyld, D. Minzari, P. Westermann, and H. Lilholt, "Testing procedure for the single fiber fragmentation test," 01/01 2004.
- [136] J. Andersons, E. Spārniņš, R. Joffe, and L. Wallström, "Strength distribution of elementary flax fibres," *Composites Science and Technology*, vol. 65, pp. 693-702, 2005/03/01/ 2005.

- [137] Y. Leterrier, Y. Wyser, J. A. E. Månson, and J. Hilborn, "A Method to Measure the Adhesion of Thin Glass Coatings on Polymer Films," *The Journal of Adhesion*, vol. 44, pp. 213-227, 1994/02/01 1994.
- [138] T. Lacroix, R. Keunings, M. Desaegeer, and I. Verpoest, "A new data reduction scheme for the fragmentation testing of polymer composites," *Journal of Materials Science*, vol. 30, pp. 683-692, 1995/02/01 1995.
- [139] B. Yavin, H. E. Gallis, J. Scherf, A. Eitan, and H. D. Wagner, "Continuous monitoring of the fragmentation phenomenon in single fiber composite materials," *Polymer Composites*, vol. 12, pp. 436-446, 1991.
- [140] O. Glushko and M. J. Cordill, "Electrical Resistance of Metal Films on Polymer Substrates Under Tension: Electrical Resistance of Metal Films on Polymer," *Experimental Techniques*, 2014.
- [141] D. Faurie, F. Zighem, A. Garcia-Sanchez, P. Lupo, and A. O. Adeyeye, "Fragmentation and adhesion properties of CoFeB thin films on polyimide substrate," *Applied Physics Letters*, vol. 110, p. 091904, 2017.
- [142] W. Harizi, R. Azzouz, A. T. Martins, K. Hamdi, Z. Aboura, and K. Khellil, "Electrical resistance variation during tensile and self-heating tests conducted on thermoplastic polymer-matrix composites," *Composite Structures*, vol. 224, p. 111001, 2019/09/15/ 2019.
- [143] J. L. Beuth, "Cracking of thin bonded films in residual tension," *International Journal of Solids and Structures*, vol. 29, pp. 1657-1675, 1992/01/01/ 1992.
- [144] D. Turner, P. Crozier, and P. Reu, "Digital Image Correlation Engine," ed. United States, 2015, pp. Medium: X; OS: !Mac OSX 10.9, W indows 7, Linux; Compatibility: Multiplatform.
- [145] M. Hadad, "Adhesion and residual stress evaluation of thermally sprayed coatings," Ph.D., Mechanical Engineering, University of Lille, 2010.
- [146] W. A. Curtin, "Tensile Strength of Fiber-Reinforced Composites: III. Beyond the Traditional Weibull Model for Fiber Strengths," *Journal of Composite Materials*, vol. 34, pp. 1301-1332, 2000.
- [147] Y. Leterrier, J. Andersons, Y. Pitton, and J.-A. E. Månson, "Adhesion of silicon oxide layers on poly(ethylene terephthalate). II: Effect of coating thickness on adhesive and cohesive strengths," *Journal of Polymer Science Part B: Polymer Physics*, vol. 35, pp. 1463-1472, 1997.
- [148] Y. Leterrier, L. Boogh, J. Andersons, and J.-A. E. Månson, "Adhesion of silicon oxide layers on poly(ethylene terephthalate). I: Effect of substrate properties on coating's fragmentation process," *Journal of Polymer Science Part B: Polymer Physics*, vol. 35, pp. 1449-1461, 1997.

- [149] T. Jörg, M. J. Cordill, R. Franz, O. Glushko, J. Winkler, and C. Mitterer, "The electro-mechanical behavior of sputter-deposited Mo thin films on flexible substrates," *Thin Solid Films*, vol. 606, pp. 45-50, 2016/05/01/ 2016.
- [150] V. B. Shenoy, A. F. Schwartzman, and L. B. Freund, "Crack patterns in brittle thin films," *International Journal of Fracture*, vol. 109, pp. 29-45, 2001/05/01 2001.
- [151] M. V. Tavares da Costa and E. K. Gamstedt, "Energy-release rates and opening of cracks in thin barrier coatings on polymer substrates subjected to tensile loading," *Engineering Fracture Mechanics*, vol. 235, p. 107151, 2020/08/01/ 2020.
- [152] B. Q. Yang, K. Zhang, G. N. Chen, G. X. Luo, and J. H. Xiao, "Measurement of fracture toughness and interfacial shear strength of hard and brittle Cr coating on ductile steel substrate," *Surface Engineering*, vol. 24, pp. 332-336, 2008/09/01 2008.
- [153] S. Akin, T. Gabor, S. Jo, H. Joe, J.-T. Tsai, Y. Park, *et al.*, "Dual Regime Spray Deposition Based Laser Direct Writing of Metal Patterns on Polymer Substrates," *Journal of Micro and Nano-Manufacturing*, vol. 8, 2020.
- [154] M. Wang, X. Wang, P. Moni, A. Liu, D. H. Kim, W. J. Jo, *et al.*, "CVD Polymers for Devices and Device Fabrication," *Advanced materials (Deerfield Beach, Fla.)*, vol. 29, p. 1604606, 2017.
- [155] X. Liu, P. Gong, H. Hu, M. Zhao, K. Zhang, and H. Zhou, "Study on the tribological properties of PVD polymer-like carbon films in air/vacuum/N₂ and cycling environments," *Surface and Coatings Technology*, vol. 406, p. 126677, 2021/01/25/ 2021.
- [156] S. Akin, J.-T. Tsai, M. S. Park, Y. H. Jeong, and M. B.-G. Jun, "Fabrication of Electrically Conductive Patterns on Acrylonitrile-Butadiene-Styrene Polymer Using Low-Pressure Cold Spray and Electroless Plating," *Journal of Micro and Nano-Manufacturing*, vol. 8, 2021.
- [157] A. Equbal, A. Equbal, and A. K. Sood, "Metallization on FDM Processed Parts Using Electroless Procedure," *Procedia Materials Science*, vol. 6, pp. 1197-1206, 2014/01/01/ 2014.
- [158] S. K. Sahoo, A. K. Sahu, and S. S. Mahapatra, "Environmental friendly electroless copper metallization on FDM build ABS parts," *International Journal of Plastics Technology*, vol. 21, pp. 297-312, 2017/12/01 2017.
- [159] J.-T. Tsai, S. Akin, F. Zhou, D. F. Bahr, and M. B.-G. Jun, "Establishing a Cold Spray Particle Deposition Window on Polymer Substrate," *Journal of Thermal Spray Technology*, vol. 30, pp. 1069-1080, 2021/04/01 2021.
- [160] "Standard Test Method for Tensile Properties of Polymer Matrix Composite Materials," ed.

- [161] J.-T. Tsai, D. F. Bahr, S. Akin, F. Zhou, M. B.-G. Jun, and M. Park, "Simulation and Characterization of Cold Spray Deposition of Metal Powders on Polymer Substrate Electrically Conductive Application," in *ASME 2020 15th International Manufacturing Science and Engineering Conference*, 2020.